Università degli Studi di Catania
Scuola Superiore di Catania

International PhD
in
Nanosciences
XXIII cycle

Quantum transport in confined graphene: role of defects, substrate and contacts

Ioannis Deretzis

Coordinators	Tutors
Prof. Emanuele Rimini	Dr. Antonino La Magna
Prof. Maria Grazia Grimaldi	Dr. Giovanni Piccitto

a.a. 2007/2010

To Marina, Matteo and Sofia

Acknowledgements

I would like to acknowledge Antonino La Magna for guidance, support and patience throughout this PhD period.

I would like to thank Gianluca Fiori and Giuseppe Iannaccone for hospitality and collaboration during the three-months period spent at the engineering department of the University of Pisa.

I am grateful to Giovanni Piccitto for tutoring and to Giuseppe Forte for collaboration.

I would also like to thank the following people: Vito Raineri, Silvia Scalese, Vittorio Privitera, Corrado Spinella, Emanuele Rimini, Viviana Scuderi, Renato Pucci, Sushant Sonde, Jens Eriksson, Filippo Giannazzo, Massimo Camarda.

Finally a big thanks to family and friends.

Contents

List of Figures

Chapter 1

Introduction

1.1 Toward novel digital application technology

Silicon-based complementary-metal-oxide semiconductor technology has ruled the semiconducting industry for the last decades. However, pure silicon electronics is arriving toward its physical limits in terms of traditional transistor operation: as channel lengths get reduced below $L_{ch} \sim 30 - 20nm$, strong differentiations in the device operation are expected due to the presence of quantum confinement, while problems like leakage currents and dielectric scaling arise. In this sense the search of alternative materials for nanoscale integration in electronics, sensors and environmental applications that would allow for a further reduction of transistor dimensions while at the same time increasing clock speeds and reducing power dissipation becomes eminent. Under this perspective a new concept of low-dimensionality comes into the picture. Reduced dimensionality can significantly advance miniaturization and improve performance of plausible logic and storage devices. The advantages of small size in nanoelectronics are well known: devices can become faster, denser and require lower power consumption.

The idea of embedding single molecules between two electrodes and make molecular devices stands since the mid seventies[2]. However the real revolution in low-dimensional electronics took place at the early nineties with the discovery of carbon nanotubes[59], i.e. quasi one-dimensional sp^2-bonded carbon allotrope systems that look like a single rolled sheet of graphite. Carbon nanotube research grew exponentially in the following years whereas important achievements come into the picture also to date. This research framework served for the incubation of the concept of a pure two-dimensional (2D) system. Previously, quasi-2D electron gas systems existed only in heterostructure junctions like the one that forms in the GaN/AlGaN interface. However the idea of a pure 2D material was lacking any consistence whereas serious thermodynamical stability concerns were raised. At 2004 Novoselov *et al.*[81] showed the existence and stability of a pure

2D system deriving as a single one-atom thick graphite sheet. Such a discovery brought an intense interest on the study of this material both from a scientific as well as from an industrial point of view, being the first one to posses this type of dimensionality, and consequently, a series of exceptional characteristics. In this chapter some key structural and electronic properties of graphene-based systems will be reviewed in order to establish the problematics for this PhD study.

1.2 Graphene: a two-dimensional world

Graphene is a one-atom thick planar sp^2 carbon allotrope system with particular electrical, mechanical and optical characteristics[14, 31, 44]. Structurally graphene is a hexagonal honeycomb surface where each carbon atom is covalently bonded with three neighboring atoms at a distance $d \simeq 1.42$ Å (see Figure 1.1). The primitive basis vectors of the underlying Bravais lattice read:

$$\vec{a_1} = \frac{a}{2}\begin{pmatrix}\sqrt{3}\\ 1\end{pmatrix} \tag{1.1}$$

$$\vec{a_2} = \frac{a}{2}\begin{pmatrix}\sqrt{3}\\ -1\end{pmatrix} \tag{1.2}$$

where $\vec{a_1}, \vec{a_2}$ are lattice vectors and a is the in plane graphite lattice constant, having a value of $a = \sqrt{3}d \simeq 2.46$ Å. Since the translation of each one of the basis vectors gives rise to a triangular lattice, graphene can be thought of as the superposition of two triangular interpenetrating lattices.

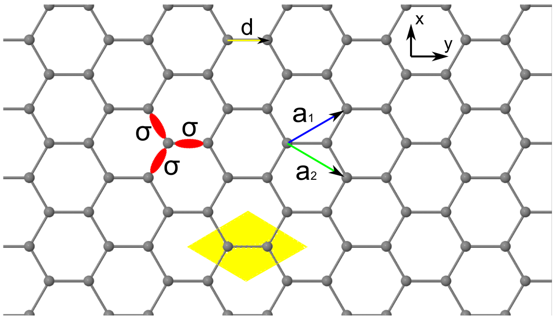

Figure 1.1: Graphene lattice - The atomic structure of a graphene surface where $\vec{a_1}, \vec{a_2}$ are lattice vectors and σ are the sp^2-hybridized bonds that allow for the covalent bonding between neighboring atoms. The WignerSeitz cell is highlighted in yellow.

The sp^2 hybridization scheme provides for the presence of both σ and π orbitals in the electronic structure of this system. The σ orbitals primarily lie along the structure's surface and are responsible for covalent bonding between neighboring C atoms that forms the basis of the extremely high mechanical stability of this material (see figure 1.1). On the other hand σ bonds have energies that are too far away from the Fermi level and do not contribute in the electrical, thermal and optical characteristics of graphene. The remaining π orbitals (one per carbon atom) lie perpendicular to the lattice surface and are responsible for the peculiarity of its low-energy electronic properties.

Probing for the electronic structure of graphene can be simple and straightforward within a next-neighbor Tight Binding (TB) model. Such a description accounts only for the linear combination of π atomic orbitals of graphene, being sufficient for the low-energy spectrum of this material. We start from the next-neighbor TB Hamiltonian:

$$H = -t \sum_{<i,j>} c_i^\dagger c_j + H.c., \tag{1.3}$$

where $c_i(c_i^\dagger)$ is the annihilation (creation) operator and t is the hopping integral with a typical value $t = 2.7eV$. The previous Hamiltonian can be rewritten with a notation that introduces the bipartite nature of the honeycomb lattice[88]:

$$H = -t \sum_{n,m} c_{n,m,\sigma}^{(1)\dagger} \left(c_{n,m,\sigma}^{(2)} + c_{n+1,m,\sigma}^{(2)} + c_{n,m+1,\sigma}^{(2)} \right) + H.c., \tag{1.4}$$

where operator $c^{(1)}(c^{(1)\dagger})$ is the annihilation (creation) operator at sublattice $\vec{L}_{n,m}^{(1)} = n\vec{\alpha_1} + m\vec{\alpha_2}$, and $c^{(2)}(c^{(2)\dagger})$ is the annihilation (creation) operator at sublattice $\vec{L}_{n,m}^{(2)} = n\vec{\alpha_1} + m\vec{\alpha_2} + \vec{d}$. By Fourier transforming in momentum space we get:

$$b_{\vec{k},\sigma}^{(1)} = \frac{1}{\sqrt{N_s}} \sum_{n,m} e^{i\vec{k}\cdot\vec{L}_{n,m}^{(1)}} c_{n,m,\sigma}^{(1)} \tag{1.5}$$

$$b_{\vec{k},\sigma}^{(2)} = \frac{1}{\sqrt{N_s}} \sum_{n,m} e^{i\vec{k}\cdot\vec{L}_{n,m}^{(2)}} c_{n,m,\sigma}^{(2)} \tag{1.6}$$

$$c_{n,m,\sigma}^{(1)} = \frac{1}{\sqrt{N_s}} \sum_{\vec{k}} e^{i\vec{k}\cdot\vec{L}_{n,m}^{(1)}} b_{\vec{k},\sigma}^{(1)} \tag{1.7}$$

$$c_{n,m,\sigma}^{(2)} = \frac{1}{\sqrt{N_s}} \sum_{\vec{k}} e^{i\vec{k}\cdot\vec{L}_{n,m}^{(2)}} b_{\vec{k},\sigma}^{(2)} \tag{1.8}$$

where $\vec{k}$ is the electron quasi-momentum, N_s the number of unit cells in the graphene sheet, and $\vec{L}$ the cell position index. Substituting back to 1.4 we get:

$$H = \sum_{\vec{k}} H(\vec{k}) \qquad = -te^{-i\vec{k}\cdot\vec{d}}\left(1 + e^{-i\vec{k}\cdot\vec{\alpha_1}} + e^{-i\vec{k}\cdot\vec{\alpha_2}}\right) \cdot b^{(1)^\dagger}_{\vec{k},\sigma} \cdot b^{(2)}_{\vec{k},\sigma} + H.c. \tag{1.9}$$

The energy dispersion relation can be derived from the previous Hamiltonian by means of a Bogoliubov transformation:

$$H(\vec{k}) = \pm t\sqrt{3 + 2cos(\vec{k}\cdot\vec{\alpha_1}) + 2cos(\vec{k}\cdot(\vec{\alpha_2} - \vec{\alpha_1}))} \cdot \tilde{b}^\dagger_{\vec{k},\sigma} \cdot \tilde{b}_{\vec{k},\sigma}, \tag{1.10}$$

where $\tilde{b}_{\vec{k},\sigma}$ is a linear combination of $b^{(1)}_{\vec{k},\sigma}$ and $b^{(2)}_{\vec{k},\sigma}$. By projecting the previous expression on the graphene plain we have:

$$E(k_x, k_y) = \pm t\sqrt{1 + 4cos^2(\frac{k_y a}{2}) + 4cos(\frac{k_y a}{2}) \cdot cos(\frac{k_x\sqrt{3}a}{2})}, \tag{1.11}$$

where k_x, k_y are wavevector components along the x, y directions (see figure 1.2). Here valence and conduction bands meet exactly at the charge neutrality level at the high symmetry *K* and *K'* points of the respective Brillouin zone. Such a band formation gives rise to a density of states that vanishes linearly at the Fermi level making graphene a half-filled zero-gap semiconductor.

The peculiarity of the band structure of graphene lies in the linear dispersion near the Fermi level (see figure 1.2(b)) where electrons behave like Dirac massless chiral quasiparticles (relativistic fermions), making graphene an ideal platform for the experimental study of quantum electrodynamics phenomena. Indeed, for the low energy spectrum the dispersion relation reads:

$$H(\vec{k}) = \pm\hbar\nu_F \begin{bmatrix} 0 & k_x - ik_y \\ k_x + ik_y & 0 \end{bmatrix} = \pm\hbar\nu_F\vec{\sigma}\cdot\vec{k}, \tag{1.12}$$

where $\vec{k}$ is the quasiparticle momentum, $\vec{\sigma}$ are the 2D Pauli matrix and ν_F is the Fermi velocity. It should be noted that the use of the Dirac-like Hamiltonian is valid only for a small part of the energy spectrum ($|E| <\sim 1eV$) of 2D graphene, while it lacks sense for higher energies or other forms of confined graphene systems.

The electronic, structural and geometrical properties of graphene form the cornerstone of its physical peculiarity, giving rise to the manifestation of a series

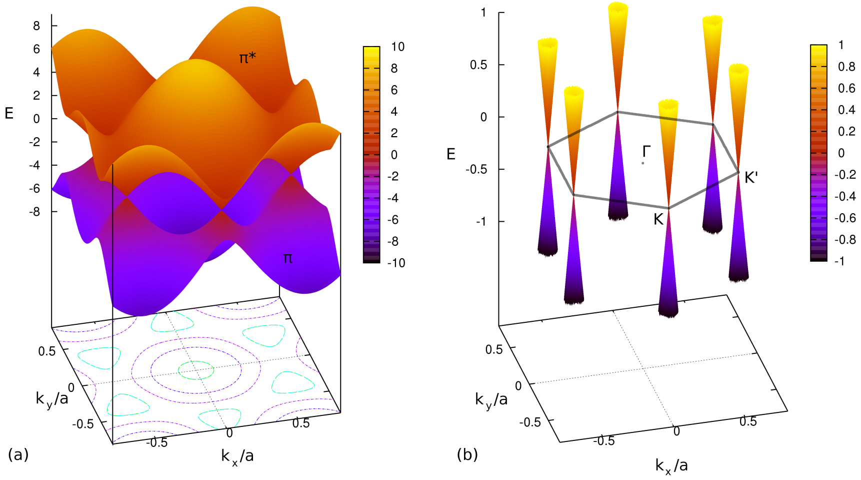

Figure 1.2: Graphene bandstructure - (a) Energy dispersion relation of two-dimensional graphene for the π and π^* bands. (b) Detail of the energy dispersion relation of two-dimensional graphene for the π and π^* bands showing band meeting at the high symmetry K and K' points of the first Brillouin zone.

of exceptional phenomena[44]: extreme mechanical strength, room-temperature half-integer quantum Hall effect, high thermal conductivity, huge charge carrier densities and mobilities, to name but a few. Under this perspective graphene becomes an outstanding candidate for integration in nanoelectronics, since it combines both low-dimensionality and exceptional device requested characteristics.

1.3 Where is the gap?

Out of the plethora of the excellent electronic properties that could make graphene an ideal candidate for post-Si CMOS technology there is still one missing, i.e. the intrinsic bandgap that could allow graphene to be used as an active component in semiconducting devices. Indeed, great amounts of research have been spent during the last years for such a non-trivial problem. The proposed solutions generally fall within five main categories: a) the first solution has to do with the lateral confinement of graphene in one dimension, i.e. the mechanical transformation from a quantum well to a quantum wire. It has been shown from atomistic calculations beyond the next-neighbor TB model that the so-called graphene nanoribbons (GNRs) with an armchair type of lateral confinement (where armchair refers to the edges, see figure 1.3) should bear a semiconducting gap that depends on the number of dimer lines N_a along the ribbon width. If we moreover consider electron exchange and correlation features in the electronic model, it turns out that also GNRs with the zigzag-type of confinement exhibit a secondary meV bandgap due to the presence of edge magnetism[99]. Within this framework lateral confinement has been proposed as a key factor that could engineer intrinsic bandgaps in graphene structures. b) The second proposal involves Bernel-stacked bilayer graphene systems, where it has been observed that the application of a perpendicular electric field (e.g. using a gate electrode) gives rise to a bandgap of the order of $\sim 200meV$[43, 119]. Notwithstanding this positive perspective, such a bandgap is still too small for the high current on/off ratios required for device operation[38]. c) A third route towards bandgap engineering has been identified in the interaction between graphene and a substrate. It has been argued, e.g. in the case of epitaxial graphene, that such interactions can give rise to bandgap openings for the first graphene layer that forms on the substrate[121]. However the stronger this interaction the more likely is for the π bands to get destroyed, giving rise to a significant loss of graphene's exceptional electrical properties. d) It has been shown theoretically that chemical functionalization with reactive atoms or molecules can act directly on the electronic structure of graphene-based systems and give rise to direct band gaps [9, 43]. However also in this case the drawback consists in the possibility to balance between a controllable dopant concentration and the maintaining of graphene π bands. e) Lately and in conjunction with the lateral confinement, the generation of mobility gaps has been proposed within a backscattering mechanism from defects and substitutional impurities during conduction[6]. Such a mechanism could tune the device characteristics and reduce the differentiations in the bandgaps based on the exact confinement (e.g. see figure 1.3) without being invasive and therefore without compromising the bandstructure of ideal graphene. While all previously mentioned methodologies have their pros and cons, a mostly plausible route towards bandgap engineering within a current view of technological advances, which guarantees device-requested functionality, appears to be the one of lateral confinement, with all enhancements made possible by surface chemistry and engineering.

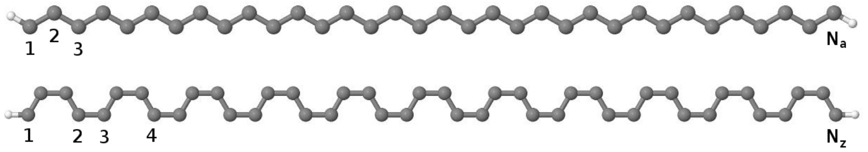

Figure 1.3: Graphene edges - Armchair (upper) and zigzag (lower) edges passivated by single hydrogens for graphene nanoribbon structures. The respective graphene nanoribbons can be categorized on the basis of the dimer lines N_a and zigzag chains N_z along the ribbon width.

1.3.1 Armchair confinement

Armchair graphene nanoribbons (aGNRs) are quasi-1D graphene-based structures, where the lateral confinement consists of left/right terminated armchair edges. Prevailing definition enumerates the number of dimer lines N_a along the ribbon width[99] (see figure 1.3). Probing for the electronic properties of ideal aGNRs can take place analytically within the TB schema of eq. 1.3 by considering appropriate boundary conditions towards the width of these structures that nullify the wavefunction out of the structure's borders[120]:

$$q_y = \frac{2}{a} \frac{p\pi}{N_a + 1}, \tag{1.13}$$

where q_y is the discretized vector in the y direction and $p = 1, 2, 3, ..., N_a$. Hamiltonian diagonalization here gives the following dispersion relation:

$$E(k_x, q_y) = \pm t \left(2e^{\frac{ik_x a}{2\sqrt{3}}} \cdot cos \frac{aq_y}{2} + e^{\frac{-ik_x a}{\sqrt{3}}} \right) \tag{1.14}$$

A key characteristic of the TB bandstructure of aGNRs is its dependence on the number of dimer lines according to the following rule: $\forall p \in \mathbb{N}$, aGNRs with $N_a = 3p+2$ dimer lines are metallic while the rest are semiconducting with energy gaps Δ given by the following equations[31]:

$$\Delta_{3p} = |t| \left(4cos \frac{\pi p}{3p+1} - 2 \right) \tag{1.15}$$

$$\Delta_{3p+1} = |t| \left(2 - 4cos \frac{\pi (p+1)}{3p+2} \right) \tag{1.16}$$

$$\Delta_{3p+2} = 0 \tag{1.17}$$

The previous picture is slightly revised when the electronic Hamiltonian is written beyond nearest-neighbor interactions and with the inclusion of edge effects towards the uplifting of metallicity and the formation of secondary bandgaps (of the order of few meV) for aGNRs with $N_a = 3p + 2$ dimer lines (see figure 1.4 for the bandstructure of aGNRs according a description that considers further-neighbor interactions as well as σ orbitals).

1.3.2 Zigzag confinement

Zigzag graphene nanoribbons (zGNRs) (see figure 1.3) are quasi-1D graphen-based structures identified by the number of zigzag chains N_z along the ribbon width that always have their two edge carbon atoms belonging to the different sublatices A and B (see eq. 1.4). This characteristic makes the imposition of

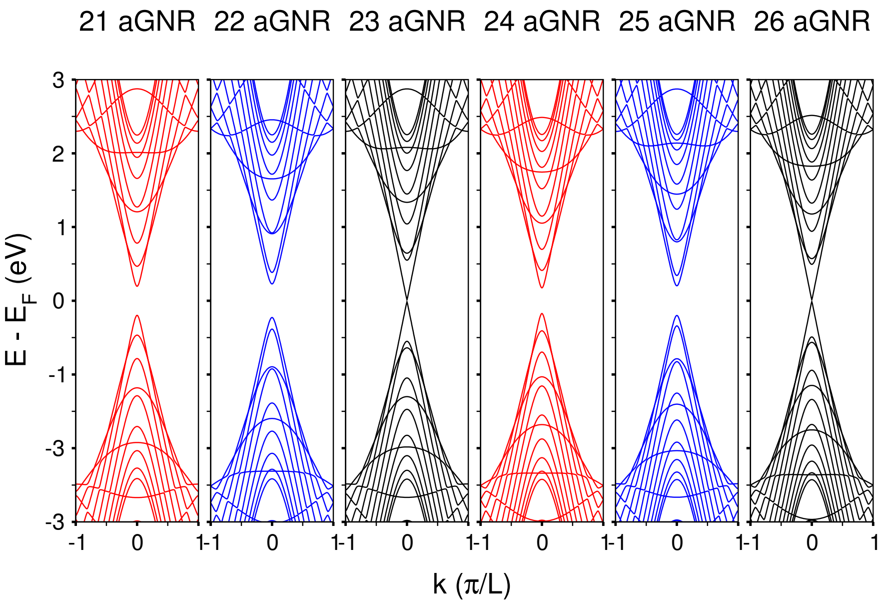

Figure 1.4: Bandstructure of armchair graphene nanoribbons - Energy dispersion relation of aGNRs within the Extended Hückel Theory for six different dimer line widths ($N_a = 21 - 26$). L is the lattice periodicity.

boundary conditions that nullify the wavefunction at the borders separate according to a reciprocal scheme where the wavefunction of sublatice A vanishes at the opposite B-type edge and vice-versa[31]. An analytical expression for the dispersion relation in zGNRs is not straightforward, however the numerical diagonalization of the Fourier-transformed $N_t \times N_t$ blocks of the nearest-neighbor TB Hamiltonian yields a bandstructure that presents some key characteristics: the Dirac points of two-dimensional graphene are projected at the $k = \pm\frac{2\pi}{3}$ points of the first 1D Brillouin zone, and b) from $k = \pm\frac{2\pi}{3}$ to $k = \pm\pi$, i.e. until the borders of the Brillouin zone there exist two partially flat degenerate bands with zero energy. The revisions in the previous picture inferred by higher order Hamiltonians show that the two degenerate subbands near the borders of the Brillouin zone slightly bend towards negative energies and do not maintain a zero value (see figure 1.5). A further inclusion of exchange interactions shows that the Γ point wavefunction above and below the charge neutrality level projects highly localized states at the edges of the zGNR with a ferromagnetic/anti-ferromagnetic order that open a small meV bandgap in between the two quasi degenerate subbands[99]. This last characteristic has driven a wide discussion on the possibility of spin-related phenomena based on the zigzag edges of GNRs (i.e. zGNRs as spintronic systems). However it should be noted that some of the conditions of suppression for edge magnetism are the presence of edge disorder[57], polihydrogenation of edge atoms[113] and finite temperatures, which are all commonly met in real GNR samples.

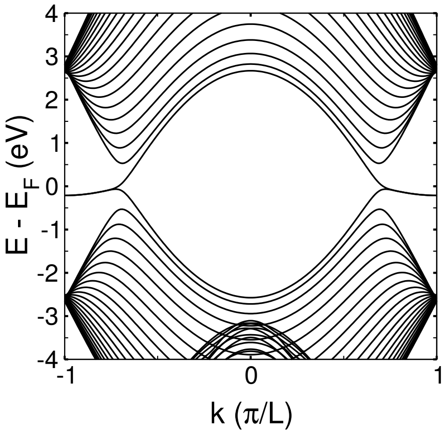

Figure 1.5: Bandstructure of zigzag graphene nanoribbons - Energy dispersion relation of a 22-zGNR ($N_z = 22$) within the Extended Hückel Theory. L is the lattice periodicity.

1.4 Nonideal low-dimensional graphene systems

As an one-atom-thick surface graphene is subject to the interaction with the surrounding environment. This interaction is bound to induce microscopic disorder in the electronic properties of this material. Already from the growth stage and notwithstanding the possibility to obtain high crystalline quality for micrometer scales, all popular growth techniques give rise to local or extended deviations from the ideal atomic structure: a) Micromechanical cleavage of graphite, also known as mechanical exfoliation or simply the "scotch-tape" technique, is uncontrollable, prohibiting for upscaling and produces samples that suffer point and Stone-Walles defects, as verified by low-energy transmission electron microscopy[76]. b) Epitaxial growths (both on SiC[32] and metallic substrates[106]) give origin to important interactions with the substrate that non-trivially compromise electronic and transport characteristics. c) Finally, chemical exfoliation leaves permanent chemical compounds that can become highly reactive with defects and lattice dislocations. A further source of structural disarrangement can be identified within patterning manipulations: up to date there exists no nanolithographic technique that imposes lateral confinement without inducing a great amount of edge disorder. Finally the step of device integration of graphene-based structures in nanoelectronics enhances perturbations withing a framework of interaction with both dielectrics and contacts, giving rise to important alterations in the conductance characteristics of this material[73].

Under this perspective the use of phenomenological approaches (e.g. the Anderson model[24]) for the inclusion of disorder in electronic transport properties of graphene-based systems[66] serve as a first approximation in the macroscale, but lack authoritativeness for the effects of local atomic reconstruction at the disordered area. The presence of defects and/or impurities, the interface with a particular substrate, the interaction with a metallic contact, the charge transfer induced by a local perturbation and in general all the structural/electronic deviations from bulkiness need more sophisticated approximations that consider both chemistry and electrostatics. It is therefore clear that a thorough understanding of different types of deviations from the ideal atomic/electronic structure, as well as their role in the shaping of the transport properties of graphene-based systems is of a fundamental importance.

1.5 Aims of this project

The goal of this PhD study is to investigate at an atomistic level the role of non-ideality on the electronic transport properties of systems based on graphene, with a specific focus on confined structures that could serve for a plausible device operation. An atomic reconstruction is necessary here for the encapsulation of localized or extended modifications of the structural and electronic symmetry that go beyond phenomenological approaches. Three different types of atomic/structural and electronic perturbations will be considered: a) perturbations induced by defects in the atomic lattice, b) perturbations induced by the interaction with the substrate, and c) perturbations induced by the coupling with the metallic contacts. For this study numerical codes will be implemented based on state-of-the-art Schrödinger/Poisson methodologies for the calculation of the electronic transport. Computational research will focus on: a) the reference formalism, b) the model Hamiltonians (both *ab initio* and semiempirical), and c) the numerical optimization and eventual parallelization techniques. A multiscale bottom-up approach will be defined for the evaluation and parameterization of semiempirical Hamiltonians by more accurate *ab initio* ones in order to enhance scaling and use extended spatial resolution without compromising on the chemical aspects of the atomic reconstruction for the disordered areas. Such an atomic resolution will allow considering the relation between the intrinsic geometry of the carbon-based structure (e.g. type and dimensions of the graphene nanoribbon) and the corresponding geometry alterations of the system's symmetry. Moreover electrostatic effects will be considered, e.g. the mechanism that regulates charge transfer between the metal-graphene junctions and their role in the conduction mechanism. To conclude, this study aims at studying various faults or perturbations in graphene-based systems in relation with device operation and upscaling.

1.6 Thesis outline

The second chapter of this thesis introduces a general quantum transport formalism that is able to encapsulate atomistic features that respect chemical bonding between different species as well as dynamic charge-transfer phenomena[1]. The basics of the non equilibrium Green's function formalism are derived analytically and its correlation with the Landauer-Buttiker approach for the calculation of conductance is presented. Different methods for the description of electronic Hamiltonians are analyzed with an accuracy/efficiency mismatch. Finally the insertion of electrostatics in the overall formalism and convergence/optimization numerical techniques are discussed.

The first part of the third chapter presents a multiscale approach for the calculation of the electronic structure and quantum transport using hexagonal graphene quantum dots as a case study. Both first-principles and semiemprirical Hamiltonians are considered. Using the *ab initio* calculations as a reference, the theoretical framework under which semiempirical methods adequately describe the electronic structure of the studied systems is recognized, thereon proceeding to the calculation of quantum transport. Attention is paid to the modeling of defect localization. The second part of the chapter treats electron backscattering phenomena during conduction for graphene nanoribbons with vacancy scatterers and dimensions within the capabilities of modern lithographic techniques. The analysis builds upon *ab initio* parameterized semiempirical models that break electron-hole symmetry and non equilibrium Greens function methods for the calculation of the conductance distribution. The detailed backscattering mechanism is extensively treated and considerations for a finite concentration of defects in micrometer scales are presented. Local charging aspects of defects are also discussed.

The first part of the forth chapter calculates quantum transport for metal and graphene nanoribbon heterojunctions within the atomistic self-consistent Schrödinger/Poisson scheme. Attention is paid on both the chemical aspects of the interface bonding as well the one-dimensional electrostatics along the ribbon length. Band bending and doping effects are discussed, that give rise to conductance asymmetries and a selective suppression of the typical 1D subband formation. Junction electrostatic effects are presented in the case of high work function *Au*, *Pd* and *Pt* electrodes, as well as for the low work function *Al* one. In

---

[1] Particularities of the theoretical formalism for the examination of specific problems treated in each chapter will be locally appended.

the second part of the chapter high-bias nonequilibrium aspects of conductance are discussed. In particular, the relationship between the device's local density of states and the electrochemical potentials of the contacts is examined within a perspective that has no equivalent in the semiclassical limit.

The fifth chapter treats electronic structure and quantum transport calculations for epitaxial graphene grown on SiC substrates. In the first part calculations for few-layer epitaxial graphene nanoribbons on the Si-face of SiC are presented. An atomistic description of both the graphene layers and the substrate is followed, while real/momentum space projections evidence the role of the heterostructures interface. Repercussions for the conducting capacity of the studied systems are discussed. Interface issues arising from this interaction (e.g. Fermi level pinning effects) are presented. Finally lateral scaling phenomena are analyzed showing the reduced role of confinement in these systems. In the second part of the chapter attention focuses on the structural and electronic properties of C-face grown epitaxial graphene. Based on *ab initio* calculations this part probes for the conducting and the magnetic properties of the graphene/substrate interface and discusses some fundamental differences with respect to the Si-grown case.

In the sixth chapter conclusions are presented along with a discussion of the overall results and a general outlook.

Chapter 2

Quantum transport formalism

2.1 Introduction

As the ongoing miniaturization trend of novel electronic devices reaches the nanoscale, the semiclassical model of diffusive transport is inadequate in explaining low-dimensional ballistic conductance aspects, whereas a fully atomistic and quantum description of the processes that govern conduction is indispensable. Indeed, device active component lengths are reaching the 10^{-10} m order and new conceptual issues arise in the theoretical description of transport like coherence/incoherence, quantum interference, confinement and tunneling. Such arguments were totally absent from the electronic engineering vocabulary until the late 80's. In this continuously evolving framework the need to efficiently address transport modeling becomes eminent both in terms of scientific progress as well as industrial challenge.

This chapter will present a review of the state-of-the-art quantum transport formalism for problems that diffusive and semiclassical models fail to address. This model is a combination of the Non-Equilibrium Green's Function (NEGF) methodology with the Landauer derivation of transmission and current. The power of such purely quantistic theory lies in its capacity to describe systems not only in the diffusive regime, but also systems where transport is ballistic and phase coherent. This conduction context is the one already prevalent for a number of active channel candidate materials like graphene (up to a submicrometer scale), carbon nanotubes, polyynes and other organic/inorganic molecules. It is therefore crucial for computer aided design techniques to integrate and enhance such theory for the appropriate study of electronic conduction in present and future nanoscale systems.

2.2 Green's function

A Green's function represents a response in one point of a conductor within a multi-terminal geometry from an exitation that takes places in a different point of the same conductor. Conceptually it is related to a scattering matrix (S-matrix), albeit its applicability is more general and powerful[1]. In our case, if the representation for the time-independent Schröedinger equation is

$$\hat{H}|\psi_\alpha\rangle = \epsilon_\alpha|\psi_\alpha\rangle, \tag{2.1}$$

$\hat{H}$ being the Hamiltonian operator and ϵ_α the energy eigenstate corresponding to wavefunction ψ_α, we can define the Green's function G as:

$$(\epsilon_\alpha\hat{I} - \hat{H})G(\vec{r}, \vec{r'}) = \delta(\vec{r} - \vec{r'}), \tag{2.2}$$

where δ represents the Dirac delta function and $\hat{I}$ is the unitary operator. The usefulness of the Green's function can be better understood if we consider a constant perturbation $|u\rangle$ that by acting on Schröedinger's equation gives rise to a perturbed wavefunction n:

$$\hat{H}|n\rangle = \epsilon|n\rangle + |u\rangle \tag{2.3}$$

We can rewrite the previous equation with the idea of introducing Green's function:

$$(\epsilon\hat{I} - \hat{H})|n\rangle = -|u\rangle \tag{2.4}$$

$$|n\rangle = -G|u\rangle \tag{2.5}$$

In this sense the Green's function is the response of a quantum mechanical system to a constant perturbation[86]. The main advantage of the calculation of Green's function with respect to the typical eigenvalue problem is its applicability to open systems used for the calculation of quantum transport (e.g. in a two terminal geometry, where a device part is embedded between two semi-infinite leads on the left and the right side). On the basis of this function a complete theory can be built, from which all necessary quantities for the calculation of transport can be obtained. The derivation of such formalism can take place in different ways, from the one-electron Schröedinger equation to a second quantization formalism[24]. Here, for simplicity's sake, we will choose the first approach and derive some inportant aspects of the NEGF formalism starting from a neat tight-binding picture.

---

[1] See ref. [24] for a detailed description of the S-matrix concept

2.3 Matrix Green's function for open systems

We consider an infinite one-dimensional discrete lattice where atoms with mass m are on lattice positions and are distant from neighboring atoms by a. In this sense each atom can be found at position $x = na$, where n is an integer. If we moreover consider that each atom interacts only with first neighbors and that it can be described by a single orbital centered at each atom, we can obtain the tight-binding Hamiltonian for this infinite system:

$$H = \begin{pmatrix} \ddots & \vdots & & & & & & & & \\ \dots & -t & \epsilon & -t & 0 & 0 & 0 & 0 & 0 & \dots \\ \dots & 0 & -t & \epsilon & -t & 0 & 0 & 0 & 0 & \dots \\ \dots & 0 & 0 & -t & \epsilon & -t & 0 & 0 & 0 & \dots \\ \dots & 0 & 0 & 0 & -t & \epsilon & -t & 0 & 0 & \dots \\ \dots & 0 & 0 & 0 & 0 & -t & \epsilon & -t & 0 & \dots \\ \dots & 0 & 0 & 0 & 0 & 0 & -t & \epsilon & -t & \dots \\ & & & & & & & & \vdots & \ddots \end{pmatrix} \tag{2.6}$$

Here the ϵ and t Hamiltonian values can derive by writing the system's one-electron Schröedinger equation with a simple finite difference method[1]. The discretization of the Hamiltonian matrix allows for a similar transformation also for the differential Green matrix of eq. (2.2):

$$(EI - H)G(E) = I \tag{2.7}$$

where E is the energy and I is the unitary matrix[2]. It would be therefore straightforward to introduce (2.6) in (2.7) and make the inversion in order to calculate Green's function, had the H matrix not been infinite.

If we now consider the generalized transport problem of a two-terminal geometry, where a finite device part is embedded between semi-infinite left and right contacts, we can write the Hamiltonian of the entire system as[86]:

$$H = \begin{pmatrix} H_L & \tau_L & 0 \\ \tau_L^\dagger & H_0 & \tau_R^\dagger \\ 0 & \tau_R & H_R \end{pmatrix} \tag{2.8}$$

---

[1] $t = \frac{\hbar}{2ma}$ and $\epsilon = 2t + U_n$, for derivation details please see reference [26]

[2] Equation 2.7 gives in fact two equivalent solutions, which are called the advanced (G^A) and the retarded (G^R) Green's functions and physically represent an incoming and an outgoing wave that are formed due to the same excitation. Mathematically we can obtain only one solution by imposing correctly the boundary conditions, which in our case is translated in adding or subtracting an infinitesimal imaginary part to the energy. It is also straightforward to show that $(G^R)^\dagger = G^A$.

Here, H_0 is the device Hamiltonian and $H_{L,R}$ are Hamiltonians relative to the contact regions. In this way, although contact subspaces are semi-infinite, the device subspace has a finite character. Similarly, we can separate the Green's function that corresponds to the device (G_0) and the contacts ($G_{L,R}$), and by substituting to equation (2.7) we have:

$$\begin{pmatrix} EI-H_L & -\tau_L & 0 \\ -\tau_L^\dagger & EI-H_0 & -\tau_R^\dagger \\ 0 & -\tau_R & EI-H_R \end{pmatrix} \begin{pmatrix} G_L & G_{L0} & G_{LR} \\ G_{0L} & G_0 & G_{0R} \\ G_{RL} & G_{R0} & G_R \end{pmatrix} = \begin{pmatrix} I & 0 & 0 \\ 0 & I & 0 \\ 0 & 0 & I \end{pmatrix} \tag{2.9}$$

Considering matrix multiplications with the second column of the Green matrix, we obtain the following equations:

$$(EI-H_L)G_{L0} - \tau_L G_0 = 0 \tag{2.10}$$

$$-\tau_L^\dagger G_{L0} + (EI-H_0)G_0 - \tau_R^\dagger G_{R0} = I \tag{2.11}$$

$$(EI-H_R)G_{R0} - \tau_R G_0 = 0 \tag{2.12}$$

In this set of equations (2.10) and (2.12) give matrices with (∞, N) dimensions, whereas (2.10) has (N, N) dimensions, where N is the number of device atoms. If we solve for G_{L0} and G_{R0} we have:

$$G_{L0} = (EI-H_L)^{-1}\tau_L G_0 = g_L \tau_L G_0 \tag{2.13}$$

$$G_{R0} = (EI-H_R)^{-1}\tau_R G_0 = g_R \tau_R G_0, \tag{2.14}$$

where $g_{L,R}$ are the Green functions of the left and right contact respectively. The next step should be to transform these two (∞, N) matrices into (N, N) ones and substitute them back to eq. (2.11) in order to obtain a finite device Green's function expression. Such a procedure usually takes advantage of the semi-infinite lattice symmetry of the two leads in order to make a k-space transformation of real-space matrices $g_{L,R}(\vec{r})$ into $g_{L,R}(\vec{k})$. It is afterwards easy to calculate the new matrices either analytically in the 1-D case[24] or iteratively in the 3-D case[117] and backspace substitute them in a real coordinate representation. The gain of such computationally overwhelming approach is that at the end of the story we can calculate (N, N) G_{L0} and G_{R0} matrices, and by substituting them into eq. (2.11) we get:

$$-\tau_L^\dagger g_L \tau_L G_0 + (EI-H_0)G_0 - \tau_R^\dagger g_R \tau_R G_0 = I \tag{2.15}$$

If we now define the *self-energies* of the two contacts as

$$\Sigma_L = \tau_L^\dagger g_L \tau_L \tag{2.16}$$

$$\Sigma_R = \tau_R^\dagger g_R \tau_R, \tag{2.17}$$

we can obtain the final version of the Green's function matrix G of the device (from now on we will call G the device's Green function) that takes also account for the interaction with the two contacts via the two self-energy terms:

$$G = (EI - H_0 - \Sigma_L - \Sigma_R)^{-1} \tag{2.18}$$

Conceptually one can think of $\Sigma_{L,R}$ as matrices that by being added to the bare device's Hamiltonian result in an effective Hamiltonian that accounts also for the exact effect of the leads. This concept is very powerful and can be extended to other types of interaction that take place in the device channel during conduction, e.g. electron-phonon or electron-electron interactions, although such extension results only in approximate descriptions, contrary to the ones obtained for the contacts. At this point, we have fixed a standard procedure for the calculation of Green's function of a two-terminal system, which could be easily expanded for multi-terminal geometries. From here on we can focus on the quantities relevant to transport that can be withdrawn from this function.

2.4 Device and contact spectral functions

Eq. (2.18) allows for a plausible computation of a two-terminal system due to its finite matrix character, even if conceptually the effect of the contacts is that of semi-infinite leads. Here we will define and discuss two quantities that are called the spectral functions A and Γ of the device and the contact respectively. The two relations are defined by the anti-Hermitian part of Green's function and the Self-energy's function respectively:

$$A = \imath(G - G^\dagger) \tag{2.19}$$

$$\Gamma \ = \imath(\Sigma - \Sigma^\dagger) \tag{2.20}$$

Conventionally only A is usually referred to as the spectral function and is related to the density of states of the system, while the Γ matrix is also called broadening matrix and physically represents the strength with which the contacts are bonded to the device.

For the derivation of the relationship between the spectral function and the density of states we need to expand Green's function in its eigenbasis. We start off by considering that the eigenfunctions of eq. (2.1) form an orthonormal set (being the eigenvectors of the Hamiltonian operator):

$$\langle \psi_\beta | \psi_\alpha \rangle = \delta_{\beta,\alpha}, \tag{2.21}$$

where $\delta_{\beta,\alpha}$ is the Kronecker delta. This allows us to expand Green's function on the basis of the eigenvectors. From eq. (2.7) and considering the retarded Green's function by adding an infinitesimal imaginary part to the energy we obtain:

$$G^R = \sum_\alpha \frac{|\psi_\alpha\rangle\langle\psi_\alpha|}{E + \imath\eta - \epsilon_\alpha}, \tag{2.22}$$

where η is a very small positive number and ϵ_α is the eigenvalue corresponding to eigenfunction $\psi_\alpha(\vec{r})$ From eqs. (2.19) and (2.22) we have:

$$A = \imath \sum_a |\psi_\alpha\rangle\langle\psi_\alpha|(\frac{1}{E + \imath\eta - \epsilon_\alpha} - \frac{1}{E - \imath\eta - \epsilon_\alpha}) \tag{2.23}$$

$$= \sum_a |\psi_\alpha\rangle\langle\psi_\alpha| \frac{2\eta}{(E - \epsilon_\alpha)^2 + \eta^2} \tag{2.24}$$

Since $\eta \rightarrow 0^+$, by integrating over E with a test function we obtain[86]:

$$A = 2\pi \sum_a \delta(E - \epsilon_\alpha)|\psi_\alpha\rangle\langle\psi_\alpha| \tag{2.25}$$

We know that the expression for the Density of States of the system is[26]:

$$D = \sum_a \delta(E - \epsilon_\alpha)|\psi_\alpha|^2 \tag{2.26}$$

From the last two equations we obtain:

$$2\pi D = Trace(A) \tag{2.27}$$

Similarly, the broadening matrix can be related with the electronic structure of the system in two qualitative aspects. As its name suggests, it provokes a broadening of the energy levels in the channel proportionally to the strength of the coupling between the device and the contacts. Furthermore, it introduces a finite lifetime for the electronic states (even if we have started deriving the formalism from the time-indipendent Schröedinger equation), suggesting that an electron introduced into a state at some point escapes to the contact. References [24, 26] propose a detailed mathematical and conceptual derivation of these physical aspects starting from simple toy models all the way up to second quantization arguments. Finally, a useful identity between A and Γ that can be found easily[24] is:

$$A = G\Gamma G^\dagger = G^\dagger \Gamma G \tag{2.28}$$

2.5 Electron density matrix

Next we will follow the derivation of the density matrix, whose diagonal elements give the electron density of the device. Let us start from a basic conceptual point. When contact reservoirs with different electrochemical potentials are attached to the device, each one of them tries to 'bring' the device to its own electrochemical potential by injecting or subtracting electrons. If we consider the system in equilibrium (i.e. the device part connected to just one contact) and take into account that the Hamiltonian is a hermitian matrix, the charge density matrix ρ is given by the relation[26]:

$$\rho = f_0(H - \mu I), \tag{2.29}$$

where μ is the electrochemical potential of the contact, H the Hamiltonian matrix, I the unitary matrix and

$$f_0(E - \mu) = \frac{1}{1 + e^{\frac{E-\mu}{k_B T}}} \tag{2.30}$$

is the statistical Fermi-Dirac distribution of electrons in the contact at energy E. Using now the fundumental property of the delta function:

$$\int_{-\infty}^{\infty} f(x)\delta(x - a)dx = f(a), \tag{2.31}$$

we can obtain from eq. (2.29):

$$\rho = \int_{-\infty}^{\infty} dE f_0(E - \mu)\delta(EI - H) \tag{2.32}$$

From a standard property of the delta function we have[25]:

$$2\pi\delta(x) = \lim_{\epsilon \to 0^+} (\frac{2\epsilon}{x^2 + \epsilon^2}) = \frac{i}{x + \imath 0^+} - \frac{i}{x - \imath 0^+} \tag{2.33}$$

In our case:

$$\delta(EI - H) = \frac{i}{2\pi}([(E + \imath 0^+)I - H]^{-1} - [(E - \imath 0^+)I - H]^{-1}) \tag{2.34}$$

From eqs. (2.32) and (2.34) we get:

$$\rho = \frac{1}{2\pi}\int_{-\infty}^{\infty} dE f_0(E - \mu)[\imath(G - G^\dagger)] \tag{2.35}$$

$$= \frac{1}{2\pi}\int_{-\infty}^{\infty} dE f_0(E - \mu)A \tag{2.36}$$

$$= \frac{1}{2\pi}\int_{-\infty}^{\infty} dE f_0(E - \mu)G\Gamma G^\dagger \tag{2.37}$$

If we generalize now the previous equation for the case of two (and futhermore easily expand for N) contacts we get the final form for the equation of the density matrix deriving directly by the NEGF formalism:

$$\rho = \frac{1}{2\pi}\int_{-\infty}^{\infty}(f_L G\Gamma_L G^{\dagger} + f_R G\Gamma_R G^{\dagger})dE \tag{2.38}$$

2.6 Transmission formalism

The term transmission formalism refers to the theory developed by Landauer[60] and afterwards expanded by Büttiker for the calculation of current in nanodevices on the basis of the summation of the *transmission probability* of each *transverse mode* of the device channel[24]. This can be better visualized from the well-known Landauer formula for the conductance:

$$G = \frac{2e^2}{h}MT \tag{2.39}$$

Here G is the conductance, M the number of transverse (or propagating) modes of the device and T the average probability that an electron injected from the one contact will transmit to the other. By defining $T(E) = MT$ as the total transmission probability of the channel for energy E it is straightforward to show[26] that in the case of coherent transport the total current can derive by the relation:

$$I = \frac{2e}{h}\int_{-\infty}^{\infty} T(E)[f_L - f_R]dE \tag{2.40}$$

Here the contact Fermi functions represent the driving force for the propagation of current[27] in the sense that only carriers with energies in-between the electrochemical potentials of the two contacts participate in the conduction process. This implies that the usual idea that considers the electric field acting on all electrons as the primary reason for transport is simply inacurate. Having established this, the point is to show how we can relate the transmission and the NEGF formalisms.

Under non-equilibrium, we can think of the current that passes from a contact to the device as the difference of an influx and an outflux current[25]. We can write the outflux from the device to the left contact as:

$$I_{out_L} = \frac{e}{h}\int_{-\infty}^{\infty} Trace(\Gamma_L \rho)dE, \tag{2.41}$$

and the outflux from the device to the right contact as:

$$I_{out_R} = \frac{e}{h}\int_{-\infty}^{\infty} Trace(\Gamma_R \rho)dE, \tag{2.42}$$

where $\frac{\Gamma_{L,(R)}}{h}$ represent the *rate* at which electrons escape from the device to the left (right) contact (considering that Γ matrices have the dimensions of energy) and ρ is the density matrix given by eq. (2.38). Now we can think of the influx current from the contacts to the device as equal to the outflux current we would have if the device was in equilibrium with each one of the contacts:

$$I_{in_L} = \frac{e}{h}\int_{-\infty}^{\infty} Trace(\Gamma_L \rho_{eq})dE \tag{2.43}$$

$$I_{in_R} = \frac{e}{h}\int_{-\infty}^{\infty} Trace(\Gamma_R \rho_{eq})dE \tag{2.44}$$

where

$$\rho_{eq} = \frac{1}{2\pi}\int_{-\infty}^{\infty}(f_L[G\Gamma_L G^{\dagger} + G\Gamma_R G^{\dagger}])dE \tag{2.45}$$

$$= \frac{1}{2\pi}\int_{-\infty}^{\infty}(f_R[G\Gamma_L G^{\dagger} + G\Gamma_R G^{\dagger}])dE, \tag{2.46}$$

since in equilibrium conditions $\mu_L = \mu_R$. The net current for contact L is:

$$I = I_{in_L} - I_{out_L} = \frac{e}{h}\int_{-\infty}^{\infty} Trace(\Gamma_L G\Gamma_R G^{\dagger})(f_L - f_R)dE \tag{2.47}$$

With a similar procedure for the second contact we can derive that:

$$I = I_{in_R} - I_{out_R} = \frac{e}{h}\int_{-\infty}^{\infty} Trace(\Gamma_R G\Gamma_L G^{\dagger})(f_L - f_R)dE \tag{2.48}$$

If we multiply equations (2.47) and (2.48) with 2 in order to account for the spin factor and compare them with (2.40), we can write the transmission probability in terms of Green's formalism quantities:

$$T(E) = Trace(\Gamma_L G\Gamma_R G^{\dagger}) \tag{2.49}$$

$$= Trace(\Gamma_R G\Gamma_L G^{\dagger}) \tag{2.50}$$

$$= Trace(\Gamma_L A_R) \tag{2.51}$$

$$= Trace(\Gamma_R A_L) \tag{2.52}$$

The coupling between Green's and Landauer's formalism in the coherent limit is also known as the NEGF-Landauer approach.

2.7 Electronic Hamiltonians

A key issue that precedes quantum transport is the correct treatment of the electronic structure of the system in study by writing a proper electronic Hamiltonian.

This aspect is fundamental since a proper input in the transport formalism is a prerequisite for correct conduction outcomes. Usually there are two common approaches to this problem with an accuracy/efficiency mismatch between them, i.e. *ab initio* and semiempirical approaches. *Ab initio* (or *first principles*) methods use only fundamental physical constants and calculate self-consistently the wavefunction of the studied system on the basis of a variational principle of energy minimization. A particular category of *ab initio* methods is the Density Functional Theory (DFT), where the fundamental quantity is the electron probability density ρ and not the electronic wavefunction. *Semiemprirical* methods on the other hand use simpler Hamiltonians that are parameterized on the basis of experimental data or first-principles calculations. In this case no self-consistent loop is necessary for the calculations, enhancing computational efficiency. However, the static character of such Hamiltonians imposes limitations in their capability to describe systems outside the scope of the initial parameterization. In this sense evaluation or calibration of semiempirical models is necessary prior to their use in electronic structure and quantum transport calculations of a particular system. Here we will see the basic concepts of two methods widely used throughout the this work, i.e. the first principles DFT method and the semiempirical Extended Hückel Theory (EHT).

2.7.1 Density Functional Theory

DFT is founded on the Hohenberg-Kohn theorems and the Kohn-Sham (KS) formulation that allows for its practical use for the calculation of the electronic structure. The first Hohenberg-Kohn theorem states that the ground state electronic energy E_0 is a unique functional of the ground-state electron probability density ρ_0, i.e. $E_0 = E_0[\rho_0]$ (see ref. 71 for the proof). Therefore DFT attempts to calculate ground-state properties from ρ_0. We start by the average energy for the ground state of a system with n electrons:

$$E = \overline{T} + \overline{V}_{Ne} + \overline{V}_{ee}, \tag{2.53}$$

where $\overline{T}$ is the kinetic energy, $\overline{V}_{Ne}$ are the electron-nuclear attractions and $\overline{V}_{ee}$ are electron-electron interactions. All three terms of the previous equation are determined by the ground-state wavefunction, which in turn, according to the first theorem is a functional of ρ_0. Therefore:

$$E_0 = E_u[\rho_0] = \overline{T}[\rho_0] + \overline{V}_{Ne}[\rho_0] + \overline{V}_{ee}[\rho_0]. \tag{2.54}$$

Considering adiabatically fixed locations for the nuclei (i.e. the BornOppenheimer approximation) we have:

$$\overline{V}_{Ne} = \langle\psi_0|\sum_{i=1}^{n} u(\vec{r_i})|\psi_0\rangle = \int \rho_0(\vec{r})u(\vec{r})d\vec{r}, \tag{2.55}$$

where $u(\vec{r_i})$ is the external nuclear attraction potential energy for an electron located at $\vec{r_i}$:

$$u(\vec{r_i}) = -\sum_{\alpha} \frac{Z_\alpha}{r_{i\alpha}}, \tag{2.56}$$

and α denotes the atomic sites. The complete formulation of equation 2.54 reads[71]:

$$E_0 = E_u[\rho_0] = \int \rho_0(\vec{r})u(\vec{r})d\vec{r} + \overline{T}[\rho_0] + \overline{V}_{ee}[\rho_0] = \int \rho_0(\vec{r})u(\vec{r})d\vec{r} + \overline{F}[\rho_0], \tag{2.57}$$

where $\overline{F}[\rho_0] = \overline{T}[\rho_0] + \overline{V}_{ee}[\rho_0]$ is an unknown functional of the sum of the kinetic-energy terms and electron-electron repulsions.

The second Hohenberg-Kohn theorem (also known as the Hohenberg-Kohn variational theorem) states that the exact ground-state electron density minimizes the energy functional $E_0 = E_u[\rho_0]$ (see ref. 71 for the proof). In principle, if we know ρ_0 it is possible to calculate all the ground-state properties from it without having to calculate the wavefunction. However, the Hohenberg-Kohn theorems do not tell us how to calculate E_0 from ρ_0, since $F[\rho_0]$ is unknown. The solution to this problem comes with the Kohn-Sham method that translates a problem of n interacting electrons in a noninteracting one by the definition of a fictitious reference system that experiences an external potential $u_s(\vec{r_i})$ that makes the ground-state probability density $\rho_s(\vec{r})$ equal to the exact ground-state density $\rho_0(\vec{r})$ of the interacting system. Since the electrons do not interact in the reference system, single-electron orbitals should derive from:

$$\left(-\frac{\hbar^2}{2m}\nabla^2 + u_s(\vec{r})\right)\phi_i(\vec{r}) = \epsilon_i\phi_i(\vec{r}), \tag{2.58}$$

where the electron density ρ_s is:

$$\rho_s(\vec{r}) = \sum_{i=1}^{n} |\phi_i(\vec{r})|^2 . \tag{2.59}$$

In order to calculate the rest of the unknown quantities of eq. 2.57 Kohn and Sham defined

$$\Delta\overline{T}[\rho] \equiv \overline{T}[\rho] - \overline{T}_s[\rho] \tag{2.60}$$

as the difference in the ground-state average electronic kinetic energy between the interacting and the noninteracting systems. The $\overline{T}_s[\rho]$ term can then be calculated by the KS orbitals as:

$$\overline{T}_s = \sum_{i=1}^{n} \int \phi_i^*(\vec{r}) \left(-\frac{\hbar^2}{2m}\nabla_i^2\right) \phi_i(\vec{r}) d\vec{r}. \tag{2.61}$$

They moreover defined:

$$\Delta\overline{V}_{ee}[\rho] \equiv \overline{V}_{ee}[\rho] - \frac{e^2}{2}\int\int \frac{\rho(\vec{r_1})\rho(\vec{r_2})}{\vec{r}_{12}} d\vec{r}_1 d\vec{r}_2, \tag{2.62}$$

where $\vec{r}_{12}$ is the vector showing two different points in space and the second term represents the Coulomb energy of the noninteracting system.

Substituting back to equation 2.57 we get:

$$E_0 = E_u[\rho] = \int \rho(\vec{r})u(\vec{r})d\vec{r} + \sum_{i=1}^{n} \int \phi_i^*(\vec{r}) \left(-\frac{\hbar^2}{2m}\nabla_i^2\right) \phi_i(\vec{r}) d\vec{r} + \tag{2.63}$$

$$+\frac{e^2}{2}\int\int \frac{\rho(\vec{r_1})\rho(\vec{r_2})}{\vec{r}_{12}} d\vec{r}_1 d\vec{r}_2 + \Delta\overline{T}[\rho] + \Delta\overline{V}_{ee}[\rho] \tag{2.64}$$

With the definition of the exchange-correlation energy functional $E_{xc}[\rho]$ as:

$$E_{xc}[\rho] = \Delta\overline{T}[\rho] + \Delta\overline{V}_{ee}[\rho], \tag{2.65}$$

we have just one unknown functional in equation 2.63. From 2.65 we can define the exchange-correlation potential as:

$$u_{xc}(\vec{r}) = \frac{\delta E_{xc}[\rho](\vec{r})}{\delta\rho(\vec{r})}, \tag{2.66}$$

and the effective potential $u_s(\vec{r})$ as:

$$u_s(\vec{r}) = u(\vec{r}) + e^2 \int \frac{\rho(\vec{r_2})}{\vec{r}_{12}} d\vec{r}_2 + u_{xc}(\vec{r}) \tag{2.67}$$

During the last decades there have been numerous attempts to approximate the previous potential, with the majority entering into two general categories of the Local Density Approximation (LDA) and the General Gradient Approximation (GGA). It should be noted that once the exchange-correlation potential has been calculated and the electron density is found within a variational approach, this is no longer the exact ground-state density of the system, but a good approximation of it, since the exchange-correlation potential is by itself an approximation. Moreover KS wavefunctions and eigenstates have an auxiliary character and do not represent their real counterparts. However it should be noted that they usually approach the real eigenfunctions/eigenstates. Finally, a brief remark for the high usability of the DFT theory in state-of-the-art electronic structure calculations should be made, which outdates most other quantum chemical theories.

2.7.2 Extended Hückel Theory

The EHT method is one of the most important one-electron molecular orbital semiempirical theories for the calculation of the electronic structure. It is based on the approximation of treating valence electrons separately from the rest and uses Slater-type atomic orbitals as basis functions for the construction of the Hamiltonain type:

$$f^{\zeta}_{nml}(r, \theta_1, \theta_2) = N r^{n-1} e^{-\zeta r} Y^m_l(\theta_1, \theta_2), \tag{2.68}$$

where n, m, l are the principle, azimuthal and magnetic quantum numbers and Y^m_l are the spherical harmonics. The molecular orbitals are then formed as a linear combination of the atomic orbitals f:

$$\phi_i = \sum_i c_i f, \tag{2.69}$$

where coefficients c_i and exponents ζ_i are fitted for the individual basis functions to match bandstructure data[64]. Diagonal Hamiltonian elements are usually calibrated by experimental or first-principles obtained values of the difference between ionization potential and electron affinity:

$$H_{mm} = E_{mm}. \tag{2.70}$$

For the off diagonal elements the following expression is used:

$$H_{mn} = \frac{1}{2}K(H_{mm} + H_{nn})S_{mn}, \tag{2.71}$$

where K is the Wolfsberg-Helmholtz constant (usually having values within 1 and 3) and S_{mn} is the overap matrix between orbitals ϕ_m and ϕ_n:

$$S_{mn} = \int \phi_m^*(\vec{r})\phi_n(\vec{r})d^3\vec{r}. \tag{2.72}$$

The power of the EHT lies its good capacity to describe qualitative characteristics of more accurate Hamiltonians with a real-orbital localized basis set that enhances transferability and an overall reduced computational cost.

2.8 Nonequilibrium electrostatics

A key characteristic of conduction is that devices are at a nonequilibrium conditions due to the separation of the electrochemical potentials of the contacts by the application of bias. Nonequilibrium charging effects are therefore crucial for the correct description of the transport process. The insertion of charging effects in the NEGF formalism simply takes places by the addition of a self-consistent potential U_{sc} that is a functional of the electron density to the bare device Hamiltonian[26]:

$$H = H_0 + qU_{sc}, \tag{2.73}$$

where H_0 is the device Hamiltonian without the presence of electron-electron interactions and q is the electronic charge. The calculation of U_{sc} takes places by numerically solving the Poisson equation:

$$\nabla^2 U_{sc} = -\rho_f/\epsilon, \tag{2.74}$$

where ρ_f are mobile charges that can be easily calculated within the NEGF[40] and ϵ is the dielectric constant of the material in which the device part is embedded. Computationally, the calculation of eq. 2.74 takes place within finite difference/elements methodologies in real or momentum space grids using appropriate boundary conditions (usually Neumman and Dirichlet ones) that account for the different contact configurations (e.g. source, drain or gate contacts).

2.9 Numerical optimizations

The underlying structure of a computational code is largely based on iterative matrix algebra operations (e.g. matrix diagonalizations and inversions) that scale as $\sim N^3$, where N are matrix dimensions. It becomes evident that computational overloading can easily result for systems of moderate dimensions (e.g. if we consider a graphene nanoribbon with 1000 atoms and describe the electronic structure within the EHT using a $2s2p^3 3d^5$ basis we obtain matrices with [9000,9000] dimensions). To override related difficulties common computational techniques usually fall within two general categories, i.e. optimization algorithms and parallelism.

Most optimization algorithms take advantage of the sparsity in the matrices used within the transport formalism (e.g. Hamiltonian and Green matrices) in order to achieve a reduction in the required operations that goes to a linear scaling of matrix operation with the system size, known as $O(N)$ techniques[89, 90]. The underlying algorithms create submatrices with tridiagonal blocks and use the particular properties of the respective matrices to fasten operations. Further optimization can be obtained for particular problems like the calculation of the surface Green matrix[95] that involves costly iterative operations, while energy integrals can be enhanced by division between real and complex contour integration[11]. Finally, use of optimized computational linear algebra libraries (e.g. LAPACK and BLAS) sensibly reduces the processing time.

Parallelism can be achieved at different levels within a quantum transport code. The first level introduces parallelism for the costly matrix operations like diagonalizations and inversions, since the latter occupy the major part of the runtime. A second order scaling can be achieved by the introduction of parallelism for energy integrals, i.e. with the assignment of different energy areas to different processors and linear recombination of the results in the end of each iterative loop. The main drawback of parallelism lies in the need to operate in parallel multicore shared or distributed memory architectures, while the different parallelism protocols (e.g. MPI and OpenMP) give rise to architecture specific codes that lack transferability.

2.10 Discussion

The real power of the NEGF formalism is that it can also describe inelastic and incoherent transport. This means that e.g. a description of electron-phonon scattering interactions is plausible in a neat way by introducing an extra self-energy term in the calculation of the Green's function[1]. Also it can be detached from the Landauer formula and calculate the current for systems where phase-breaking mechanisms are present. The quantities deriving from the NEGF theory are not limited to the ones seen in the previous paragraphs[24, 26, 27]. This chapter has been intensionally kept at an introductory level, and this has also imported conceptual approximations in the derivations of the NEGF formula. For a thorough and exact insight on the formalism one has to harness the power of second quantization mathematics[26].

Criticism to the NEGF-Landauer formalism derives from the intrinsic single-electron picture of the transmission probability that does not take into account many-body effects that are enhanced in the case of the nanoscale due to the viscous nature of the electron liquid[110]. This problem is non solved by simply considering a Hamiltonian that incorporates many-body effects (e.g. a DFT Hamiltonian) since the Landauer-Buttiker approach derives the overall conductance by single-particle contributions. However, post NEGF-Landauer formalisms based on the time-dependent DFT which do incorporate many-body interactions at all possible levels[110] give rise to results that rather appear as corrections to the NEGF-Landauer picture rather than a complete reformulation of the transport theory.

In summary, the NEGF formalism can be considered a complete and mature quantum mechanical theory for the calculation of transport in nanodevices that can incorporate a number of scattering mechanisms (contacts, electron-electron, electron-phonon) efficiently. Derivation of all relative to transport quantities can take place with the appropriate writing of the Green matrix for the studied system, that involves the electronic Hamiltonian written at an appropriate basis set along with information on electron-electron interactions (self-cosistent potential U_{sc}), scattering by the contacts (self-energy matrices $\Sigma_{L,R}$) and other scattering mechanisms (self-energy matrices Σ_{ext}). From the Green matrix derivation of the density of states, trasmsission probability, charge carrier density and current becomes straightforward.

Chapter 3

Vacancies in confined graphene structures

3.1 Introduction

Graphene is a stable, two-dimensional, sp^2-bonded carbon allotrope system with exceptional electrical, mechanical and optical properties[80, 115]. Particularity stems from the almost linear dispersion relation in momentum space close to the Fermi level, where valence and conduction bands meet exactly at the charge neutrality point. Provided that a viable method of controllable band-gap engineering can be obtained, graphene can also constitute a valid alternative for post-Si CMOS technology. Graphene's peculiar conduction properties can be highly compromised by the presence of disorder in terms of local scattering centers (e.g. defects[19]) or substrate-induced interference[30, 32]. On the other hand, disorder by means of chemical functionalization has been proposed to enhance device functionality by controlling the opening of exploitable gaps. Dopants can either act directly on the electronic structure[9, 43], or induce backscattering effects within the transport process[5]. As a consequence, the study of conduction in disordered graphene systems acquires a double significance: on the one hand it becomes crucial for performance-related characteristics, while on the other it can be used to address band-gap tailoring issues.

Vacancies can make part of crystalline graphene as production faults of the mechanical or the epitaxial growth process. Their presence has been experimentally verified by transmission electron microscopy[76], whereas structural, electronic and magnetic properties have been theoretically investigated at a full quantum scale[13, 55, 85, 88, 116]. Modeling within the nearest-neighbor tight-binding formalism is straightforward: a local point potential $U \to \infty$ is introduced on the vacancy site that forbids hoppings to and from neighboring sites[88]. As a result a semi-localized state appears at the Fermi level of the system with a C_3 point symmetry and a local spin[85, 88]. The positioning of this zero-energy mode is highly related to the electron-hole symmetrical description of the bandstructure under this approach. By considering a next-to-near neighbor in the same type of model, valence and conduction band mirror-symmetry breaks, and the defect state looses its high-symmetry allocation. Accurate *ab initio* calculations show that the resonance of this mode is located at energies that do not coincide with the charge neutrality point[13]. Pereira *et al.*[88] have argued that the breaking of electron-hole symmetry in the presence of a point defect can induce further alterations in the electronic structure by means of other semi-localized eigenstates, implying that the perturbation induced by the point defect is not constrained to a single energy but it expands within the energy spectrum. Unlikely, a clear allocation of the role of such perturbation with respect to the conduction properties of graphene-based systems still lacks.

This chapter will focus on the problem of defect localization in zero and one-dimensional graphene structures. The aim here is twofold: investigate the electronic structure alterations that arise due to the presence of defects in these systems and establish a clear methodological framework that enables simpler semiempirical approaches to capture qualititative aspects of more sophisticated *ab initio* descriptions for an eventual use in massive quantum transport calculations. In the second part of this chapter this methodology will be implemented for large-scale quantum transport calculations in vacancy-damaged graphene nanoribbons.

3.2 Vacancies in graphene quantum dots

We start off by implementing a bottom-up multiscale approach for the modeling of defect localization graphene quantum dots with a hexagonal symmetry, by means of density functional and semiempirical approaches. Using the *ab initio* calculations as a reference, we recognize the theoretical framework under which semiempirical methods describe adequately the electronic structure of the studied systems and thereon proceed to the calculation of quantum transport within the non-equilibrium Green's function formalism. The study's groundwork focuses on: (i) the structural characteristics, and (ii) the methodological approach. The islands under consideration are the coronene molecules[34, 41] with a general chemical type of $C_{6n^2}H_{6n}$ in a pure, defected (with a single vacancy) and hydrogen functionalized form. These can be thought of as planar complexes of benzene rings that grow rotating around a central benzene ring, forming six hydrogen-passivated zigzag edges (see fig. 3.1). Methodologically, electronic structure is initially studied with DFT while optical properties are calculated within the time-dependent density functional theory (TD-DFT). These results serve as a reference for the comparison with similar calculations by means of two parameterized semiempirical methods: (i) the extended Hückel (EH) theory [56] and (ii), the next-neighbor tight-binding model. As soon as a proper functional framework is identified for the semiempirical approaches the study proceeds with the calculation of electronic transport. Particular attention is paid to the effect of defect localization both within a level of characterization as well as model calibration, since the computational results indicate impurity-like behavior of single vacancies in these systems. Conceptually, although the final objective is physical (quantum transport modeling in graphene islands), the basis is founded on chemistry (multiscale comparative analysis of the electronic structure).

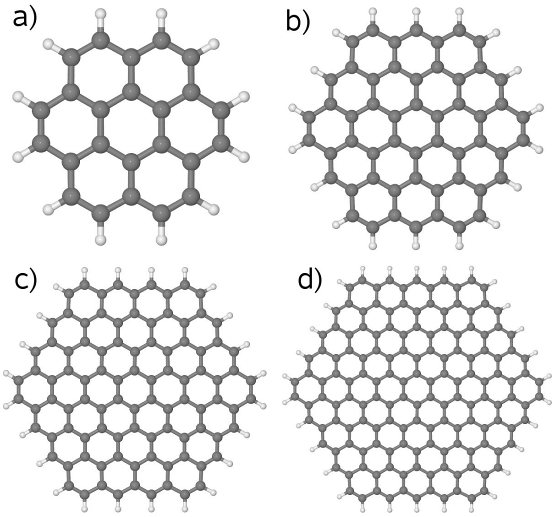

Figure 3.1: Hexagonal graphene quantum dots - $C_{6n^2}H_{6n}$ molecular complexes: a) $C_{24}H_{12}$ (coronene, n=2), b) $C_{54}H_{18}$ (coronene 19, n=3), c) $C_{96}H_{24}$ (coronene 37, n=4), d) $C_{150}H_{30}$ (coronene 61, n=5)

3.2.1 Methodology

Geometry relaxation and electronic structure properties (eigenvalues, eigenfunctions, density of states) of various $C_{6n^2}H_{6n}$ clusters are extrapolated by DFT calculations on a split-valence double-zeta (3-21g [7, 45, 91]) and a minimal (STO-3G [21, 51]) basis set, as implemented in the GAUSSIAN code[33]. The semiempirical three-parameter hybrid nonlocal exchange and correlation functional of Becke and Lee, Yang and Parr[4, 68, 104, 112] (B3LYP) has been chosen here for its capacity to predict a large range of molecular properties for aromatic systems[10, 78]. Additional optical properties (excitation energies, fundamental optical gaps) are calculated within a TD-DFT approach for comparison between theory and experiment. Electronic structure results are then confronted with similar ones obtained by two semiempirical methods[28, 117] that also present a precision/efficiency mismatch among them: (i) the extended Hückel method, and (ii) a next-neighbor tight-binding model. In the case of the EH method three distinct parameterizations are used: (i) the first one considers a standard valence $2s2p$-basis set of single-ζ Slater orbitals for C atoms, principally deriving from the initial values used by Hoffmann[56](EH-sp from now on)[1]. (ii) The second one is a $2s2p3d$-based parameterization with valence/polarization double-ζ exponents and C parameters fitted to recreate the bandstructure of two-dimensional graphene as given by DFT calculations[16, 17, 64] (EH2-spd from now on). (iii) The third parameterization derives in the similar way to the second one, whereas here the polarization orbitals are absent[17, 64](EH2-sp from now on). For the first-neighbor TB model a standard $t_0 = 2.7eV$ C-C hopping integral is used, while vacancies are approximated with the insertion of a local point potential $U \rightarrow \infty$ (unless explicitly referred to in the text). Although all methods construct the molecular orbitals on the basis of the linear combination of atomic orbitals there is a distinct difference in the level of accuracy that each method delivers. In the DFT case the basis set is comprised of Gaussian-type orbitals with weighting coefficients that are both calculated self-consistently in order to reproduce the best approximation of the exact ground state density of the system. In the EH case the bases are nonorthogonal Slater-type orbitals with fixed weighting coefficients that have been parameterized on the basis of experimental data or first principles calculations. Finally in the TB case no real orbitals exist and the system Hamiltonian is constructed by a next-neighbor scheme that through a proper choice of the hopping integral is representative of the π-orbital in the sp^2 hybridization. Naturally, the level of computational efficiency is the inverse, ranging from molecular (DFT) to mesoscopic (TB).

Electronic structure results are obtained through a direct diagonalization of the respective Hamiltonian matrix. Comparisons take place in terms of highest occupied molecular orbital (HOMO) and lowest unoccupied molecular orbital (LUMO) gaps, energy eigenstates ϵ_α and their respective eigenfunctions Ψ_α. The local density of states LDOS($\vec{r}, E$) at the positions $\vec{r}$ of the device atoms at energy E is calculated as:

$$LDOS(\vec{r}, E) = \sum_\alpha |\Psi_\alpha(\vec{r})|^2 \delta(E - \epsilon_\alpha), \tag{3.1}$$

where δ is the Delta function, while summing over all atoms gives the total density of states (DOS) of the molecular systems at this energy.

---

[1] $Eon - site(C_s) = -21.4eV$, $Eon - site(C_p) = -11.4eV$, $Eon - site(H) = -13.6eV$, $\zeta(C_s) = 1.625$, $\zeta(C_p) = 1.625$, $\zeta(H) = 1.3$, $coeff(C_s) = 1$, $coeff(C_p) = 1$, $coeff(H) = 1$, $K = 1.75$

Quantum transport is calculated within the non equilibrium Green's function formalism[25]. In particular, the method is based on the single particle retarded Green's function matrix $G = [ES - H - \Sigma_L - \Sigma_R]^{-1}$, where E is the energy, H and S are the device Hamiltonian and the overlap matrix respectively (written in an appropriate basis set), while $\Sigma_{L,R}$ are the self-energy matrices that account for the effect of scattering due to the left (L) and right (R) contacts. In the TB case the overlap matrix coincides with the unitary one. The $\Sigma_{L,R}$ terms can be expressed as $\Sigma = \tau g_s \tau^\dagger$, where g_s is the surface Green function specific to the contact type and τ is the Hamiltonian relative to the interaction between the device and the contact. The calculation of the Green's function permits for the evaluation of all the quantities of interest for conduction, e.g. the device spectral function is the anti-hermitian part of the Green's function $A = \imath(G - G^\dagger)$ from which the Density of States can be obtained as $D(E) = \frac{1}{2\pi} Trace(AS)$. Moreover in the coherent transport regime, the expression used for the zero-bias transmission probability reads $T(E) = Trace(\Gamma_L G \Gamma_R G^\dagger)$, where $\Gamma_{L,R} = \imath(\Sigma_{L,R} - \Sigma_{L,R}^\dagger)$ are the contact spectral functions.

In this study $C_{24}H_{12}$, $C_{54}H_{18}$, $C_{96}H_{24}$ and $C_{150}H_{30}$ complexes have been considered in their pure, defected (with a single vacancy) and hydrogen functionalized form. All structures have been relaxed by DFT molecular dynamics while relaxation information is also used by the EH method. In the case of TB an ideal reconstruction of the molecular structure is considered since the latter does not account for interatomic distances. Finally, for the quantum transport calculations the islands are placed within two semi-infinite $Au(111)$ metallic planes (directly considered in the case of EH, appropriately fitted in the case of TB[28]) in a molecular bridge configuration.

3.2.2 Comparative analysis of structural and electronic properties

A proper treatment of quantum transport modeling has to take care of both quantitative and qualitative aspects of the electronic structure of a molecular system. In this sense, if the value of the HOMO-LUMO gap is a quantitative feature, the form of the HOMO and LUMO wavefunctions, or similarly, the local density of states of the structure for energies near the HOMO/LUMO states are qualitative characteristics. It can be argued that in terms of conduction, although the former can influence scaling, the latter can affect the shape of the current-voltage curve. In addition, higher-bias conduction requests accuracy for entire conduction/valence bands. Such considerations imply that a proper description of the local density of states of a molecular system by means of a quantum chemical method can be fundamental for the correct modeling in terms of quantum transport. This section examines electronic configuration aspects one by one.

3.2.2.1 Geometry relaxation

From a numerical point of view, distance between the atomic sites influences the electronic structure of a molecular system by affecting both overlap and Hamiltonian matrix elements. Geometry relaxation with the DFT method has shown that near the island edges, complex distance polymerization effects can be observed that tend to periodically increase/decrease C-C bonding for about 5% from the equilibrium distance ($C - C_{equil} \approx 1.42\text{Å}$). Such feature tends to propagate also in the inner parts of the clusters albeit in a continuously decreasing extent, while only the central benzene rings result having equal interatomic C distances. Distance shortenings due to hydrogen passivation have been also observed in the case of graphene nanoribbons[99], whereas the effect there is localized near the edges. From a methodological point of view, variable bond-lengths can have a practical consequence in the parameterization of the hopping integral for the TB method, where for accuracy's sake an evaluation of each atomic pair distance should take place prior to the assignment of the integral value (in this sense the method becomes similar to the single π-orbital Hückel one). If such information is not available inaccuracies in the TB Hamiltonian can occur. It can be argued that futher complications in the correct estimation of interatomic distances have to be considered in the case of interaction between the molecular structures and a substrate (e.g. for the reproduction of laboratory conditions[20, 96, 122]). In this case combined molecular/substrate atomistic modelling should enlight interface bonding interactions for both the chemical and the structural characteristics.

3.2.2.2 Energy levels

A well-known aspect of geometrical symmetry is the presence of orbital degeneracies. Such feature is captured by all methods for the pure structures, from DFT to TB. Eventually, symmetry breaking events (e.g. the presence of a single vacancy) lift such degeneracies and split the respective energy levels. In this subsection we visualize characteristics of the eigenvalue spectrum in a full quantum scale, in terms of energy gaps and state alignment over the energy axis. Figure 3.2 shows HOMO-LUMO gaps for pure and defected structures by means of DFT (both 3-21g and STO-3G), EH2-spd, EH-sp and TB, while EH2-sp results are similar to EH2-spd and are not shown. Regarding the pure structures the following observations can be made: (i) the gap value given by the DFT is bigger than those obtained by the semiempirical methods. This aspect is not directly related to the exchange-correlation absence in the semiempirical cases (since parameterization can take place on the basis of *ab initio* calculations) but with the chemical environment considered for the parameterization, which usually considers bulk structures where the effect of confinement cannot be evaluated. It is moreover interesting to evidence that the minimal basis set in the DFT method slightly overestimates this value with respect to the 3-21g case. (ii) The EH2-spd method with its orbital foundation and sp^2-hybridized calibration approximates better the DFT results with respect to the other semiempirical methods. (iii) Albeit the clear difference in terms of the methodology, results by EH-sp and TB are very similar. It should be noted here that a rough method to bring semiempirical models closer to first principles calculations is by globally fitting the hopping integral (or similarly the Wolfsberg-Helmholtz K constant for EH). However in this case the parameterization looses any meaning outside the designated geometrical environment.

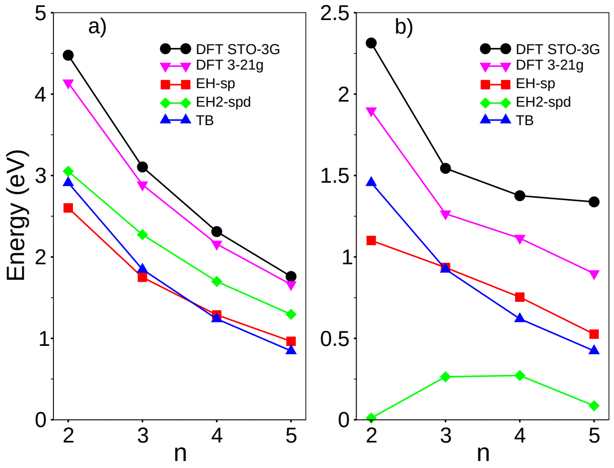

Figure 3.2: Energy gaps in hexagonal graphene quantum dots - $C_{6n^2}H_{6n}$ molecular complexes: a) $C_{24}H_{12}$ (coronene, n=2), b) $C_{54}H_{18}$ (coronene 19, n=3), c) $C_{96}H_{24}$ (coronene 37, n=4), d) $C_{150}H_{30}$ (coronene 61, n=5)

The validity of the results obtained by the first-principles B3LYP/32-1g model for these structures with respect to the semiempirical methods is tested by direct comparison with experimental data on the fundamental optical gap of the $C_{24}H_{12}$ island. For this purpose we follow a TD-DFT approach for the calculation of the excitation energies of this cluster. The calculated value for the fundamental optical gap is $E_{opt} = 3.18eV$, which is in a good agreement with the experimental value of $E_{opt} = 3.29eV$ measured in Ref. [96][1]. The difference between the

---

[1] We have confirmed the good TD-DFT estimation of the optical gap with respect to the experimental value also by calculating excited state energies within the Configuration Interaction Singles (CIS) Method. The optical gap given by the latter is $E_{opt} = 4.19eV$, which is by

ground state ($E_{HOMO-LUMO} = 4.13eV$) and the excited state ($E_{opt} = 3.18eV$) is also consistent with experimental measurements for similar structures, since the exciton binding energy in these complexes gives rise to a $0.5 - 1eV$ reduction of the optical gap with respect to the ground state HOMO-LUMO gap[54].

Moving on to the defected structures (with a single vacancy in the central benzene ring) an expected reduction of the gap value can be observed, while DFT basis set differences become more pronounced. For the semiempirical methods the picture changes qualitatively only in the EH2-spd case. Considering spin-degeneracy, the EH2-spd parameterization assigns the HOMO and the LUMO states to two quasi-degenerate levels prior to the real gap, which in this case is represented by the LUMO and LUMO+1. A detailed study of the corresponding eigenvectors (with respect to eigenvectors given by the DFT and EH-sp) shows that in the case of the defected structures an incorrect state is inserted at the energy axis inside the energy gap. In this sense, although the EH2-spd/EH2-sp parameterizations demonstrate overall optimal characteristics (e.g. see ref. [64] for a study on carbon nanotube band structure and the next subsection for pure clusters), a careful use might be necessary for transport calculations in defected coronene systems.

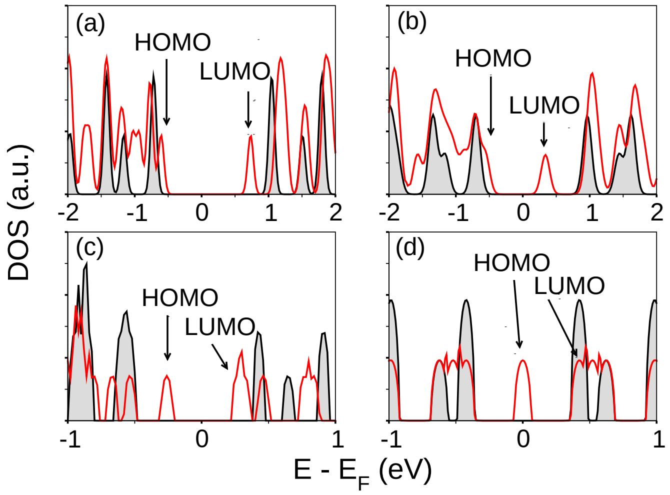

Figure 3.3: Density of states in pure/defected graphene quantum dots - Density of states around the Fermi level for pure (black line) and defected (red line) $n = 5$ islands by means of (a) DFT (STO-3G), (b) DFT (3-21g) (c) EH-sp and (d) TB. In all cases, a small smearing has been applied.

---

far bigger than the experimental and the TD-DFT value.

Another important aspect that regards energy eigenstates is their alignment over the energy axis, moreover when local alterations of the symmetry 'break' the ideal atomic structure. For few-atom molecular complexes a neat way to visualize this is with their density of states spectrum as a function of energy. Figure 3.3 plots DOS functions for pure and defected $n = 5$ islands by means of DFT, EH-sp and TB. In this case the lifting of the symmetry-induced degeneracy inserts states that tend to 'shrink' the band gap. In the case of TB, a state always appears in the center of the pure structure's gap. This well-known effect has its origin at the bipartite nature of the honeycomb lattice, where the presence of a single vacancy in one of the two sub-lattices inserts a zero energy mode at the Fermi level of the system (i.e. at energy E=0)[88]. The key issue though arising from figure 3.3 is that for the more sophisticated methods the HOMO state is not located in the center of the pure structure's gap, but shifted towards lower energies next to the valence band. Such feature is captured by both DFT and EH-sp, although in a quantitative disagreement. The analysis therefore implies that TB gives a rigid picture of the gap state with respect to more sophisticated models. Under this perspective, this study will try to affront the problem by introducing a further parameterization for the point defect (see section 3.2.3).

3.2.2.3 Qualitative evaluation: molecular orbitals

A most important aspect for transport in nanostructures is the availability of states (either full or empty) within the conduction window. In conjunction, a very important factor for the correct treatment of conduction are the eigenvectors that correspond to these states, from which topological features can be deduced (e.g. localization, polarization etc.). In this context the semiempirical methods have been evaluated on the basis of DFT results for pure, defected and hydrogen functionalized structures. Results shown here are for the DFT 3-21g, EH-sp, EH2-sp and TB models. A qualitative correspondence has been obtained for the DFT STO-3G and the EH2-spd bases with respect to their method counterparts[1].

TB: In the absence of real atomic orbitals and with the restriction of its limited basis set the TB method demonstrates a progressive wavefunction descriptive capacity from smaller to larger complexes. In particular TB eigenvectors for conduction/valence eigenstates have a poor resemblance with the respective DFT ones for the $C_{24}H_{12}$ molecule, while similarity becomes gradually better for bigger structures. This behavior is due to the C-C bonding distance polymerization features discussed earlier, which have a higher impact for the smaller complexes.

---

[1] The surprisingly accurate correspondence in terms of molecular orbitals obtained for the 3-21g and STO-3G bases within the DFT scheme indicates that the minimal basis set can be used in disordered graphene-based systems with only small quantitative compromises (see paragraph 3.2.2.2).

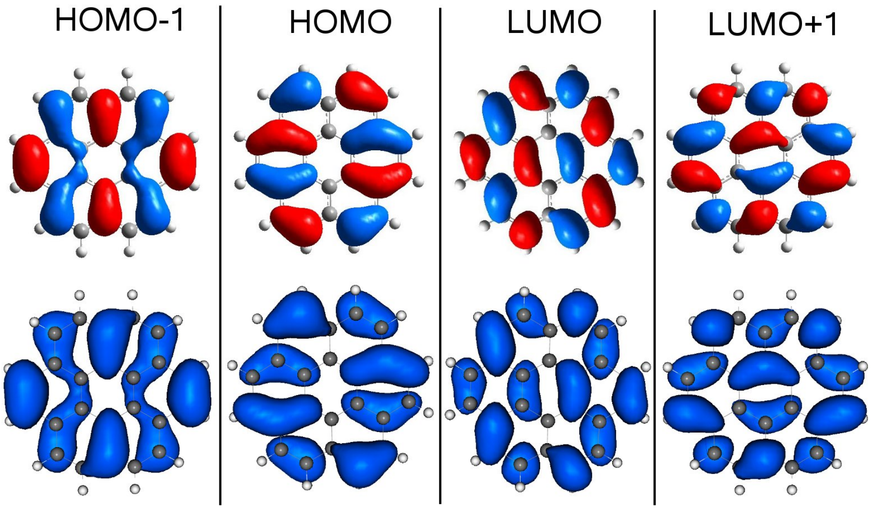

Figure 3.4: Molecular orbitals of HOMO/LUMO states in graphene quantum dots - Molecular orbitals for the HOMO-1, HOMO, LUMO and LUMO+1 states of the $n = 2$ complex by means of DFT (upper) and EH-sp (lower).

Arriving at the $n = 5$ complex, DFT-TB matching becomes adequate, hence, the TB method is qualified for the electronic structure description of these structures with a respective number of C atoms and onwards.

EH-sp: The method is in a qualitative agreement with the DFT one only for the energy degenerate HOMO/HOMO-1 and LUMO/LUMO+1 pairs for all studied structures (see fig. 3.4 for the coronene molecule). Moving away from these states towards the valence band accuracy is lost, not in the form of the wavefunctions whereas in the correct order that these appear. Conduction band description results poor.

EH2-sp: Matching between EH2-sp and DFT wavefunctions is excellent for all pure islands and for both valence and conduction energy zones (e.g. see figure 3.5 for the valence band of $C_{24}H_{12}$). It is evident here that the chemical environment in which the parameterization has taken place (bulk graphene) and the double-exponent Slater orbitals play a crucial role in the representation of correct molecular orbitals. It is also interesting to note the mismatch in the results obtained by the EH2-sp and the EH-sp parameterizations, even if the quantum chemical method is the same.

Finally, magnetism issues that could arise due to the presence of zigzag terminated edges in these complexes are not confirmed by the the *ab initio* calculations, contrary to zigzag GNRs[42, 57, 99] or coronene islands above a critical size (based on mean-field Hubbard model calculations [35]). It can be therefore stated that

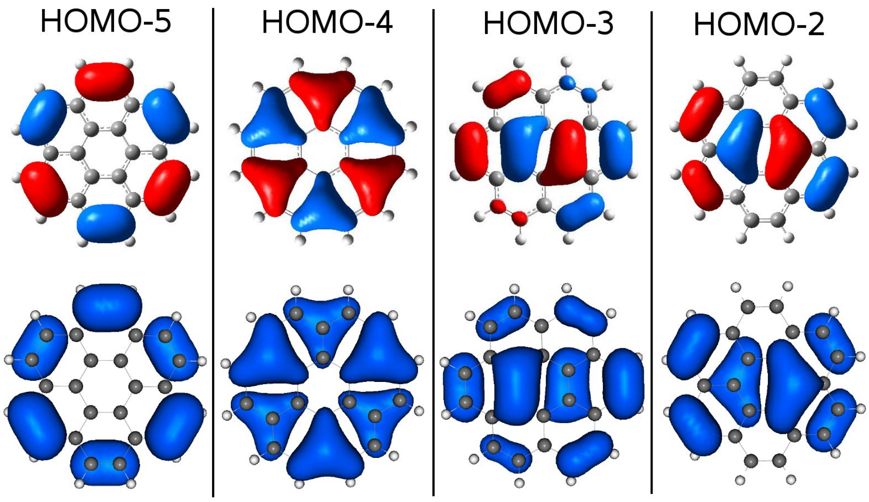

Figure 3.5: Molecular orbitals of valence band states in graphene quantum dots - Molecular orbitals for the HOMO-5, HOMO-4, HOMO-3 and HOMO-2 states of the $n = 2$ complex by means of DFT (upper) and EH2-sp (lower).

the absence of a self-consistent exchange evaluation in the semiempirical methods does not compromise the obtained results with respect to the DFT case in the present study.

The presence of a single vacancy in these islands provokes a distortion of the atomic structure since the remaining σ dangling bonds tend to recombine by leaving their equilibrium positions. On the other hand, σ-orbital energies are too far away from the HOMO-LUMO states and do not contribute to the formulation of the respective wavefunctions. Most importantly, apart from a symmetry breaking effect in topological terms, the presence of the vacancy imposes a localization of the wavefunctions that correspond to the various eigenstates, making such complexes 'sensitive' to the positioning of a nanoprobe. In terms of the various methodologies we have obtained:

TB: The lack of information concerning distance in the TB method is even more important for the defected structures, where the smaller the structure the higher is the effect of the vacancy on its deformation. In this sense the TB method with its standard parameterization is inadequate for the description of the electronic structure of these complexes, whereas like in the case of pure structures, description gradually betters as the complexes grow, with the following particularities: (i) HOMO wavevectors present a succession of zero and non-zero values for neighboring atomic sites and (ii) for even n-indexed molecules ($n = 3$, $n = 5$ etc.) the hexagonal edge that corresponds to the defected site presents atoms with zero LDOS for the HOMO eigenstate (fig. 3.6). This last observation is crucial in terms of transport modeling and its implications will be discussed in the next section.

EH-sp: It describes better the valence (HOMO, HOMO-1, HOMO-2) than the conduction band. Moreover, moving towards the bigger structures accuracy is increased and for the $n = 5$ island description becomes adequate for the valence and discrete for the conduction band.

EH2-sp: The main drawback of this parameterization has to do with the presence of an incorrect HOMO eigenstate as discussed in the previous subsection. Overall it offers a valid alternative to the DFT results, on the other hand though, the importance of the HOMO state in terms of conduction modeling requires attention in its use in defected graphene environments.

Finally a remark on the C_3 point symmetry of the HOMO wavefunction around the vacancy should be made[88] (feature that is captured by all methods), where clearly a non-zero magnetic moment arises (also obtained with Hartree-Fock-based calculations on the same complexes[41]).

Results for the complexes where the defected site has been functionalized by a hydrogen atom that saturates one σ dangling bond do not differ substantially from their nonfunctionalized counterparts. Here the role of hydrogen slightly influences the structure's geometrical relaxation whereas wavefunctions are similar to non-passivated molecules with defects, as σ-orbital energies are too far away from the zone of interest for conduction. Consequently the discussion made in the previous subsection is valid also in this case for the methods that directly account for the presence of hydrogen (DFT, EH).

3.2.2.4 Discussion

Semiempirical models in graphene-based quantum dot structures can be successfully used within a certain framework that is established by their quantum chemical limitations. The Extended Hückel method with its real-orbital foundation can cope with a great number of qualitative features, whereas the role of parameterization proves to be fundamental. In this sense EH2-spd/EH2-sp are excellent alternatives to DFT for pure coronene structures, whereas defected/functionalized complexes are more appropriately treated by the EH-sp model. On the other hand, TB with the standard parameterization can be used for the study of conduction in large defect-free systems, while modeling remains a challenge for defected complexes since results appear too 'radical'. In this sense a further parameterization of the defected site within its particular topological environment is necessary for the correct estimation of the electronic structure, argument that will be treated in the next section.

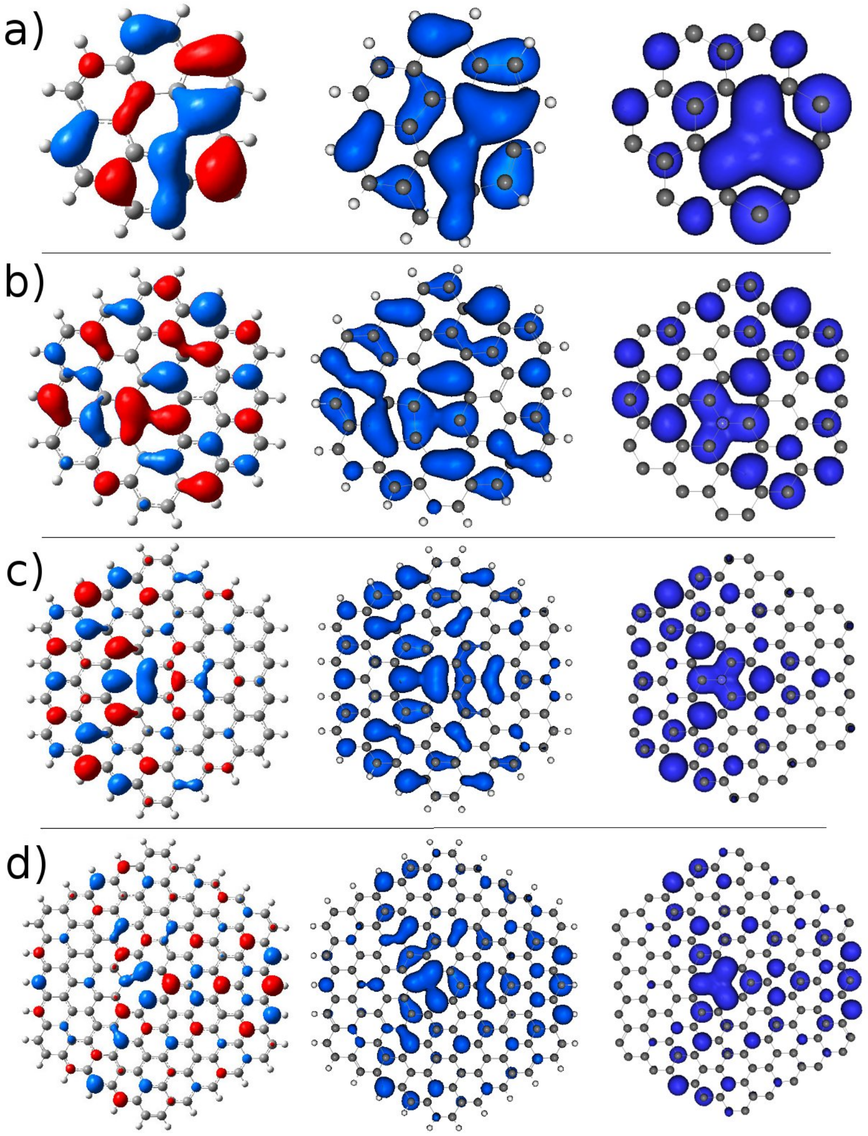

Figure 3.6: Molecular orbitals for the HOMO states for defected graphene quantum dots - Highest occupied molecular orbitals for a) n=2, b) n=3, c) n=4 and d) n=5 islands with a single vacancy by means of DFT (left), EH-sp (middle) and TB (right). The TB orbital representation is purely demonstrative by assigning Slater type p_z orbitals with the same parameters as the EH method.

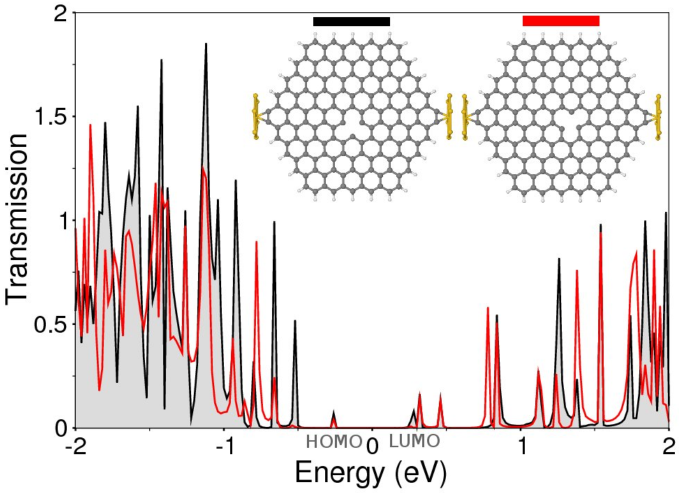

Figure 3.7: Conductance of defected graphene quantum dots by meads of EHT - Transmission as a function of energy by means of EH-sp for the defected $n = 5$ complex, for two equivalent contact configurations that differ only in the position with respect to the defected site.

3.2.3 Quantum transport

The study's bottom line is to efficiently model transport phenomena on graphene-based quantum dot systems respecting the chemical aspects that arise due to the particularity of the chemical/geometrical environment. The importance of a proper description of the electronic structure on conduction can be better appreciated in the case of defected islands, where the presence of the vacancy is a reason for topological asymmetries also on the formation of the molecular orbitals (see fig. 3.6). In this section, a numerical analysis takes place for the defected $n = 5$ complex initially with the EH-sp method, while results are used for a critical evaluation of similar calculations made with the TB model. Two equivalent molecular bridge configurations are used, where the source-device-drain geometry differs only in the position of the contacts with respect to the vacancy site (fig. 3.7). In detail, two opposite edge corners of the aforementioned dot have been inserted between two semi-infinite Au(111) metallic planes, which model the metallic probes of an atomic force microscope. The contact Hamiltonian is also written within the EH theory using an appropriate *spd* basis[28]. A prerequisite of equivalence for the contact bonding between the two configurations is explicitly requested for an evaluation of transport without geometrical or bond strength implications[28]. Here, contacts are 1.7Å distant from the edge C atoms (avoiding strong invasiveness) and are geometrically symmetrical with respect to the molecular structure. The transmission probabilities obtained for the two configurations have a distinct character, whereas differences are not fundamental for the conduction characterization of the system. Namely, both configurations give a non-zero transmission value corresponding to the HOMO state, whereas differences exist both in the valence and conduction band. The divergences can only be attributed to the different geometrical positions of the contacts with respect to vacancies that reflect unequal interface chemical bondings due to orbital localization phenomena. The minor impact of such phenomena on the conduction characteristics is driven by the real atomic orbital foundation of both contact and device wavefunctions that constitute bonding interactions that exceed next neighbor distances. Therefore, e.g. if local disorder provokes a nullification of the LDOS at the contact-device interface at a certain energy, transmission is still possible if this zero LDOS expands in a smaller area than that of orbital overlap between contact and further device atoms with a finite LDOS. The same concept can be described from a quantum mechanical perspective, where the presence of the contacts induces a constant perturbation on the bare device's Hamiltonian and the effective Hamiltonian now writes:

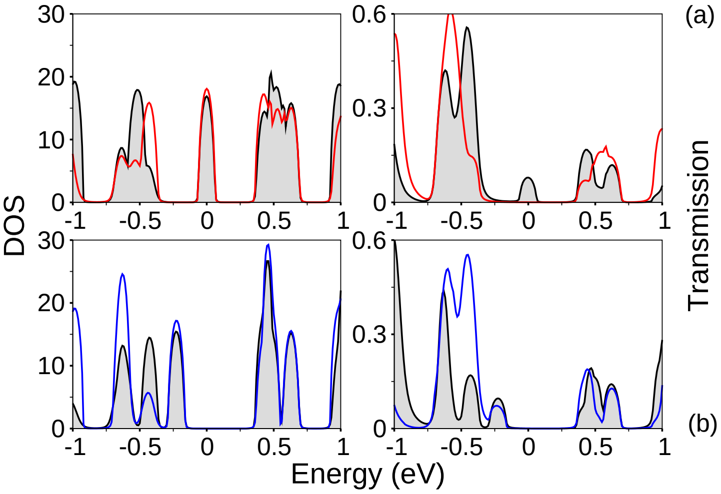

Figure 3.8: Electronic structure and transport for defected graphene quantum dots by meads of calibrated TB - Density of states and Transmission probability of the $n = 5$ complex by means of the TB method for nonparameterized (a) and parameterized (b) vacancy values ($Eon-site_{vac} = 10eV$, $t_0 = 1.9eV$). The DOS figures are represented with a small Gaussian smearing.

$$\hat{H}_{eff} = \hat{H}_0 + \hat{H}_{0L} + \hat{H}_{0R} \tag{3.2}$$

Here $\hat{H}_0$ corresponds to the molecular Hamiltonian in the absence the contacts and $\hat{H}_{0L,0R}$ are the Hamiltonian components that arise due to the interaction between the device and the left/right contact. According to EH theory for the localized HOMO state we get:

$$< \Psi_{HOMO}|\hat{H}_{0L}|\Psi_{HOMO} > \neq 0 \tag{3.3}$$

and

$$< \Psi_{HOMO}|\hat{H}_{0R}|\Psi_{HOMO} > \neq 0 \tag{3.4}$$

This finite value of both integrals makes transport plausible from the HOMO state.

Albeit its phenomenological simplicity, the TB description of conduction in the same structures as before generates complexity in the interpretation of the obtained results. The critical points are two: (i) the first has to do with the zero mode introduced by the vacancy at the Fermi energy level. The corresponding HOMO wavefunction, and equally the LDOS at $E = 0$, have a succession of finite and zero values for next-neighbor atoms, that is, for each C atom with a finite LDOS value the three nearest neighbor atoms have a zero value and *vice versa*. Moreover the $n = 5$ structure (like all even n-indexed ones) has a hexagonal side with $LDOS = 0$, as discussed in the previous section. Therefore, for the standard-parameterized first-neighbor TB model this state represents the respective molecular orbital in a rigid way, contrary to EH and DFT. (ii) The second issue reflects TB interface bonding issues between a device and the metallic leads that in the next-neighbor context present a strongly-localized character (e.g. only two C atoms in our case are allowed to chemically interact with the leads). In this case, if the metallic contacts form bonding interactions exclusively with zero LDOS carbon atoms (configuration 2 in our case), the HOMO eigenstate will not contribute to the conductivity of the system, yielding a zero transmission probability at that energy. Indeed, figure 3.8 shows transmission as a function of energy for the $n = 5$ complex for the two contact configurations presented before, where a finite transmission probability for the HOMO state appears only in the first case, whereas clearly no conduction takes place through this state for the second. In terms of expectation values, for the HOMO eigenstate of the second configuration we now get:

$$< \Psi_{HOMO}|\hat{H}_{0R}|\Psi_{HOMO} >= 0 \tag{3.5}$$

This blocked conduction channel reflects the extreme manifestation of wavefunction localization obtained by TB and comes to contrast with EH results. It is therefore fundamental that a realistic modeling has to take into account that the tails of the contact wavefunctions penetrate the body of a molecular device for several Å before they decay.

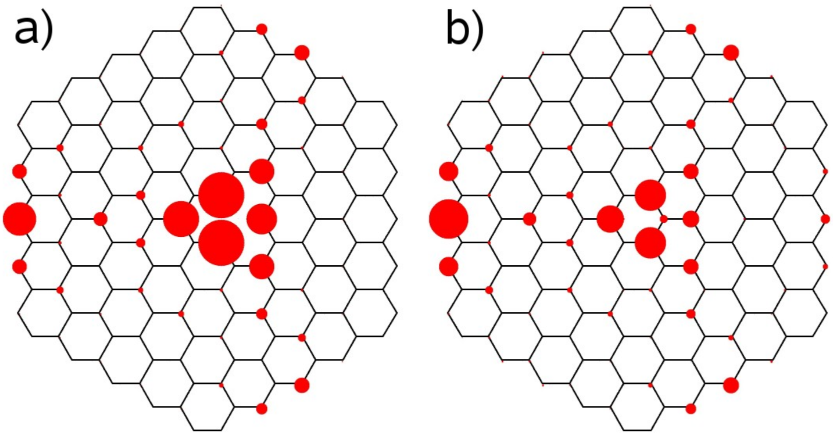

Figure 3.9: Local density of states by means of standard and calibrated TB for defected graphene quantum dots - Schematic LDOS representation of the $n = 5$ complex by means of the TB model for two different parameterizations of the vacancy site, a) $t_0 = 0eV$ within the vacancy and the neighboring sites, and b) $t_0 = 1.9eV$ and $Eon - site_{vac} = 10eV$. The radius of each circle is proportional to the amplitude of the LDOS value on that atomic site.

A possible way to affront the aforementioned problems is by introducing a further parameterization of the vacancy site. Figure 3.9 shows a schematic LDOS real-space representation of the $n = 5$ island by means of the TB method for a non-parameterized and a parameterized vacancy site. The vacancy parameterization takes place by assigning a finite $E = 10eV$ energy on the site and a $t_0 = 1.9eV$ hopping integral within this and the neighboring atoms. The principal differentiations obtained are: (i) The sites where zero LDOS values corresponded for the HOMO level now obtain a finite, albeit small density (not visible in fig. 3.9). (ii) The hexagonal edge that corresponds to the vacant site (which for even n-indexed molecules had zero HOMO-wavefunction components) obtains also a finite LDOS value that is more similar to the electronic structure by means of the DFT and the EH methods (see figure 3.6). (iii) The collocation of the HOMO eigenstate on the energy axis is in $E < 0$, i.e. it moves towards the valance band leaving the midgap position (see figure 3.8). Also in this case the DOS spectrum comes closer to the ones obtained by DFT and EH (figure 3.3). Finally, changes obtained for wavefunctions that correspond to other than the HOMO level do not present particular differences from their non parameterized counterparts. Overall, the parameterization of the vacancy site permits for a clear improvement of the qualitative aspects of the electronic structure for defected molecules, respecting the chemical equilibriums and approaching results obtained by more sophisticated methods. Indeed, in terms of transport, the HOMO eigenstate now contributes to conduction for both contact configurations whereas a less 'radical' representation of the transmission probability is sketched. Apart from to the qualitative gains of TB calibration presented here though, a key conceptual issue arises. Now the vacancy site becomes similar to a (nominally p-type) impurity, since the local point potential lowers (from ∞ to big finite) and the hopping integral raises (from $0eV$ to finite) [88]. This consideration can have an impact on the way vacancies are seen in graphene-based systems, both from an applicative as well as from a methodological point of view. As a conclusion, it should be strongly stated that the common perception of treating vacancies in graphene-based systems (zero-energy modes) is not confirmed in this study, whereas an impurity-like behavior has been obtained.

3.3 Vacancies in graphene nanoribbons

As more relevant system for microelectronics, graphene nanoribbons represent a meta for bandgap engineering and device integration of graphene-based systems. The objective here is to extensively investigate the importance of wave-function localization induced by defects for the electrical transport properties of quasi one-dimensional systems. We therefore present a systematic investigation of conduction and charging for vacancy damaged armchair and zigzag graphene nanoribbons (aGNRs and zGNRs respectively) from the physical effect of the single scatterer in the nanoscale (for ribbons with dimensions within the capabilities of modern lithographic techniques) up to a statistical analysis of finite defect concentrations (for ribbons with μm lengths). The basis of the transport formalism for the single-vacancy scatterers is based on first-principles parameterized semiempirical Hamiltonian that considers atomic interactions on the evaluation of distance-dependent overlap integrals, hence, introducing further neighbor interactions in a natural way. The parametrized tight-binding Hamiltonian of the previous paragraph is used instead for massive quantum transport calculations in heavily disordered systems. Computational results show that there is a clear relationship between the position of the vacancy, the resonance of the defect-states and the local eigenvector value of the corresponding unperturbated system. Coupling between such features can give rise to resonant backscattering phenomena during the conduction process that in the case of the first $\pi - \pi^*$ plateau are associated with the opening of pseudogaps, similar to ones obtained for p-type impurities[5]. A further goal is to evidence the charging properties of vacancies in graphene within self-consistent Schrödinger/Poisson calculations.

3.3.1 Methodology

We consider the convention of Ref. 99 to classify aGNRs (zGNRs) on the number of the dimer lines N_a (zigzag chains N_z) across the ribbon width. We use two *ab initio* parameterized semiempirical Hamiltonians with different levels of accuracy for the correct treatment of defect states in the sp^2-hybridization scheme. The first one is formed on the basis of the extended Hückel theory, using a double-ζ sp^3d^5 Slater orbital basis set[64]. Such Hamiltonian acounts for next-to-near neighbor interactions in a natural way and accurately assigns the resonance of the vacancy states. The second one is the nearest-neighbor tight-binding Hamiltonian with a $t_0 = 2.7eV$ hopping parameter, whereas on-site energies and hopping integrals for the defected sites have been appositively parameterized in order to reproduce first-principles and extended Hückel results, as seen in the previous paragraph. Energy eigenstates ϵ_α and their respective eigenfunctions Ψ_α are obtained through a direct diagonalization of the Hamiltonian matrix imposing periodic boundary conditions in large supercells. Quantum transport is studied within the non-equilibrium Green's function formalism (NEGF) coupled to the Landauer-Buttiker approach for the calculation of the conductance g[24]. Simulations take place within the ballistic regime. Contacts are ideal, i.e. of the same width N_a (N_z) as the device without the presence of vacancies. Edges are passivated with single hydrogens.

3.3.2 Vacancies in aGNRs

We start this study with electronic structure, conductance and density of states (DOS) spectra calculated for a semimetallic 38-aGNR. Here the vacancy is introduced in various positions of a chain transversal to the longitudinal axis of the system (see fig. 3.10a). Electronic structure calculations show that the universal response of the defect is to give rise to quasilocalized states[88] along nonlocalized ones, that due to electron-hole disparity do not preserve a mirror symmetry with respect to the charge neutrality point. The level of localization for these states can vary from strong to weak while their energy resonance highly depends on the position of the defect site. When it comes to conduction, there are two distinct groups of behaviors obtained on the basis of the location of the vacancy sites. For sites of the first group, significant conductance dips and pseudogap features are present within the valence band of the first $\pi - \pi^*$ plateau of the system. The correspondent DOS interestingly shows a smooth bell-like region which expands throughout the conductance dip zone. The presence of a non-negligible DOS where a conduction gap takes place is strongly correlated with resonant backscattering phenomena during the transport process. Such feature is strikingly similar to analogous effects calculated for p-type (nominally boron)

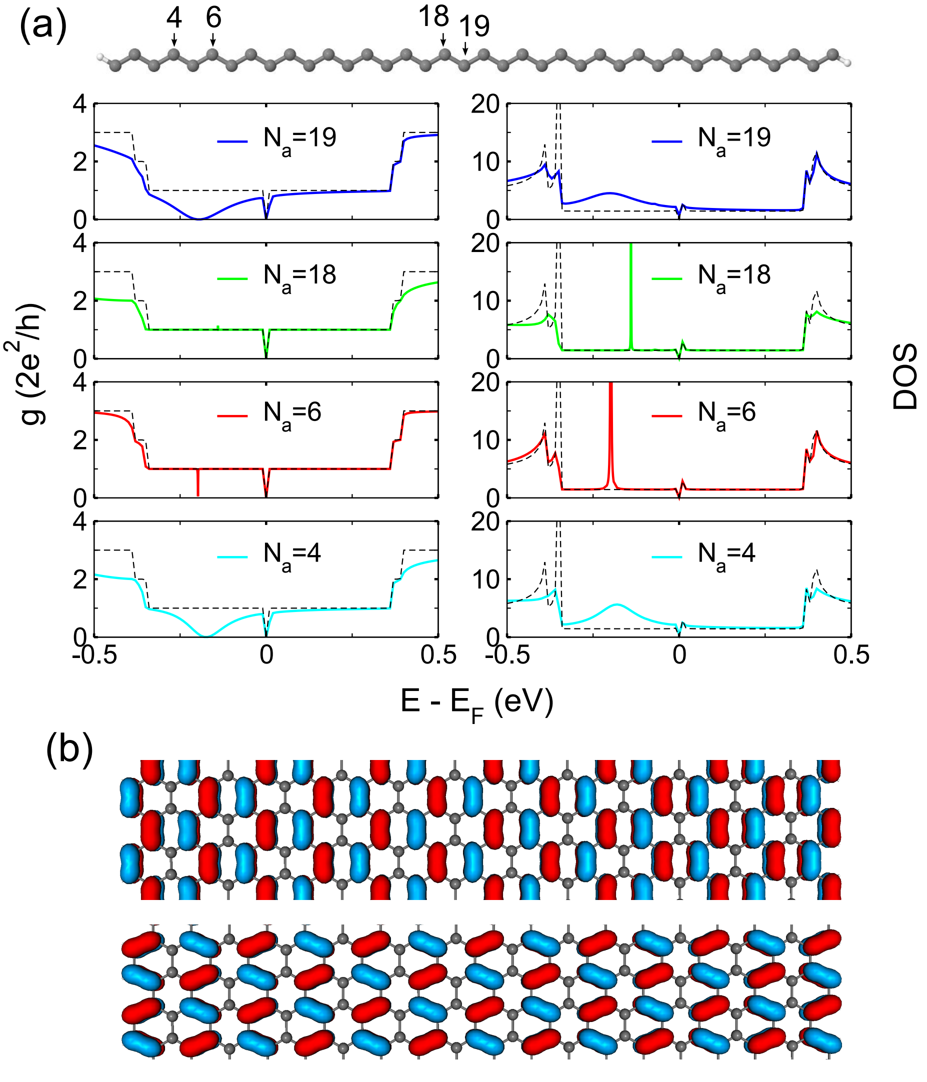

Figure 3.10: Conductance and DOS for a defected 38-aGNR - (a) Conductance g and DOS as a function of energy for a 38-aGNR with single vacancies at different positions N_a. (b) Projection of the wavefunction corresponding to first state below the charge neutrality level (upper) and the first state above the charge neutrality level (lower) for a non-defected 38-aGNR.

impurities[5]. On the other hand, second group sites practically leave the pure structure's $g = 1$ (in units of $2e^2/h$) conductance plateau unaltered. Here the first vacancy state below the charge neutrality point gives rise to a DOS with a sharp peak that decays exponentially and provokes a strongly localized perturbation in the electronic structure. A systematic analysis for the sum of possible vacant sites shows that two thirds of the total sites belong to the first group, while the remaining one third sites conform with the second group. This categorization strictly stands only for the first $\pi - \pi^*$ region, since for energies that are more distant from the charge neutrality point, further divergences occur in the conduction properties according to purely geometrical criteria.

The $1/3 - 2/3$ relationship presented above can be understood with a careful examination of the ribbon's wavefunctions in the ideal case, i.e. when no alteration of the atomic structure is present (see fig. 3.10b). The form of the eigenvectors within the the entire first conductance plateau preserves a $1/3-2/3$ schema where $2/3$ of the sites have a finite eigenvector value while the rest $1/3$ have an extremely small value instead. If the vacancy is introduced in a position corresponding to the $2/3$ group, eigenvector symmetry breaks and defect-mode perturbations spread also to neighboring energies. The sum of perturbative behaviors due to the quasilocalized states within this plateau gives rise to an increased DOS distribution with respect to the ideal case below the charge neutrality point. This expanded perturbation is the reason for electron backscattering during conduction. On the other hand, if the vacancy is introduced in the $1/3$ group sites, the perturbation induced remains localized since the $2/3$ symmetry does not break, and no generalized repercussions are inferred in the conductive capacity of the system. This concept can be visualized better through local density of states distributions $\mathrm{LDOS}(\vec{r}, E)$ at the positions $\vec{r}$ of the device atoms. In the case of a system with semi-infinite contacts the LDOS can be calculated within the NEGF[30]. Figures 3.11(a),(b),(c) show LDOS values for different energies within the first plateau for a 38-aGNR with a vacancy at $N_a = 19$. It is clear that a perturbation around the vacancy site spreads over the entire range of energies that corresponds to the conductance dip. Contrary, for $N_a = 18$ no extended perturbation can be detected (see 3.12d) apart from the highly localized energetic position of the quasilocalized vacancy mode.

This picture is not only present in the previous aGNR but reflects a general situation for the conduction properties of vacancies in semimetallic nanoribbons with the armchair confinement (e.g. see fig. 3.12a). A systematic data analysis for aGNRs up to $N_a = 44$ dimer lines leads to the following empirical rule (which is supported by analytical calculations of the first plateau wavefunctions for all metallic aGNRs[120]): for $N_a = 3p + 2$ dimer lines ($\forall p \in \mathbb{N}$), vacancies at the $N_a = 3q$ sites belong to the $1/3$ group ($\forall q \in \mathbb{N}, \leq p$), while the rest make part of the second group. Apart from the semimetallic ribbons, semiconducting aG-

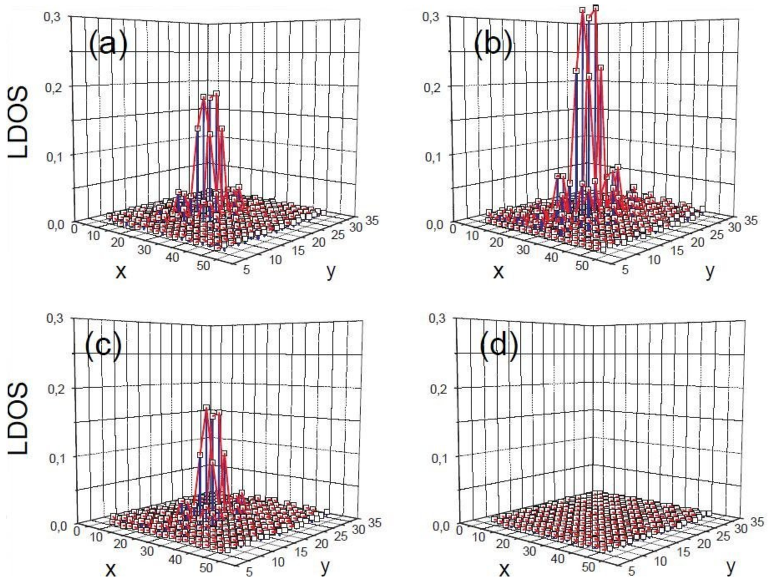

Figure 3.11: Local density of states for a defected 38-aGNR - LDOS as a function of distance coordinates (in Å) and energy (in eV) for a defected 38-aGNR. Defect position N_a and energy E are at (a) $N_a = 19, E = 0.27eV$, (b) $N_a = 19, E = 0.17eV$, (c) $N_a = 19, E = 0.07eV$, and (d) $N_a = 18, E = 0.17eV$. The zero energy level refers to the charge neutrality point.

NRs behave within a similar framework that infers a less pronounced effect on the transport mechanism due to the intrinsic electronic bandgap (see fig. 3.12b). Unlike though their semimetallic counterparts, wavefunctions of semiconducting aGNRs do not globally preserve the $1/3 - 2/3$ symmetry within the first conductance plateau (fig. 3.12c). Notwithstanding this, the mechanism that gives rise to DOS perturbations and therefore to conductance dips remains the same, even if mainly for vacancies towards the center of the ribbons backscattering effects are always present and differences are attenuated.

3.3.3 Vacancies in zGNRs

The case of defected zGNRs is intrinsically more complicated than that of aGNRs due to the presence of edge magnetism (that gives rise to a secondary bandgap[99]) in conjunction with the local spin attributes of vacancies themselves[85]. On the other hand recent *ab initio* calculations have shown that the most stable hydrogen-terminated zig-zag ribbons are not monohydrogenated and loose their magnetic ground state[113]. Here we neglect spin interactions and focus on the effect of vacancy-induced pseudogaps within the conduction process, which is complementary to but of a higher order with respect to the intrinsic bandgap

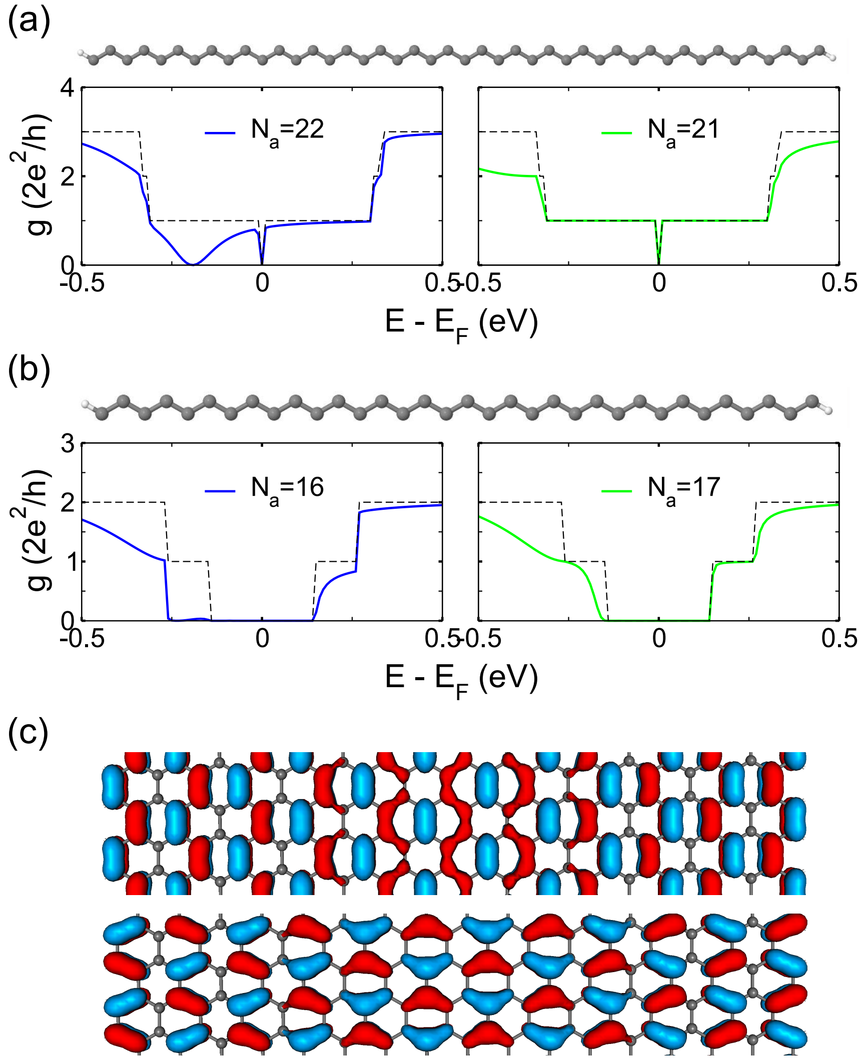

Figure 3.12: Conductance of defected armchair graphene nanoribbons - a) Conductance g as a function of energy for a semimetallic 44aGNR with a single vacancy at $N_a = 22$ (left) and $N_a = 21$ (right). a) Conductance distribution g as a function of energy for a semiconducting 34aGNR with a single vacancy at $N_a = 16$ (left) and $N_a = 17$ (right). (c) Projection of the wavefunction corresponding to first state below the charge neutrality level (upper) and the first state above the charge neutrality level (lower) for a non-defected 34-aGNR.

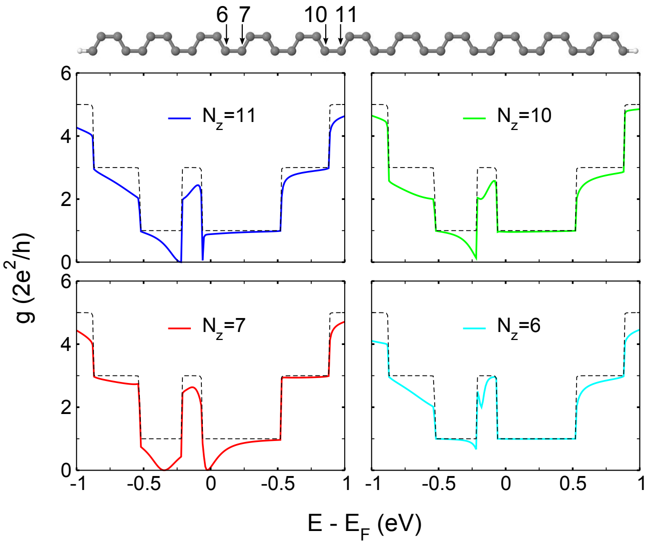

Figure 3.13: Conductance of a defected 22 zigzag graphene nanoribbon - (a) Conductance g as a function of energy for a 22-zGNR with a single vacancy at the $N_z = 11$ (up-left), $N_z = 10$ (up-right), $N_z = 7$ (down-left) and $N_z = 6$ (down-right) positions. (b) Bandstructure of an ideal 22-zGNR with periodicity L within the spin-restricted extended Hückel model.

(see Ref. 82 for a discussion on spin-polarized transport). Fig. 3.13 shows representative conductance results for a 22-zGNR with single vacancies at four different internal positions of the ribbon along a chain transversal to the longitudinal axis of the system. The $1/3 - 2/3$ symmetry seen in the case of aGNRs is not confirmed, reflecting the different form of zGNR wavefunctions. On the other hand symmetry effects with respect to parity, as well as important differences with respect to the positioning of the various defected sites can be obtained. In detail, vacancies at the central region of the zGNR show a p-type conduction gap that is greatly compromised by the presence of the $g = 3$ plateau area due to band-bending close to the Fermi level near the Brillouin zone boundaries (see Fig. 1.5). Moving towards the ribbon's edges, even-N_z sites become completely metallic whereas odd-N_z sites give rise to a simultaneous transport gap in both conduction and valence bands[46]. This behavior is similar to impurity backscattering with both donor and acceptor characteristics, whereas analogous effects have been calculated for substitutional boron atoms[5]. The key issue for understanding resonant backscattering phenomena in zGNRs can be traced back in the high local density of states concentration within the $\pi - \pi^*$ plateau that is not only limited to edge states, i.e. nonlocalized states in an ideal zGNR are present in this energy zone. The wavefunctions of these states usually maintain a parity symmetry for neighboring sites that can loose balance while moving from the center towards the edges of the ribbon. According to the exact positioning of the vacancy site the perturbation induced can be stronger or weaker while it can affect more than one regions at the entire plateau, giving rise to separate resonant backscattering phenomena during the conduction process.

3.3.4 Vacancies as charging centers

For a more realistic description of quantum transport and the evaluation of nonequilibrium aspects of conduction, we have performed self-consistent simulations within the coupled NEGF-Poisson scheme in order to evidence the manifestation of charging effects related to the presence of vacancies in the atomic lattice. To this purpose, we have extended the open-source *NanoTCAD ViDES* code[36, 39] with extended-Hückel functionality and enhanced matrix operations with optimized numerical techniques[90]. We consider the 4-terminal geometry of fig. 3.14a and 20/22aGNRs with length $l = 8.41nm$ as channel materials. Single vacancies are introduced at various positions of the atomic lattice, whereas the relatively short length of these aGNRs allows for a short-range Coulomb scattering study within the ballistic limit. Simulation temperatures are set to $T = 300K$. Gate voltages are fixed to zero ($V_{G_1S} = 0V, V_{G_2S} = 0V$) while drain-to-source bias is gradually raised from $V_{DS} = 0V$ to $V_{DS} = 0.5V$. Maps of the electrostatic potential Φ along the ribbon surfaces at the end of the self-consistent process can be seen at fig. 3.14b. There are two main charging aspects related to the presence of vacancies in these samples: on one hand the immediate region around the defect acquires a charge concentration that manifests as an electrostatic peak on the GNR topology. This feature appears for all types of vacancies discussed in the previous paragraphs. Directionality of such potential is also visible in correspondence to the geometrical orientation of the vacancy. On the other hand though, an important aspect arises in the cases where vacancies are associated with impurity-like backscattering issues. Here the presence of the defect gives rise to a charge-carrier inhomogeneity effect on the GNR topology (e.g. see the lower panel of fig. 3.14b). Moreover, this process is bias-dependent, i.e. by increasing V_{DS} a more intense electrostatic inhomogeneity pattern can be observed. The presence of carrier inhomogeneities on the graphene surface have been widely attributed to charged impurities, and under this perspective important experimental features related to the measured conductivity of graphene have been justified[18]. This study indicates that alternatively, also vacancies can create similar charging disorder whose extend should ideally be calculated for flakes of dimensions within the range of the microscale.

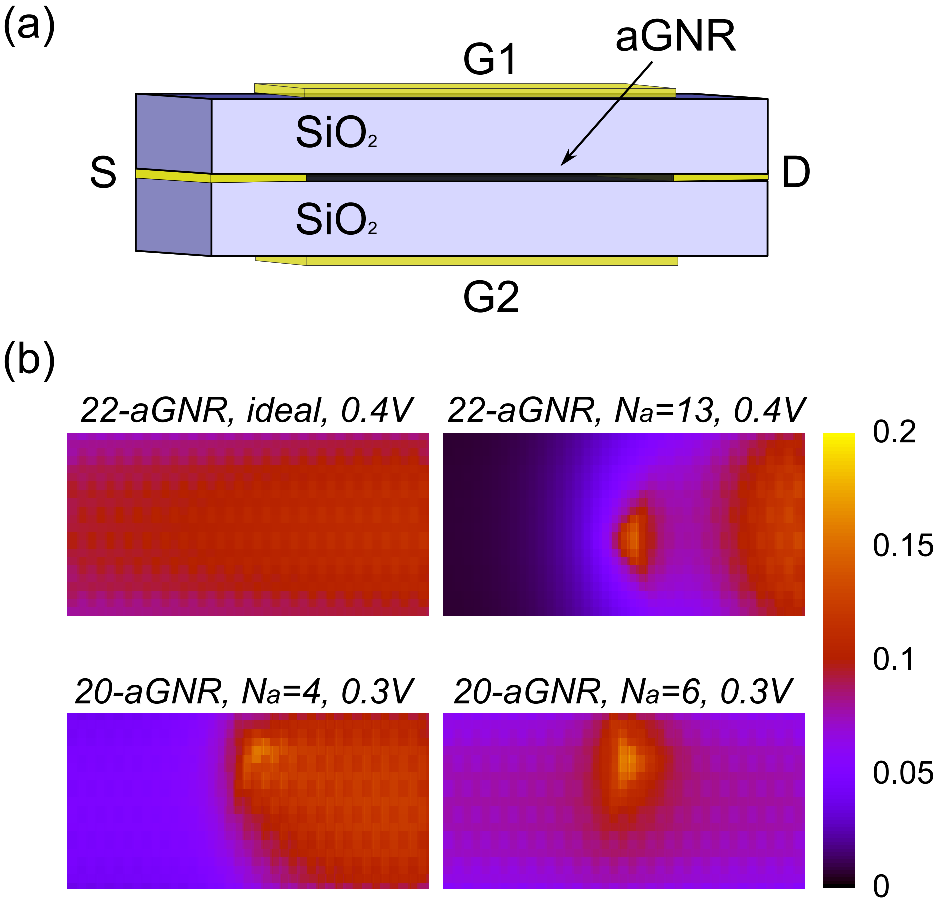

Figure 3.14: Charging effects in defected graphene nanoribbons - (a) Schematic representation of the simulated 4-terminal system. Front and back gates are isolated by a 1.9 nm thick SiO_2 layer with a relative dielectric constant $\kappa = 3.9$. Armchair graphene nanoribbons are used as channel materials with length $l = 8.41nm$. (b) Maps of the electrostatic potential Φ (in V) along the ribbon surface for an ideal 22-aGNR ($V_{DS} = 0.4V$), a 22-aGNR with a single vacancy at $N_a = 13, l = 4.38nm$ ($V_{DS} = 0.4V$), a 20-aGNR with a single vacancy at $N_a = 4, l = 4.28nm$ ($V_{DS} = 0.3V$) and a 20-aGNR with a single vacancy at $N_a = 6, l = 4.28nm$ ($V_{DS} = 0.3V$).

3.3.5 Statistical conductance analysis for finite defect distributions

Understanding of single-vacancy scattering forms the basis of the generalized backscattering mechanism present in confined graphene systems. However transport repercussions for realistic devices within the micro-scale and a finite concentration of defects can only be addressed within statistical analyses of large replicas of equivalent systems. For this purpose we have appositively calibrated a next-neighbor TB Hamiltonian that reproduces results obtained by more accurate Hamiltonians in the case of single vacancies(see paragraph 3.2.3). Figure 3.15 shows statistical averages for the conductance of a 0.84μm long 47 AGNR with two finite defect concentrations (0.2% and 0.4% respectively), obtained for more than 500 equivalent replicas of these systems. Like in the single vacancy case, a mobility gap appears in the hole-band region close to the Fermi level of the system. We have evaluated if the studied systems are in the localization regime or the quasi-diffusive one for different energies within and far from the quasigap: in the first case the average zero temperature resistance $< r(E) >=< g(E) >^{-1}$ dependes exponentially on L:

$$\langle lnr(E)\rangle = 2L/\xi(E) + c, \tag{3.6}$$

where c is a small constant that does not depend on E and $\xi(E)$ is the energy dependent localization length. In the second case the mean free path l_e can be calculated as:

$$r = r_c(1 + L/l_e), \tag{3.7}$$

where r_c is the contact resistance. By means of a scaling analysis[23, 66] we found that the conduction regime varies with the energy of the charge carriers, passing from the localization regime (the localization length ξ is $\sim 40nm$ in the center of the conduction gap for the 0.2% case) to the quasi-diffusive one away from the conduction gap (the elastic mean free path l_e is $\sim 0.4\mu$m when $E \sim 1eV$ for the 0.2% case). However, the main issue arising from multiple scatterers is the significant downgrading of the conductance throughout the energy spectrum that increases with the defect concentration. It is also evident that for heavily damaged GNRs (defect concentrations of 0.4% here) conductance becomes extremely low and typical graphene-like properties practically vanish. Crystalline quality is therefore a fundamental prerequisite for the maintenance of device-related characteristics like high electron mobilities and current densities.

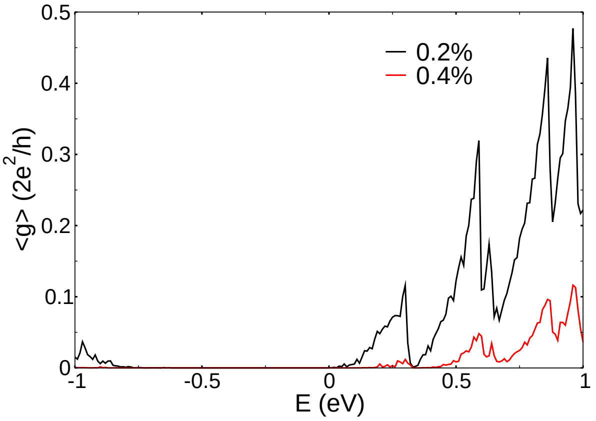

Figure 3.15: Average conductance distribution for a 47aGNR with a finite defect concentration - Average conductance $< g >$ as a function of the energy E, for a vacancy damaged 47 aGNR. Plotted values represent statistical averages over more of 500 equivalent replicas of the system. Charge neutrality points of pure and defected systems are aligned at E=0 in the figure.

3.4 Conclusions and discussion

One important aspect of the understanding of impurity induced disorder in graphene is the possibility of a controllable band gap tailoring for semiconductor applications [6, 67]. This study evidences that vacancies in graphene complexes actually behave as impurities. Such consideration can have a big practical impact on the engineering of mobility gaps in graphene-based systems since vacancies are easier to obtain (e.g. by ion irradiation [22]) than actual p or n-type doping. Here we have attempted to affront modeling issues, starting from pure and defected graphene quantum dots and keeping in mind that the desired computational efficiency for the simulation of large systems should not be in contrast with chemical accuracy. In this sense a multiscale approach has been introduced with the scope to identify merits and limitations of semiempirical approaches within a designated chemical environment prior to their use for the calculation of quantum transport. Model confrontations have demonstrated that no perfect matching exists between the results obtained by the *ab initio* on the one hand and the semiempirical approaches on the other. The extended Hückel method with its real-orbital foundation manages to capture a wide set of qualitative aspects of the systems, which qualify it as an appropriate method for quantum transport calculations in graphene-based environments. Moving towards computational efficiency, the tight-binding model has confirmed its authoritativeness for pure large-scale structures, whereas when structural defects have to be accounted a further parameterization of these sites needs to be considered. Unlikely, such tuning cannot be generic for all types of complexes/defect-types since chemical environment influence can be fundamental. E.g. we have to note that by only adding a second vacancy in the immediate vicinity of the same triangular sublattice of the honeycomb structure, hybridization between the two modes can take place. In this sense, a model evaluation of TB by a more sophisticated method should ideally take place prior to its use in disordered graphene-based systems. It should be pointed out that both theoretical and experimental attention should be paid to strongly defected systems where topological disorder can be a reason for wavefunction localizations, whose influence on the electronic properties can be important.

We have moreover extensively investigated conduction and charging properties of armchair and zigzag graphene nanoribbons with vacancy scatterers. Focus has been put on the underlying backscattering mechanism that proves fundamental for transport-related features like the appearance of pseudogaps within the first conductance plateau. A front-end consequence arising from this mechanism is that vacancies can behave as *p*-type impurities, while additional donor-like behaviors can be observed in the case of zGNRs. It has been argued that the positioning of the defect-states within the eigenspectrum in conjunction with geometrical considerations that shape the system wavefunctions are the origin of the presented phenomena. Moreover self-consistent quantum transport calculations have evidenced that during nonequilibrium, vacancies can induce inhomogeneities in the electrostatic topology of the ribbons, in accordance with similar effects often attributed to the presence of charged impurities. On the basis of such assumptions some key points need to be discussed. From an application point of view the association of vacancies with conduction gaps can have a big practical impact on the engineering of mobility gaps in graphene-based systems, since vacancies are either present in the atomic lattice from the production stage or can be easily obtained e.g. by ion irradiation. Vacancy-concentration has to remain low though in order to avoid predominant inelastic electron-phonon scattering processes and consequently high reductions of the electron mobility[19]. A preferential experimental verification is necessary here. From a methodological point of view an important issue arises with respect to the resonance of the defect states. An inaccurate positioning of these modes in the first conductance plateau can lead to a dislocation of the pseudo-gap resonance, or in some cases, to a complete suppression of such effect. In this sense, second or higher neighbor atomistic models, or impurity-like calibrations of the vacancy site[67] seem more appropriate for quantum transport calculations in defected graphene systems.

Chapter 4

Contact-graphene interaction

4.1 Introduction

Integration of graphene-based nanostructures in electronics, sensors and environmental applications makes necessary a clear understanding of the interaction between graphene and metallic surfaces[69, 72, 73, 79]. Interface bonding and electrostatics can play a crucial role in the transport characteristics of these systems since the low-dimensionality and high carrier mobility of the channel material[44] can enhance the role of the metallic contact with respect to the traditional complementary metal-oxide semiconductor technology. In this sense it can be argued that the main source of resistivity in graphene-based devices should derive from the interaction with the metallic electrodes. Characteristics of such interaction for two-dimensional graphene have been identified both experimentally[8, 69, 79] and theoretically[3, 63], where charge transfer, doping-related phenomena and near-interface potential fluctuations have been reported. However, as patterning and lithographic techniques advance towards one-dimensional (1D) confinement in order to engineer the necessary bandgaps for digital applications, a particular 1D electrostatic response can be expected that should strongly differentiate device characteristics with respect to the two-dimensional case[70]. In this chapter we investigate the role of the mettalic electrodes on the transport properties of graphene nanoribbons within a double perspective: on one hand we establish the fundamental electronic, conduction and electrostatic properties of a metal-GNR heterojunction within the atomistic self-consistent Schödinger/Poisson scheme. Attention is paid on both the chemical aspects of the interface bonding as well the one-dimensional electrostatics along the ribbon length, in order to evaluate the role of band-bending and doping effects on the transport properties of these systems. In the second part of the chapter we consider an ideal molecular device based on GNR channels embedded within metallic contacts and focus on the nonequilibrium aspects of the conduction process toward the high bias regime.

4.2 Metal-graphene heterojunctions

We start this chapter by studying the tansport properties metal-graphene nanoribbon (GNR) heterostructures within self-consistent quantum transport simulations on the basis of: a) an atomistic description on both the active device part and the metallic electrode that respects the interface chemical bonding, b) a proper treatment of the junction electrostatics and c) depletion region length-scales. The objective of the computational formalism is to evaluate both the charge transfer phenomena that are present in heterojunctions due to work-function differences (e.g. band-bending and doping), as well as investigate the electrode-dependent scattering processes that can block conduction channels in particular cases. Moreover a critical analysis between metal-GNR and metal-carbon nanotube (CNT) properties takes place in order to point out some common aspects that could allow for a plausible transfer of metal-CNT know-how in GNR-based devices.

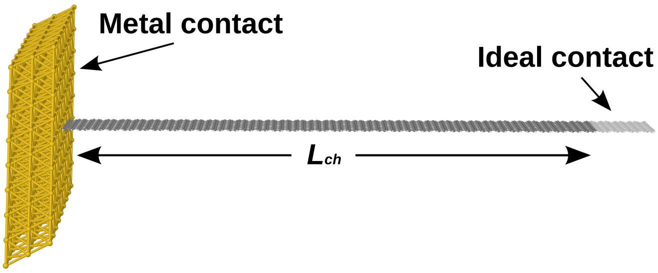

Figure 4.1: Configuration of metal-graphene nanoribbon heterojunctions - Configuration scheme of the simulated graphene nanoribbon systems, where a GNR is end-contacted by a three-dimensional semi-infinite metallic electrode at the left side, whereas ideally contacted at the right side.

4.2.1 Methodology

We consider hydrogen-terminated armchair and zigzag graphene nanoribbons (aGNRs and zGNRs respectively) and use the terminology of Ref. 99 to categorize them on the basis of the dimer lines N_a (zigzag chains N_z) along the ribbon width. Fig. 4.1 shows the two-terminal geometry used throughout this study, where GNRs with channel lengths $L_{ch} \approx 17nm$ are end-contacted at the left side by the (111) surfaces of three-dimensional semi-infinite electrodes (Au, Pd, Pt and Al). The right electrode is an ideal ohmic contact[39], i.e. a GNR with the same dimer lines (zigzag chains) as the device part. In the case of semiconducting aGNRs this geometry corresponds to a Schottky junction. We employ a self-consistent Schrödinger/Poisson scheme for the calculation of transport and electrostatics. Quantum transport is computed within the non equilibrium Green's function formalism (NEGF) coupled to the standard Landauer-Buttiker approach[24]: the single particle retarded Green's function matrix reads $\mathcal{G} = [ES - H - \Sigma_L - \Sigma_R]^{-1}$, where E is the energy, H (S) is the device Hamiltonian (overlap) matrix and $\Sigma_{L,R}$ are self-energies that account for the effect of scattering by the contacts ($\Sigma = \tau g_s \tau^\dagger$, where g_s is the surface Green function specific to the contact type and τ is the Hamiltonian relative to the interaction between the device and the contact). From the total transmission probability $T = Trace[\Gamma_L \mathcal{G} \Gamma_R \mathcal{G}^\dagger]$, where $\Gamma_{L,R} = i[\Sigma_{L,R} - \Sigma_{L,R}^\dagger]$, conductance can be calculated as $G = (2e^2/h)T$. The device spectral function is the anti-hermitian part of the Green matrix $A = i(\mathcal{G} - \mathcal{G}^\dagger)$, from which the local density of states (LDOS) at energy E and position $\mathbf{r}_\alpha$ can be defined as: $LDOS(\mathbf{r}_\alpha, E) = \int_{\mathbf{R^3}} Trace[AS/(2\pi)]\delta(\mathbf{r} - \mathbf{r}_\alpha)d\mathbf{r}$, where δ is the Delta function and $\mathbf{r}_\alpha$ shows the positions of the atomic sites. Hamiltonian and overlap matrices are written within a first-principles-based parameterized model using the extended Hückel theory[15, 64] and a non-orthogonal double-ζ Slater-type basis that fits the bandstructure of bulk graphene[64] and fcc metals[15] from density functional theory calculations. Metal surface Green functions for the evaluation of the respective self-energies are calculated for the three-dimensional semi-infinite contact with a back-and-forth real to k-space Fourier transform exploiting lattice periodicity[117]. Charging effects are introduced in the formalism with the inclusion of a self-consistent potential $U_{sc}(\rho_f)$ that is a functional of the device density matrix and is added to the bare device Hamiltonian (i.e. $H = H_0 + U_{sc}(\rho_f)$). Within the self-consistent procedure, mobile charges ρ_f deriving from the NEGF are passed to a three-dimensional numerical Poisson solver $\nabla^2 U_{sc} = -\rho_f/\epsilon$, considering the device part embedded in SiO_2[39]. A Dirichlet boundary condition is set in the metal-GNR interface of the Poisson box with a value $U_{sc}^{left} = \phi_m - \phi_{gr}$, where ϕ_m, ϕ_{gr} are the experimentally measured work functions for (111) metallic surfaces and graphene[1]. Null Neumann boundary conditions are set for the other five faces of the Poisson simulation box. Self-consistency is enhanced by a predictor/corrector Newton-Rapson algorithm[107] while optimized matrix manipulation techniques[90] have been implemented throughout the numerical code. Fermi-Dirac statistics are introduced for room temperatures ($300K$).

4.2.2 Band alignment

Fig. 4.2 shows a real-space representation of the band formation along the ribbon lengths within total/local density of states spectra for a semiconducting N_a=16 aGNR and a semimetallic N_a=14 aGNR. In the case of the 16 aGNR contacted with the high work function Au electrode (Fig. 4.2(a)) the equilibrium Fermi level

---

[1] $\phi_{Au_{(111)}} = 5.31eV$[77], $\phi_{Pd_{(111)}} = 5.6eV$[77], $\phi_{Pt_{(111)}} = 5.7eV$[77], $\phi_{Al_{(111)}} = 4.24eV$[77] and $\phi_{gr} = 4.6eV$[84]

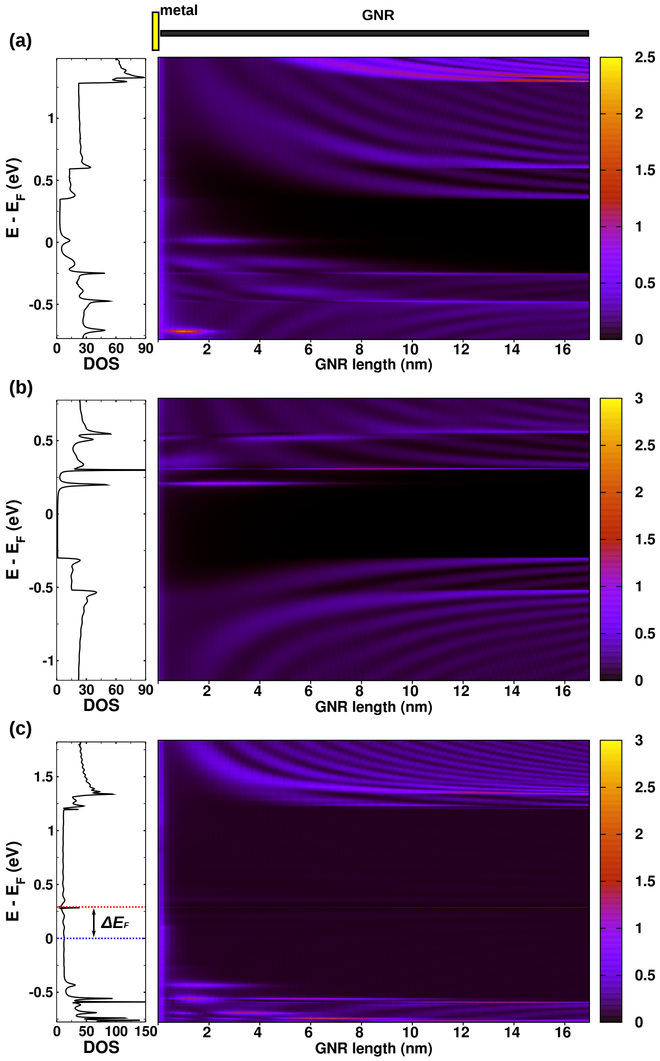

Figure 4.2: Real-space bands for metal-GNR heterojunctions - Total (left) and Local Density of States spectra along the GNR length (right) for (a) a semiconducting N_a=16 aGNR contacted with Au, (b) a semiconducting N_a=16 aGNR contacted with Al and (c) a semimetallic N_a=14 aGNR contacted with Pt. ΔE_F in (c) denotes the difference between the Fermi levels of the metal-contacted and the respective ideal aGNR.

alignment for the two parts of the heterostructure gives rise to significant upwards band-bending phenomena near the metal-aGNR interface due to the higher work function of the metal with respect to the GNR. However, band-bending is not rigid for both conduction and valence bands as a result of a complex interference mechanism: the LDOS distribution clearly shows the presence of wavelike quantum interference patterns due to the reflection of the incident electron wave by the non-ideal contact[47]. Near the interface such patterns tend to turn upwards for the conduction band and downwards for the valence band and respond differently in the presence of the electric field induced by the barrier. Hence, conduction band shifts smoothly while valence band shows localization patterns in the LDOS distribution. Such patterns become discrete localized states with a few-nm spatial breadth in the energy region where the bended valence band is triangularly-like confined inside the bandgap. In addition, metal-induced gap states (MIGS), i.e. tails of the metallic wavefunctions decaying very fast in the semiconducting gap, form throughout the interface (visible as a brighter left-border line for all energies in the LDOS representation of Fig. 4.2(a)). It can be therefore argued that the interface between a GNR and a metallic contact is ruled by complex band-bending, interference and localization phenomena whose influence in the conduction mechanism will be discussed in the following. When the same aGNR is contacted by a low-work function *Al* electrode (Fig. 4.2(b)) the bands bend downwards ($\phi_{Al} - \phi_{GNR} < 0$ here), whereas qualitatively similar behaviors as before (interference patterns, localized gap states, MIGS) can be observed. In both cases the Fermi level remains within the bandgap although loosing the midgap position of the respective ideal aGNR. In the case of a semimetallic 14 aGNR contacted with *Pt* (Fig. 4.2(c)) the main issue arising from the interaction between the two structures is a p-type doping effect due to the presence of the high work function metal (see ΔE_F in Fig. 4.2(c) for the difference between the Fermi levels of the metal-contacted and the respective ideal aGNR). Hole carrier injection has been obtained for all high work function metals on metallic GNRs in this study while a less pronounced electron doping effect has been observed in the case of *Al*. Band-bending is also evident here from the first $\pi - \pi^*$ bands and onwards, however the presence of the electrostatic potential does not seem to affect the states that lie inside the first $\pi - \pi^*$ plateau (e.g. see the GNR-long flat line that corresponds to the secondary meV bandgap of the 14 aGNR at the ideal structure's Fermi level in Fig. 4.2(c)).

4.2.3 Heterojunction electrostatics

Characteristic 1D junction electrostatics are present in the metal-aGNR case. Fig. 4.3 shows potential profiles along ribbon lengths for the previously shown N_a=14 and 16 aGNRs contacted by all available metals in this study. The main aspect of the electrostatic potential for the semimetallic aGNR is a steep potential drop near the contact interface that decays after few *nm* to a non-zero flat value. This finite potential value denotes the presence of carrier accumulation throughout the GNR length (holes for *Au*, *Pd* and *Pt* and electrons for *Al*). In the case of the semiconducting 16 aGNR the Schottky junction behaves qualitatively different. Screening is smoother and charges tend to vanish away from the metal contact. However, also in this case long-range depletion tails in the charge distribution have been obtained, in accordance with previous studies on CNT junctions[70]. In this sense an accurate estimation of depletion length scales becomes difficult in these systems and "breaks" the traditional metal-semiconductor scheme, giving rise to novel 1D device design possibilities. The categorization of metal-GNR electrostatics on the basis of the conductive character of the respective GNR has been also encountered in the metal-CNT case[29]. It can be argued that as the width of semiconducting GNRs grows and the respective bandgaps decrease[99] we can expect an electrostatic response that smoothly shifts from Fig. 4.3(b) to Fig. 4.3(a).

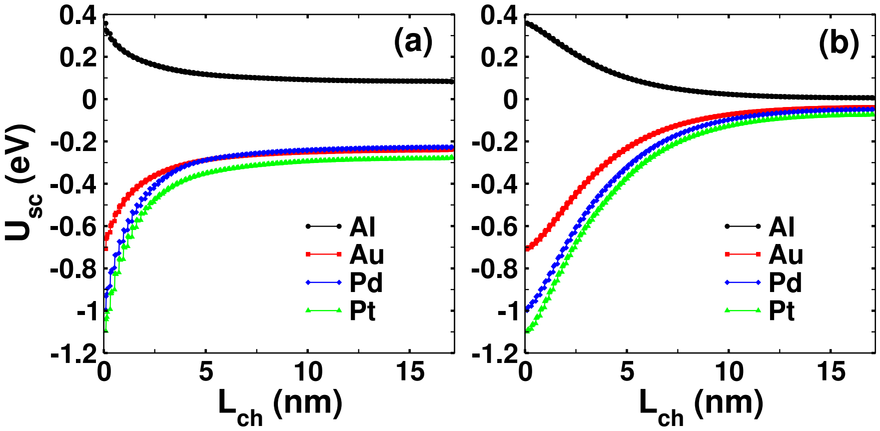

Figure 4.3: Potential profile for metal-GNR heterojunctions - Electrostatic potential profile U_{sc} as a function of the channel length L_{ch} for (a) N_a=14 aGNR and (b) N_a=16 aGNR contacted with *Au*, *Pd*, *Pt* and *Al* electrodes.

4.2.4 Quantum transport

Fig. 4.4 shows the influence of chemical bonding and electrostatics in the conduction mechanism of the studied systems. High work function *Au*, *Pd* and *Pt* metals give rise to qualitatively similar transport characteristics that originate from the electrostatic aspect of the heterojunctions. Namely, *p*-type conduction characteristics have been obtained for the 14 aGNR and low Schottky barriers with respect to the valence band (of the order of 0.2-0.3 eV) for the 16 aGNR.

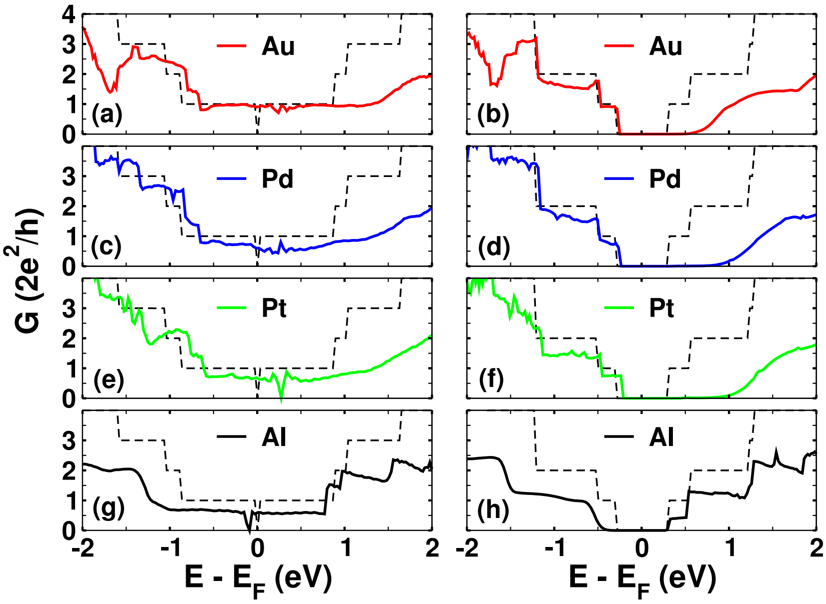

Figure 4.4: Conductance of metal-aGNR heterojunctions - Conductance as a function of energy for a N_a=14 aGNR (left column) and a N_a=16 aGNR (right column) contacted with: (a-b) *Au*, (c-d) *Pd*, (e-f) *Pt*, (g-h) *Al*. Dashed lines show ideal conductances for the respective aGNRs.

Fermi level to conduction band distances increase for the semiconducting ribbon with respect to the ideal case, arriving at $E_C - E_F \sim 1eV$ for *Pd* and *Pt*. In all cases conduction band charge flow is strongly suppressed, giving rise to a selective loss of the quantization steps that are typical of the 1D subbands in GNR structures. This behavior is related with the smooth bending of the conduction band that creates a state-free zone near the interface (see Fig. 4.2(a)). The combination of *p*-type characteristics and conductance suppression due to band-bending gives an asymmetric form to the overall conductance distribution (as similarly calculated also for CNTs[52]). In terms of chemical bonding only *Au* seems transparent near the Fermi level with the conductance arriving at the $1G_0$ plateau of the ideal case, whereas *Pd* and *Pt* demonstrate a slightly lower transparency. On the other hand, valence band transparency above the first conductance plateau is enhanced for *Pd* and *Pt*, which show a smaller extent of conductance fluctuations with respect to *Au*, making them more appropriate for high bias electrical measurements. A careful comparison between group 10 transition metals *Pd* and *Pt* shows that nonetheless the similarities deriving from their electronic structures, *Pd* shows a slightly better conductance response in the quantization steps of the valence band. The case of low work function *Al* electrode is distinct, since despite the contact-induced *n*-type doping (for the 14 aGNR) and quasi-ambipolar Schottky behavior (for the 16 aGNR), the dominant aspect that characterizes conduction is the strong scattering by the contacts. Here contact resistance constitutes the main factor of conductance suppression with respect to the ideal case, with quasi-blocked conduction channels and overall conductance degradation throughout the energy spectrum. It is therefore clear that the electrostatics and chemical bonding act complementary in metal-graphene nanostructures and a categorization of the metallic contacts on the basis of their transparency to graphene should incorporate a best compromise between these two aspects. Finally it should be noted that localized gap states that form near the metal-GNR interface (see Fig. 4.2(a),(b)) do not contribute to the transport process.

Current-voltage characteristics of the junction in the case of a pure N_a=16 AGNR contacted with different metals are reported in Fig. 4.5. Typical Schottky-diode characteristics are obtained with the high work function *Au* and *Pd* electrodes. Larger current values obtained for a negative bias in the case of *Pd* with respect *Au* are due to its slighter more pronounced *p*-type character. *Al* instead does not reproduce diode-like characteristics whilst on-off current ratios are too small for device operation.

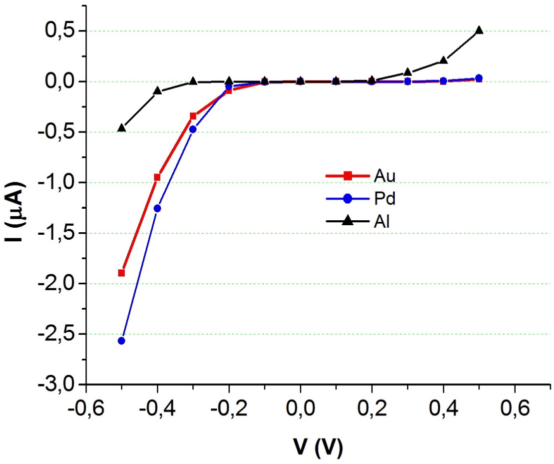

Figure 4.5: I-V curve for a metal-contacted N_a=16 aGNR - Current voltage ccharacteristics for a N_a=16 aGNR contacted with *Au*, *Pd*, *Pt* and *Al*.

Junctions between metals and zGNRs preserve similar qualitative characteristics with respect to aGNRs. However, the presence of the edge states in the channel material[99] and the accompanying large DOS near the Fermi level of these systems strongly enhances the role of localized electron-electron interactions. Hence, contrary to aGNRs, the electrostatic response is not uniform throughout the zGNR width and gives rise to a faster potential screening near the borders than in the center of the zGNR (Fig. 4.6(a)). Moreover, the reduced area of interface overlap between metallic and edge wavefunctions further hinders the transparent transmission of electrons in these systems (see the lower conductance with respect to the ideal case in Fig. 4.6(b)). It should be noted though that by the suppression of the edge state (e.g. due to corrugation from nanolithographic processes), transport and electrostatic properties are expected to converge towards the aGNR case.

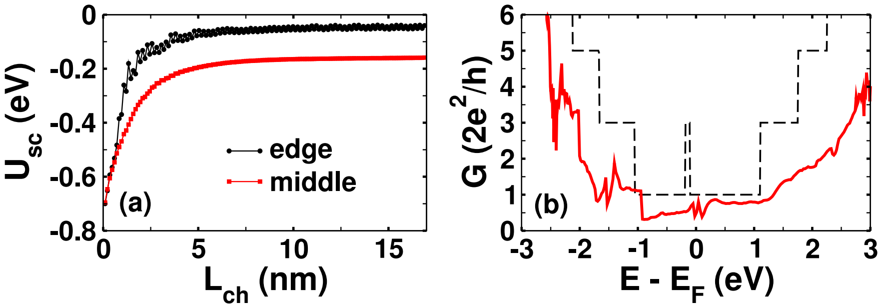

Figure 4.6: Transport and electrostatic properties of metal-zGNR heterojunctions - Electrostatic potential profile U_{sc} as a function of the channel length L_{ch} (a) and conductance as a function of energy (b) for a N_z=10 zGNR contacted with *Au*. The dashed line shows the ideal conductance of the zGNR.

4.3 High-bias aspects of graphene nanoribbon conduction

The second part of this chapter sees graphene as a zero-dimensional molecular system sandwitched between two metallic semi-infinite contacts. Electron quantum transport is theoretically studied here for finite-size armchair graphene nanoribbons biased within source and drain metallic electrodes, using an extended-Hückel-based Green's function coupled to a three-dimensional Poisson solver. The analysis evidences dynamic nonequilibrium electron charging phenomena that can affect the conduction mechanism by inferring electronic structure alterations. The scope here is to evidence out-of-equilibrium perturbations that give rise to effects that go beyond the semiclassical limit.

4.3.1 Methodology

The computational model is based on a self-consistent semiempirical approach of quantum transport developed by Zahid *et al.*[118] and extensively discussed in references 28, 29. The principal differentiation of this formalism with respect to the one presented in the first part of this chapter lies within the description of electron-electron interactions: Here the self-consistent potential $U_{SC}(\Delta\rho)$ reads:

$$U_{SC}(\Delta\rho) = U_{Laplace} + U_{Poisson}(\Delta\rho) + U_{Image}(\Delta\rho), \tag{4.1}$$

where $\Delta\rho$ represents the change in the charge density between the nonequilibrium and the equilibrium conditions ($\Delta\rho = \rho - \rho_{eq}$), whereas ρ is given by the expression below:

$$\rho = \frac{1}{2\pi}\int_{-\infty}^{+\infty} dE[f(E,\mu_L)G\Gamma_L G^\dagger + f(E,\mu_R)G\Gamma_R G^\dagger] \tag{4.2}$$

The presence of the Image term here simulates the presence of charges at the electrode part of the device. Both Poisson and Image terms of the self-consistent potential are part of the dynamic Poisson field description, with the latter numerically correcting the former on the position of the device contacts. The calculation of the Poisson term can derive in the framework of the complete neglect of differential overlap theory, using only the Hartree potential for the Coulomb interaction[118]. This approach has important numerical advantages with respect to a direct differential derivation since it allows convergences for relatively high biases. Laplace and Image expressions are determined numerically by solving the Laplace equation in real space with a finite element method, using the appropriate boundary conditions[118]. All three potential components are evaluated on the atomic sites of the AGNRs.

Rectangular armchair graphene nanoribbons have been considered (a semiconducting 12-AGNR and a metallic 14-AGNR following the terminology of ref. [99]) with hydrogen passivated armchair edges and zigzag edges strongly coupled to the two semi-infinite Au(111) contacts (see fig. 4.7). In particular the widths for the two ribbons are $W_{12-AGNR} = 13.6$Å, $W_{14-AGNR} = 16.07$Å, their length $L = 41.35$Å while mean Au-C atom distance has been set to $d \approx 2.2$Å by bringing the metallic contacts to a $d = 1$Å distance from the AGNRs ends. This strong metal-AGNR interface coupling along with the relatively large GNR width (see again ref. [99]) and the T=300K simulation temperature are expected to minimise spin polarisation effects of the zigzag edges on the conduction mechanism, thus spin-transport phenomena are not accounted for in the computational model[48]. Moreover a strong coupling regime is more likely to occur in experimental conditions where a wide area of the device sample is superimposed by the contact metal[58]. Only dynamic nonequilibrium charge transfer phenomena are being considered (i.e. no Schottky barrier aspects) by imposing the alignment between the metal's Fermi energy and the charge neutrality level of the AGNRs with a rigid shift of the AGNR energy bands with respect to the metallic ones. This approach is correct for small channel-lengths in a molecular bridge geometry. Finally simulations have been undertaken in equilibrium as well as with 1V, 2V and 3V applied biases for both types of AGNRs.

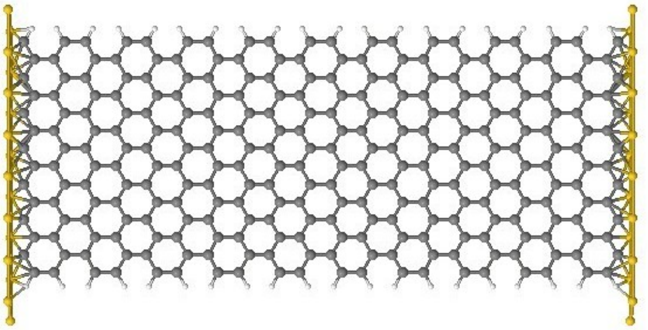

Figure 4.7: Two terminal metal-GNR-metal geometry - Schematic representation of a 14-AGNR end-contacted with source and drain Au(111) contacts in the two terminal geometry.

4.3.2 Electrostatics of the metal-GNR-metal syytem

The principal aspects of device-electrode interaction are the chemical nature of the interface bonding and the charge transfer that can take place between them. Both characteristics have an important influence on the conduction process. The first is incorporated in the self-energy matrices $\Sigma_{L,R}$ and gives rise to an increased local density of states of the device atoms near the contacts [29] while the second is captured in the current formalism by the self-consistent potential of eq. 4.1 and gives rise to a change of the device's electronic structure. Fig. 4.8 shows this potential on the area of the 14-AGNR device when a 2V bias is applied. There are two features of the U_{SC} that require attention: a) the initial screening which takes place in the interface area between the device and the contacts (that corresponds to a screening of charges near the contact edges of the AGNR), which lowers the total potential value with regard to the static Laplace term, and b) the local alteration of the potential value at the four corners of the nanorribon, which gives a three-dimensional conduction aspect in these one-dimensional structures and that indicates that dynamic charge transfer phenomena are nonuniform and can be less smooth in corrugate graphene samples than in smoothly terminated ones. Both quantitatively and qualitatively similar results have been obtained for the semiconducting 12-AGNR, demonstrating that charge transfer phenomena in AGNRs are independent from the conduction character of the nanoribbon. This last observation comes to contrast with equivalent carbon nanotube calculations where the shape of U_{SC} was found dependent from the chirality and conduction character of the studied nanotube[29].

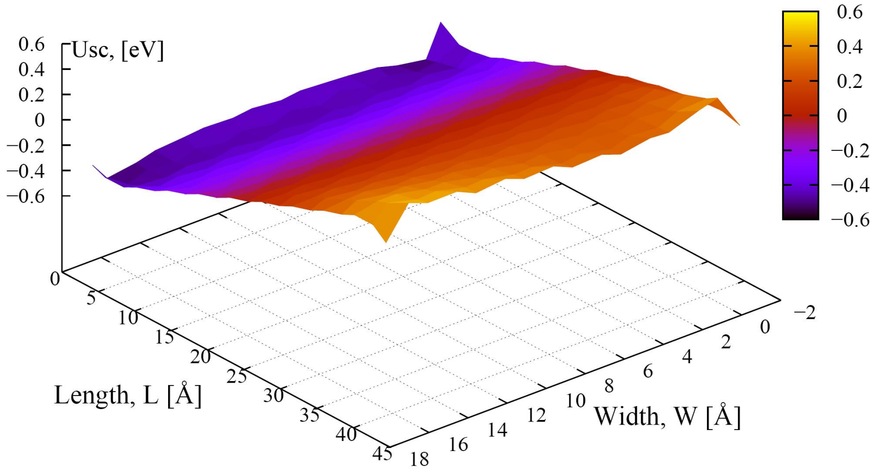

Figure 4.8: Potential profile for a Au-GNR-Au molecular system - Spatial distribution of the self-consistent potential U_{SC} for the 14-AGNR for a 2V applied bias.

4.3.3 Conduction aspects

The best way to visualise the conducting capacity of finite nanostructures is by the schematisation of their transmission probability, which can derive directly from the nonequilibrium Green's function formalism. It can be expected that the latter changes with the application of bias since the U_{SC} term is directly related to the potential difference applied on the two electrodes. Figure 4.9 shows the transmission as a function of energy for the two AGNRs when a 0V, 1V, 2V and 3V bias is applied. From the equilibrium diagrams one can draw conclusions on the conducting character of the two ribbons that comply with previous band-structure calculations[97, 99], since the 12-AGNR is semiconducting with a gap of $\approx 0.5eV$ while the 14-AGNR is metallic with an single subband near its Fermi level. It is also worth mentioning that the finite character of this AGNRs is manifested by the presence of transmission peaks, instead of the bands of the infinite 1D structures. The application of bias provokes an alteration on the transmission probability of the two systems that has both general and singular characteristics. The general aspect of these alterations is a total reduction of the transmission probability with the increase of bias, which can be translated in a diminishment of the current-carrying capacity of the AGNRs, or equivalently with the increase of a dynamic resistance that is formed out of the traditional inelastic scattering mechanism. The singular aspects are related with transmission alterations near the Fermi level zones of the two ribbons. In the case of the 12-AGNRs, the peaks near the gap edges of the equilibrium spectrum shrink and tend to diminish at 1V and 2V bias, while a single peak tends to form in the middle of the conduction gap with a 3V bias. On the other hand, in the metallic AGNR's case no important change takes place in the onefold degenerate zone near the Fermi level.

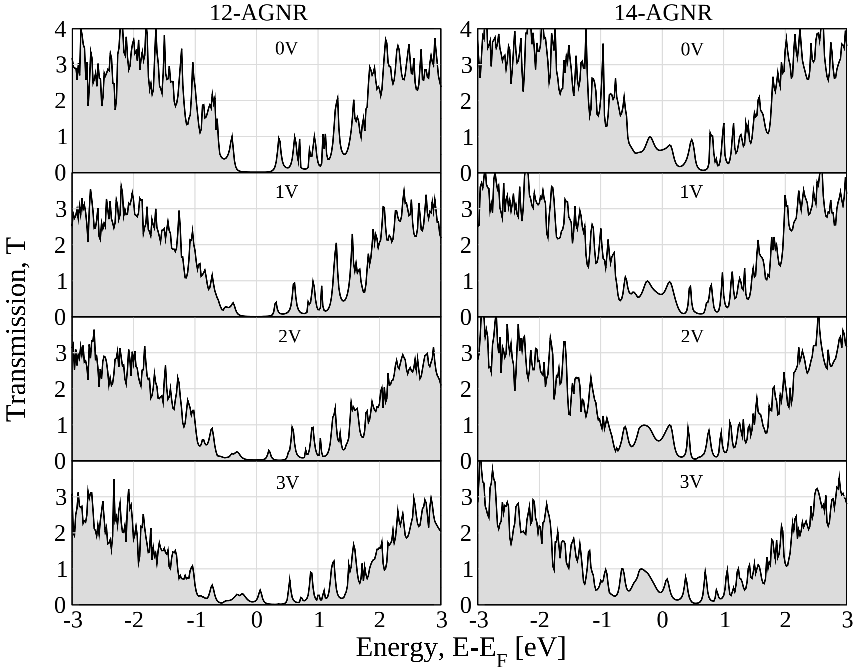

Figure 4.9: Bias-dependent transmission coefficients for aGNRs - Transmission as a function of energy for a 12-AGNR (left column) and a 14-AGNR (right column) with $L = 41.35\text{Å}$ for 0V, 1V, 2V and 3V applied bias.

4.3.4 Bias-DOS tracking interactions

The physical understanding of the presented phenomena requires an in depth study of the electronic structure alterations that provoke the aforementioned current-carrying capacity limitations. In this sense a local density of states (LDOS) analysis is indicated for a topological determination of the device's electrical behaviour with regard to the application of bias. This analysis shows similar generic characteristics with respective ones presented for carbon nanotube molecular bridges[29], namely increased LDOS values in the area near the contacts due to the tails of the metal's electron wavefunctions that tend to fade exponentially while moving towards the internal parts of the AGNRs, and a spectrum respective to the conducting character of each AGNR with finite LDOS values for the 14-AGNR and a lack of states near the Fermi level for the 12-AGNR in the inner parts of the device. In a single atom level, a representative picture of the alterations that take place in the process of bias application can be seen in figure

4.10, where the LDOS for two inversely equidistant C atoms from each one of the two metallic contacts is demonstrated. The two C atoms have an equal distance $d = 11.7\text{Å}$ from the electrode that lies closer while their width coordinate W is common ($W_C = 7.41\text{Å}$ with $W_{C_{min}} = 0\text{Å}$, $W_{C_{max}} = 14.54\text{Å}$ for the 12-AGNR and $W_{C_{max}} = 16.05\text{Å}$ for the 14-AGNR). According to quantum transport theory, when a bias is applied to the contacts, the two electrochemical potentials $\mu_{L,R}$ (that in equilibrium have the same value) separate, taking in this case a minimum and a maximum value respectively. The self-consistent calculations demonstrate that the LDOS of each atom tends to follow the electrochemical potential of the contact to which it is better correlated from a chemical/topological point of view. This bidirectional alteration of the LDOS under bias provokes a localisation of states that find it more difficult to correlate with states of near atoms. Such change on the electronic structure of the biased device has the effect seen earlier on the conducting character of the system with the total reduction of the transmission probability. When it comes to the energy zone near the Fermi level of the device, even though the LDOS behaviour does not differentiate from the general picture, the macroscopic outcome is clearly distinct. In the case of the semiconducting 12-AGNR, the LDOS movement provokes a localisation of the states that appear within the conduction gap, therefore transmission peaks near the gap tend to disappear. As the bias gets bigger and reaches the 3V value, the LDOS shift becomes high enough for the gap states to come close enough for the reappearance of correlation effects, which give rise to a small mid-gap finite transmission value in the respective spectrum. On the other hand, in the case of the metallic 14-AGNR, although the $LDOS - \mu_{L,R}$ tracking movement is similar, the continuous presence of states near the Fermi zone makes localisation effects less influent for the transmission probability and the conducting character of the system. Finally, although the picture sketched previously considers only two C atoms, qualitatively similar results have been obtained for the whole of the studied structures, being in accordance with previous analysis on carbon nanotubes and organic molecules[29].

4.4 Conclusions and discussion

In this chapter we have investigated various aspects that arise for the conduction properties of graphene nanoribbons when these are attached to metallic electrodes. In the first part, the study has addressed the problem of metal-GNR heterojunctions within an atomistic approach that deals with both the electrostatics as well as the chemical aspects of the interface. Results have shown that band-bending, doping and bonding characteristics of this interaction can non-trivially influence the conduction mechanism, giving rise to conductance asymmetries,

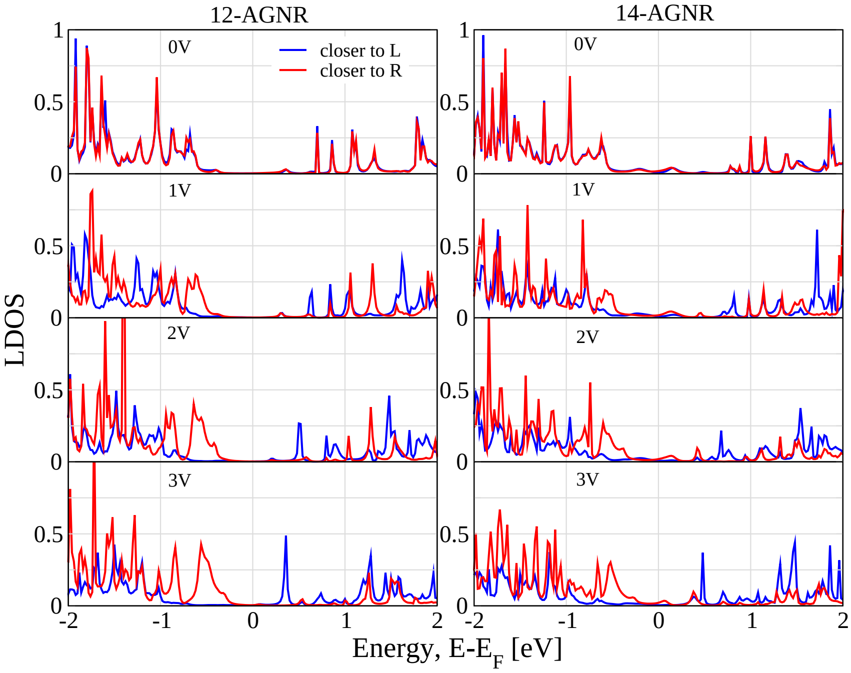

Figure 4.10: Bias-dependent local density of states alterations for aGNRs. - Local density of states as a function of energy for two inversely equidistant C atoms from each one of the two contacts, for a 12-AGNR and a 14-AGNR. Each C atom distances $d = 11.7$Å from the respective nearest metallic contact whereas their width coordinate W is common. The application of bias, which separates the electrochemical potentials $\mu_{L,R}$ of the contacts bringing them to a minimum and a maximum value respectively, provokes also a shift of the LDOS of each C atom towards energies that are closer to the contact electrochemical potential to which they are better correlated.

Schottky barriers and suppression of ideal transport properties. An important conclusion is that the electrostatics and the chemical bonding aspects can act complementary for the determination of contact transparency in graphene. We have moreover discussed some common characteristics between two similar 1D sp^2 carbon allotrope systems, i.e. GNRs and CNTs. Within a certain qualitative framework, this work argues that theoretical/experimental knowledge obtained for metal-CNT heterojunctions can be also valid in the case of GNRs. It is therefore crucial to understand the pros and cons of the two systems in terms of fabrication/growth/patterning methods and electrical/mechanical/optical characteristics in order to distinguish the ideal candidate for post-Si nanoelectronic applications.

The second part of this chapter dealt with dynamic nonequilibrium conduction phenomena for GNR molecular bridges in the high-bias regime. Attention was paid on the role of charge transfer on the conduction mechanism while local density of states alterations have been revealed under bias application. The main aspects of this self-consistently calculated procedure can be summed up in the three-dimensional characteristics of the potential profile due to a nonuniform charging manifestation, the reduction in the current-carrying capacity of the GNRs under bias due to the localisation of the electronic wavefunctions and the distinct (according to the conducting character) transmission probability response of the two structures near the Fermi energy level. All these features are highly interrelated and derive from a tracking device-DOS and contact electrochemical potential interaction revealed under bias. It can be expected that the presence of the aforementioned processes is not confirmed in the semiclasical case. There, the device can be thought of as the sum of numerous nanosize discretised units where quantum rules can be implemented. In such case, the potential profile that each of this units perceives is flat and therefore no bidirectional LDOS modifications are expected, rather than a unified movement of all states towards the respective potential level. Finally, considerations have to be made from an engineering point of view, since bias-induced electronic structure alterations should be taken into account in the projection of nanoscale graphene devices.

Chapter 5

Epitaxial graphene on SiC substrates

5.1 Introduction

Epitaxial graphene has emerged as a highly attractive alternative for CMOS graphene integration by providing a combination of characteristics that constitute a significant advantage with respect to complementary/antagonistic growth technology: wafer size scales[32, 74] and direct growth on semi-insulating substrates. The growth process is based on the sublimation of Si atoms starting from both on[111] or off axis [12] SiC substrates in ultra high vacuum or ambient pressure furnaces[61]. Accurate control of the growth process allows for the formation of graphene films, as thin as a monolayer, from the remaining C surface atoms. The structural, electronic and transport properties of epitaxial graphene strongly depend on the the polarization of the SiC surface: Si-face epitaxial graphene (i.e. graphene on the (0001) surface) is characterized by the formation of a first carbon-rich interface layer (buffer layer) with a $6\sqrt{3} \times 6\sqrt{3}R30^\circ$ surface reconstruction, over which AB (Bernel) stacked graphene layers grow. Interface interaction imposes significant n-type doping while scatterers reduce mobility values with respect to the SiO_2 deposited case[32]. Typical graphene characteristics (e.g. half-integer quantum hall effect) are recovered by the application of a gate voltage that lowers the Fermi level around the Dirac point[62] or by the decoupling of the buffer layer from the substrate via oxidation[83] or hydrogen intercalation[94]. C-face epitaxial graphene (i.e. graphene on the $(000\bar{1})$ surface) is subject to a less stringent rotational ordering with respect to the substrate[102] whereas the presence of an interface buffer layer, although predicted by theoretical calculations[75, 87, 109], is still a matter of debate[12, 49, 53, 103]. A complex rotational symmetry of subsequent graphene layers other than the AB stacking sequence is present [102] that allows for the manifestation of single-layer properties even in the case of a multilayer structure[50, 101]. C-face monolayers show higher mobilities with respect to the (0001) case and the typical half-integer quantum hall effect at low temperatures[12, 114]. Doping is also present here, however significantly smaller with respect to the (0001) case. Both electron[105] and hole carrier injection[12, 114] has been reported in the literature for C-face graphene structures.

This chapter will study the effect of both Si and C-face SiC substrates on the electronic and transport properties of epitaxially-grown graphene. In the first part we will focus on Si-face-grown graphene. Here the theoretical/experimental understanding of the interface is well-established and the scope is to discuss the role of lateral confinement in these systems for bandgap engineering and device integration issues. To this purpose an appositively parameterized semiempirical Hamiltonian will be used that allows for scaling, giving at the same time an atomistic description of both the device and the substrate. In the second part of the chapter we will focus instead on the C-face-grown graphene. In this case there are still important structural and electronic issues to be answered from a theoretical point of view and the methodological treatment will be fully *ab initio*.

5.2 Epitaxial graphene nanoribbons on SiC(0001)

It is nowadays commonly accepted that epitaxial graphene on silicon carbide substrates represents a viable method of controllable growth for the fabrication of high-quality graphene wafers [32]. The universally accepted concept for the (0001) surface is that the process of graphitization takes place with the formation of an interface carbon layer (buffer layer) which decouples the electronic properties of the substrate from those of the subsequent graphene layers[93]), allowing the formation of both covalent and unsaturated bonds in the heterostructure's interface area. In the first part of this chapter we focus on Si-face grown films, where although the theoretical/experimental framework seems in agreement (e.g. n-type doping effects[32, 75]), there are still open questions concerning the impact of one-dimensional (1D) confinement as well as the measured mobilities found to be lower ($2000 cm^2V^{-1}s^{-1}$ at low temperatures [32]) than respective ones for films deposited on SiO_2.

5.2.1 Methodology

We start off by studying the electronic structure of 1D armchair graphene nanoribbons (AGNRs) with one or more layers grown on SiC(0001), considering an atomistic description of the epitaxial layers and the substrate. The quantum chemistry is used within the extended Hückel Theory on an sp^3d^5 Slater-type basis that considers both valence and polarization orbitals. This approach has been followed for the electronic structure study of 1D carbon allotrope structures [64, 92] and allows for the study of relatively large complexes (up to 4.4 nm wide in this work) respecting at the same time the chemical environment. The Slater parameters used here have been extracted from DFT calculations on SiC [15] and have been extensively tested to reproduce well also the bandstructure of sp^2-hybridized AGNRs (see fig. 4.2). Results show that the role of the buffer layer is not limited in the separation of the electronic properties of the substrate from that of graphene, but becomes an active component of the heterostructure's electronic behavior through energy states that are introduced from the dangling bonds of the SiC surface. These states pin the Fermi level of the system even in the case where the AGNR consists of up to three graphene layers, while such behavior is independent from the width of the considered nanoribbons.

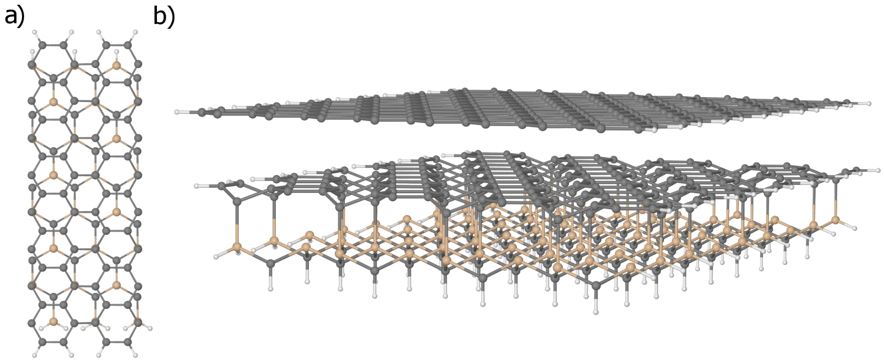

Figure 5.1: Geometrical representation of an epitaxial 17 AGNR - Geometrical representation of a 17 AGNR: (a) unit cell of the SiC(0001)/graphene interface with a $\sqrt{3}\times\sqrt{3}R30°$ surface reconstruction (top view) and (b) single-layer AGNR (side view).

We consider graphene nanoribbons on SiC substrates on the basis of relaxation information of ref. [75] obtained by *ab initio* molecular dynamics within the spin local density approximation. The surface here is reconstructed in a numerically more convenient $\sqrt{3}\times\sqrt{3}R30°$ basis that does not significantly alter the physics with respect to the experimental case. In this study, the substrate is formed by a single bilayer of SiC which is responsible for all bonding interactions with the carbon buffer layer, while hydrogen saturation has been imposed towards the bulk (fig. 5.1). The buffer layer stands at $d = 2.58$Å over the SiC substrate, while interface atoms that covalently bond relax at $d = 2$Å. We will consider the composite substrate-buffer system as the base system from now on. Subsequent graphene layers follow graphite's ideal planar interlayer relaxation($d = 3.35$Å).

Considering a unit cell n of the 1D periodic structure, we calculate the bandstructure of various AGNRs by direct diagonalization of the k-space Hamiltonian matrix

$$[H(\vec{k})] = \sum_{m} [H]_{nm} e^{i\vec{k}\cdot(\vec{d}_m - \vec{d}_n)}, \tag{5.1}$$

where $\vec{k}$ is the Block wavevector within the first Brilouin zone. The summation over m runs over all neighboring unit cells with which unit cell n has any overlap (including itself) [26], while matrices $[H]_{nm}$ are written in real space on the previously discussed set of orbital functions[1]. Vectors $\vec{d_m}$ and $\vec{d_n}$ show the position of two equivalent points of unit cells m and n. The generalized eigenvalue equation reads [64]:

$$[H(\vec{k})]\Psi_i(\vec{k}) = E_i(\vec{k})[S(\vec{k})]\Psi_i(\vec{k}), \tag{5.2}$$

where $[S(\vec{k})]$ is the k-space overlap matrix calculated in an analogous to eq. 5.1 way, and $\Psi_i(\vec{k})$ $(E_i(\vec{k}))$ is the eigenvector (eigenvalue) of the i^{th} subband.

5.2.2 Electronic structure

The study will built up on an ideal reconstruction of the epitaxial process, from the SiC substrate up to 5-layer nanoribbons, considering various semimetallic and semiconducting AGNRs (consistent with the terminology of ref. [99]). The single-SiC-bilayer 1D substrate presents a dispersion relation with an indirect gap of $E_g = 3.53eV$ for all cases, closer to the α-SiC polytypes. Such deviation from the 3D bulk case can be strictly attributed to the perpendicular confinement and results in a shift of the conduction band towards higher energies. The first step towards graphitization is achieved by the formulation of the interface buffer layer. Here, the breaking of symmetry for the two complementary triangular sublatices that constitute the ideal graphene structure results in a complete alteration of the typical AGNR bandstructure, with the presence of a wide energy zone that for the most part is not crossed by any subband, while the Fermi level of the system is captured by weakly dispersive midgap bands (fig. 5.2). It is interesting to note that due to deviation from planarity and selective covalent bonding, the buffer layer looses also the typical characteristic of 1D-confined graphene, that is the dependence of its electronic structure from its width. The process continuous with the successive addition of extra graphene layers on the systems that contrary to the buffer layer are Van der Waals bonded and preserve their sp^2 planar topology. The first layer upon the buffer one restores typical AGNR behavior [99], namely an almost linear dispersion curve with a secondary confinement-induced bandgap

---

[1] For $n \neq m$, $[H]_{nm}$ are interaction matrices between neighboring unit cells, whereas in the case of $n = m$, $[H]_{nn}$ refers to the Hamiltonian matrix of unit cell n.

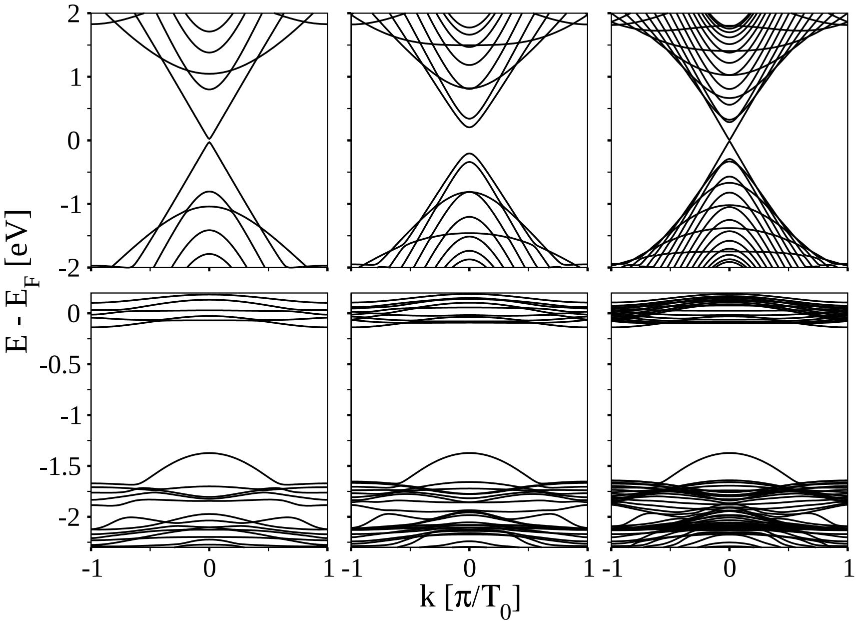

Figure 5.2: Bandstructure of SiC(0001)/graphene interface systems. - Bandstructure of an ideal (a) 11 AGNR, (b) 17 AGNR and (c) 35 AGNR. SiC(0001)/graphene interface systems corresponding to a (d) 11 AGNR, (e) 17 AGNR and (f) 35 AGNR. T_0 denotes the translation vector of the respective 1D periodic structure.

for the semimetallic AGNRs, and the presence of wider gap in the semiconducting case (see fig. 5.3 for a 17 and a 19 AGNR). The fundamental concept thought is that the Fermi level remains pinned by the almost flat subbands of the base system, imposing and overall metallic character and *n*-type doping for all types of nanoribbons. This trend continuous with the addition of a second layer, with ribbons showing the typical parabolic dispersion curve below the trapped Fermi level. Results show that such behavior continues for up to three layers of confined graphene, while from the forth layer and onwards, the highest occupied subband gradually disperses towards graphite's Fermi level position for small values of the wavevector. This picture brings to discussion two important aspects: a) the main electronic properties of two-dimensional epitaxial graphene on SiC [75] are confirmed also in the case of 1D graphene nanoribbons. b) The important role of confinement for suspended or SiO_2-deposited graphene is strongly compromised in the case of SiC substrates due to the Fermi level pinning effect and the intrinsic metallic behaviour of all AGNRs.

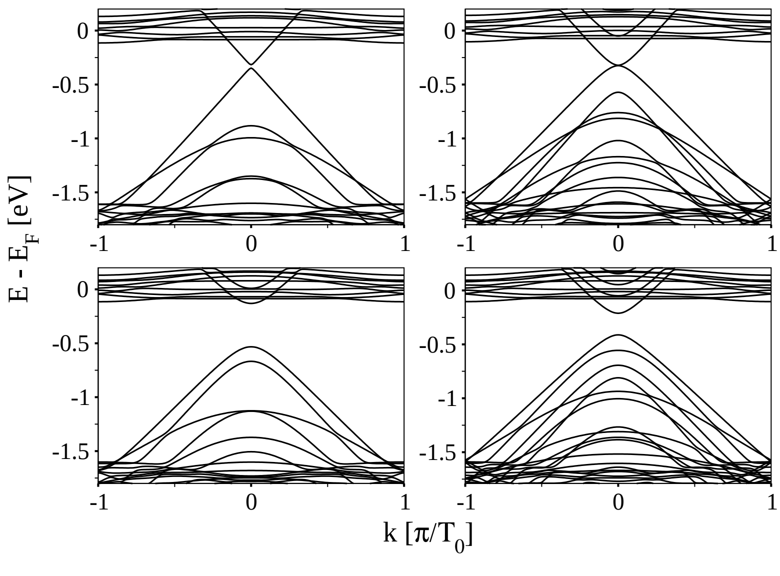

Figure 5.3: Bandstructure of single and double layer epitaxial graphene nanoribbons. - Bandstructure for AGNRs grown over the SiC(0001)/graphene interface system: (a) a single-layer 17 AGNR, (b) a double-layer 17 AGNR, (c) a single-layer 19 AGNR and (d) a double-layer 19 AGNR. T_0 denotes the translation vector of the respective 1D periodic structure.

5.2.3 Quantum transport

We now move forward to better understand the importance of Fermi level positioning for the conductive characteristics of SiC grown AGNRs. For this purpose we follow a real-space approach with the objective of identifying the topological distribution of the density states for energies around the Fermi level. We use the non-equilibrium Green's function formalism for a 1D device with ideal semi-infinite contacts. The Green matrix reads:

$$[G] = (E[S] - [H] - [\Sigma_{left}] - [\Sigma_{right}])^{-1}, \tag{5.3}$$

where E is the energy, $[H]$ ($[S]$) is the Hamiltonian (overlap) matrix written in real-space on the same basis as before, and the $[\Sigma_{left,right}]$ matrices introduce the role of scattering due to the left and right semi-infinite contacts. The latter are calculated within an optimized iterative scheme [95]. The device spectral function is the anti-hermitian part of the Green matrix $[A(E)] = i([G] - [G^{\dagger}])$, from which the local density of states (LDOS) at energy E and position $\vec{r_\alpha}$ can be defined as:

$$LDOS(\vec{r_\alpha}, E) = \int_{\mathbf{R}} \frac{Trace[A(E)][S]}{2\pi} \delta(\vec{r} - \vec{r_\alpha}) d\vec{r}, \tag{5.4}$$

where δ is the Delta function and $\vec{r_\alpha}$ shows the positions of the atomic sites. Integrating eq. 5.4 over all the atomic positions results in the total density of states of the system. Finally, transport calculation can be introduced in the formalism by the definition of the zero-bias transmission coefficient $T = Trace([\Gamma_{left}][G][\Gamma_{right}][G^{\dagger}])$, where $[\Gamma_{left,right}]$ are the contact spectral functions [26].

We consider an 11 AGNR with a singe graphene layer over the base system and calculate the LDOS for energies around the Fermi level position (fig. 5.4). Results show that the almost flat subbands around the Fermi level are primarily projected in the xyz space on the highly localized positions of the substrate's non-saturated Si-bonds. Such phenomenon raises a key issue for the conductive capacity of these systems, since it implies that the substrate becomes an active component of the conduction process, whereas the unsaturated Si atomic sites constitute conductive interface defects. Moreover such implication suggests that electrical conduction through epitaxial SiC nanoribbons can lead to a great reduction of the carrier mobility with respect to the SiO_2-deposited case and could be also related to the different conducting characteristics observed for epitaxial graphene on $(000\bar{1})$ and (0001) substrates. It is worth mentioning that as soon as we leave the energy zone of the weakly dispersed interface subbands and move towards lower energies that restore the typical nanoribbon bandstructure, LDOS is located on the single graphene layer. It can be therefore argued that by perpendicular electric field modulation (e.g. using a gate electrode) the system's Fermi level can be detached from the substrate states and electrical conduction can recover the typical graphene characteristics.

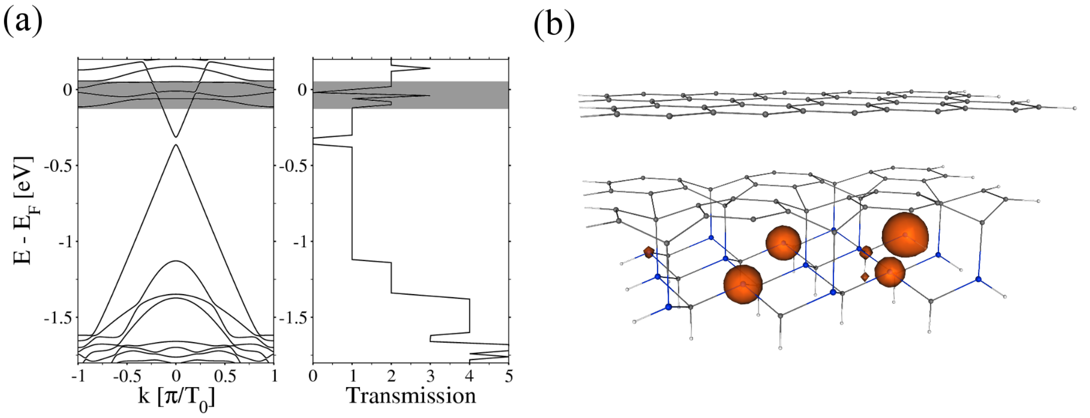

Figure 5.4: Qauntum transport and local density of states for an epitaxial 11 AGNR. - (a) Bandstructure and transmission as a function of energy for an 11 AGNR. (b) Schematic real-space representation of the LDOS corresponding to the grey energy region of figure 5.4(a). The radius of each sphere is proportional to the amplitude of the LDOS value on that atomic site. T_0 denotes the translation vector of the respective 1D periodic structure.

5.3 Epitaxial graphene on the C-fase of SiC

The importance of the interface in every heterostructure is fundamental for the determination of the electrical properties of the composite material, since this is often accompanied with defects, stresses and further alterations of the ideal atomic structure that can comport dominant structural, electrical and quantum transport implications. In the case of epitaxial graphene this concept becomes even more important, since the interface by itself forms almost the one out of the two composites of the heterostructure. This situation is clear in the Si-face case, where e.g. Fermi level pinning effects have been identified in the SiC(0001)/graphene interface both theoretically (see the first part of this chapter) and experimentally[100]. However the apparent diversity of the electronic and transport properties of C-face epitaxial graphene makes necessary a clear explanation of interface properties that reconciles to the best way possible the mismatch of experimental data (see paragraph 5.1). In the second part of this chapter we perform first-principles calculations for single and double graphitic layers epitaxially grown on 4H-SiC(000$\bar{1}$) surfaces. The scope here is to investigate the fundamental structural and electronic properties of C-face grown graphene and confront them with those of the Si-face one. A particular attention will be paid to the presence interface-driven phenomena like magnetism and Fermi-level pinning effects.

5.3.1 Methodology

We perform *ab initio* calculations based on the density functional theory (DFT) within the Local Spin Density approximation (LSDA) as implemented in the SIESTA computational code[98]. The 4H-SiC epitaxial graphene structures comprise of four bilayers of a (4×4) SiC substrate over which $R0°$ single and double layers of graphene grow (194 and 244 total atoms in the slab respectively), forming a (5×5) supercell that satisfies lattice commensuration and minimizes non-physical stresses. Epitaxial graphene samples on SiC$(000\bar{1})$ with an angular distribution around 0° with respect to the SiC $\langle 21\bar{3}0 \rangle$ direction are often seen in experiments[102]. A basis set of double-ζ valence (plus polarization) orbitals has been used for C and H (Si) whereas Troulier-Martins pseudopotentials[108] are used to model ionic cores. Basis set sensitivity and pseudopotentials have been tested to accurately reproduce the bandstructure of hexagonal SiC polytypes and graphene. Sampling of the Brilouin zone takes place by a $2 \times 2 \times 1$ Γ-centered Monhorst-Pack grid, while a mesh cutoff energy of 500 Ry has been imposed for real-space integration. All structures have been relaxed until forces were less than 0.04 eV/Å.

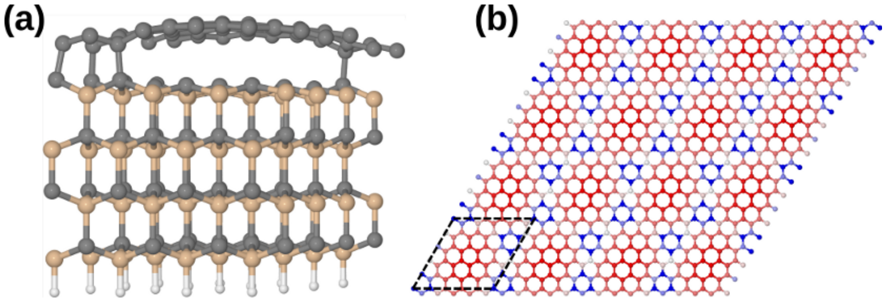

Figure 5.5: Graphene monolayer on a (4×4) SiC$(000\bar{1})$ substrate - (a) Side view of a graphene monolayer on a (4×4) SiC$(000\bar{1})$ substrate. The SiC slab comprises of silicon/carbon bilayers that are passivated with H at the bottom. The graphene layers forms with a 0° angle with respect to the $\langle 21\bar{3}0 \rangle$ direction of the SiC substrate. (b) Color map view of the first graphene layer showing the bonding characteristics of this layer with the substrate. Gradual red to blue coloring indicates bigger to smaller distances from the substrate and sp^2 to sp^3 bonding respectively. Dashed lines show the periodically reproduced unit cell.

5.3.2 Structural and electronic properties

Fig. 5.5(a) shows the geometrical configuration of a graphene monolayer at the end of the relaxation process. This layer presents an important corrugation and has a thickness $t \sim 1$ Å with a structural relaxation that presents some fundamental differences with respect to the buffer layer of the SiC(0001) case[65, 75]. A periodic reproduction of the unit cell (Fig. 5.5(b)) shows the presence of $\sim 3 \times 3$ Å islands that represent the areas of the layer that are more distant from the substrate ($d \sim 3$ Å) due to a particular surface reconstruction of the SiC substrate where also substrate carbon atoms strongly sp^2 hybridize (see the next paragraphs fo a detailed discussion). These islands are weakly coupled to the substrate and strongly preserve a π-type hybridization in their atomic orbitals. Such graphitic quantum dots are terminated by carbon atoms that are strongly coupled to the substrate and loose their sp^2 hybridization for the sp^3 one, forming covalent bonds with the substrate carbon atoms. It should be noted that in this geometrical configuration for the graphene layer stresses are minimized, since sp^2 bonds have a mean distance of $C - C_{sp^2} \approx 1.42$ Å whereas sp^3 ones relax at $C - C_{sp^3} \approx 1.67$ Å, which slightly exceeds that of pure diamond. This model has similarities and some significant differences with the previous one based on the $\sqrt{3} \times \sqrt{3}R30°$ surface reconstruction[75]. It still implies that there can be no single graphene layer that grows directly on the $(000\bar{1})$ surface without some kind of covalent bonding with the substrate, however, the smooth corrugation and island-like relaxation is beyond the previous model and consistent with experiments[53, 103].

Fig. 5.6 shows the electronic bandstructure of the first graphenic layer on 4H-SiC$(000\bar{1})$. The key point is that this layer preserves a purely metallic character with π bands that prevail within the SiC-substrate bandgap, in a clear contrast with the zeroth carbon-rich layer grown on the Si-face[109]. The metalicity of this first graphene layer is also consistent with electrical measurements performed on single graphene layers on C-face SiC[53]. However the interaction with the substrate, notwithstanding weak, smoothens the Dirac cones and the π bands do not preserve the typical free-standing graphene linearity near the Fermi level. A careful view of the spin polarized bandstrucute (Fig. 5.6(b-c)) in this system shows some important differentiations with respect to the spin unpolarized one (Fig. 5.6(a)). In both faces of epitaxially grown graphene, the presence of quasi-flat bands near the Fermi level of these systems derives from dangling bonds states in the interface between the substrate and graphene. In the Si-face, such dangling bond states pin the Fermi level of the heterostructure at energies above the charge neutrality point of ideal graphene (i.e. giving rise to an n-type doping of the system)[30]. From the spin-unpolarized bandstructure one can deduce that the same effect takes place also in the case of C-face graphene, with the only difference

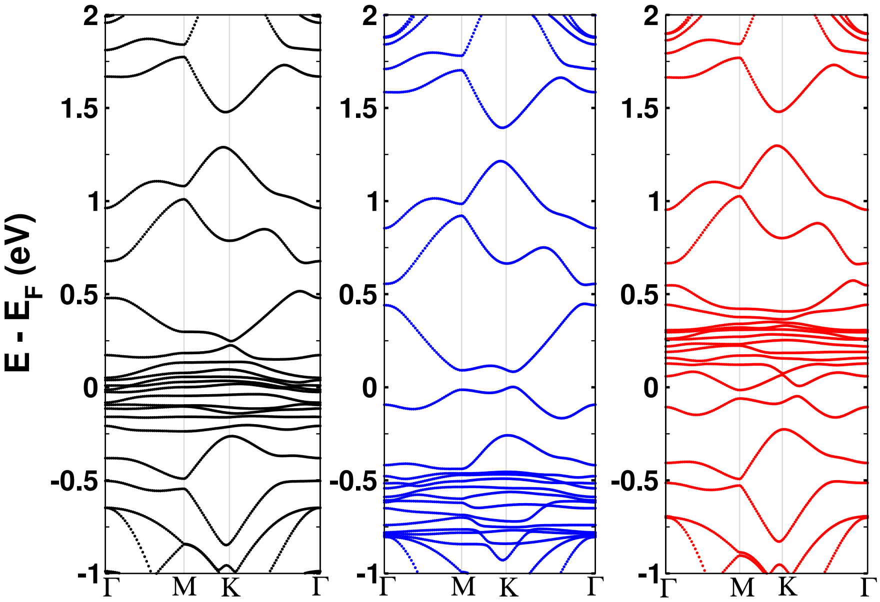

Figure 5.6: Bandstructure of a single graphene layer on a SiC(000$\bar{1}$) - Bandstructure of a single graphene layer on a SiC(000$\bar{1}$) substrate. Both spin unpolarized (left) and polarized (↑ middle, ↓ right) configurations are shown.

that the dangling bond states have energies that lie near the Fermi level. However the spin-polarized structure shows a different picture: here dangling bond states are half-filled and the presence of strong exchange interactions makes them split by $\approx 0.7 - 0.8eV$ above and below the Fermi level respectively. Hence, the Fermi level of (000$\bar{1}$) systems remains unpinned by the interface, which is consistent with the very low carrier concentrations found experimentally[114].

5.3.3 Magnetic properties

The presence of significant exchange interactions makes necessary a more careful analysis of magnetism issues in the interface of these systems. Fig. 5.7 majority (↑) and minority (↓) spin density of states and electronic density configurations for the graphene/4H-SiC(000$\bar{1}$) system. The total DOS (Fig. 5.7(a)) reveals the presence of a very big concentration of ↑ states from $0.3eV$ to $1eV$ below the Fermi level, and similarly for the ↓ states from $0eV$ to $0.5eV$ above the Fermi level. A careful analysis of the orbital-resolved projected density of states on the carbon atoms of the first SiC bilayer below the graphene layer (Fig. 5.7(b)) shows that a major component of these two peaks derives from the those carbon atoms that are not covalently bonded with the graphene overlayer. Moreover, the contributions of the π orbitals are almost exclusive in these peaks (the remaining

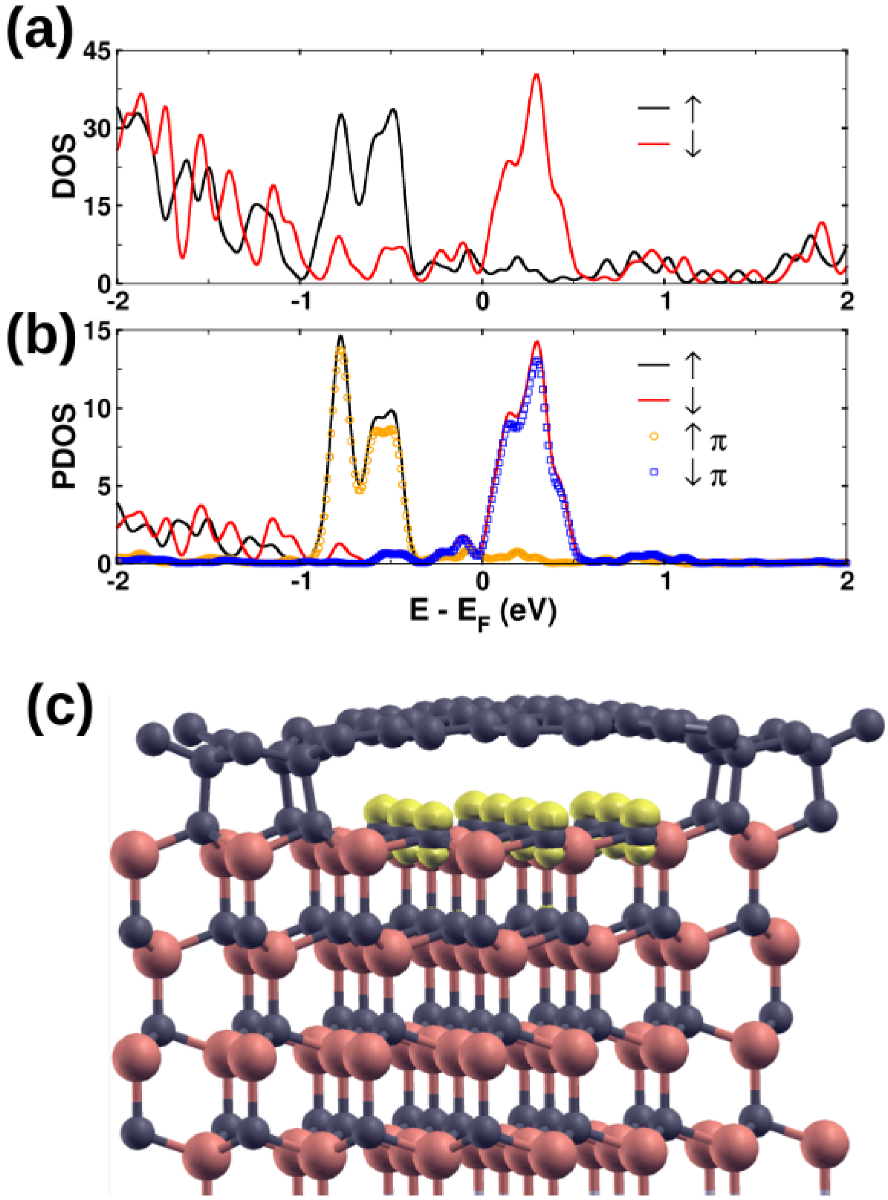

Figure 5.7: Density of states of a single graphene layer/4H-SiC(000$\bar{1}$) - (a) Total ↑ and ↓ density of states of a single graphene layer/4H-SiC(000$\bar{1}$) system. (b) Projected ↑ and ↓ density of states (PDOS) on the carbon atoms of the first SiC bilayer below the graphene layer (lines). The contribution of the π bands on the PDOS is also shown (symbols). (c) Local magnetization ($\rho_{\uparrow} - \rho_{\downarrow}$) for the previous system, where yellow isosurfaces indicate an excess of ↑ electrons.

π orbitals that can be found in the system are localized at the monolayer). This picture implies that the interface carbon atoms of the substrate that do not bond covalently with the first graphenic layer strongly sp^2 hybridize and tend to form a graphitic interface with the overlying carbon atoms that correspond to the graphenic quantum dot islands of the monolayer. Moreover, the $\uparrow$ and $\downarrow$ band-splitting gives rise to local magnetization phenomena at the heterostructure's interface (Fig. 5.7(c)) where due to the excess of $\uparrow$ electrons a ferromagnetic order is present. This magnetic aspect of the interface influences the electronic bands of the graphenic layer where a shift of $\sim 0.1eV$ between $\uparrow$ and $\downarrow$ bands can be observed (Fig. 5.6).

5.3.4 C-fase epitaxial bilayer systems

As in the case of Si-face epitaxial graphene, typical free-standing graphene characteristics and the presence of the Dirac cone are recovered with the second graphene layer (Fig. 5.8). This layer interacts weakly with the first graphenic layer maintaining a distance that is similar to that of Bernel-stacked graphite and shows a smaller corrugation with a layer thickness $t \sim 0.4$ Å, in accordance with XRD measurements[49] that indicate that also the second graphene layer should maintain a small level of corrugation. This deviation from perfect planarity also gives rise to a small separation of the Dirac cones of $\sim 0.02eV$. It should be noted that previously seen, the Fermi level remains unpinned by the interface and the Fermi level is determined by the presence of the Dirac cone. According to this picture, the presented theoretical model implies that typical graphene characteristics like the half-integer quantum hall effect should be only recovered by the second graphene layer and onwards, in contrast with experimental measurements[12, 114]. In such cases a careful examination of the real interface structure should take place in order to evaluate the presence of high concentrations of adatoms or impurities that fully passivate the substrate (e.g. as in the case of graphene deposited on SiC[100]).

5.4 Conclusions and discussion

The first part of this chapter presented bandstructure and local density of states calculations of armchair graphene nanoribbons epitaxially grown on SiC (0001). The main aspect of the presented results had to do with the importance of the SiC(0001)/graphene interface dangling bonds, which introduce states that pin the Fermi level of the system even in the case of few-layer AGNRs. Such effect can have an adverse impact on the conductive capacity of these systems since it creates an electron transport channel through interface defects, compromising

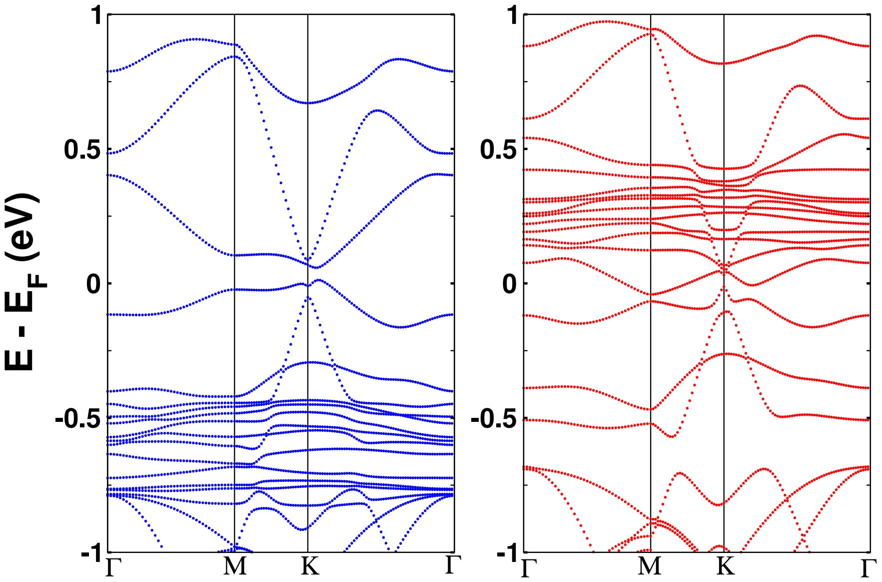

Figure 5.8: Bandstructure of two graphene layers on SiC(000$\bar{1}$) - Bandstructure of two graphene layers on a SiC(000$\bar{1}$) substrate for a↑ (left) and a ↓ (right) spin polarization.

in an non-trivial way device-related properties like high-carrier mobility. This feature also brings to attention the role of confinement, since in the absence of gate modulation, structures are always expected to behave in a metallic way, notwithstanding the wide bandgap of the interface layer.

In the second part of this chapter we have presented *ab initio* electronic structure calculations for monolayer and bilayer epitaxial graphene systems grown on 4H-SiC(000$\bar{1}$). Contrary to Si-face epitaxial graphene, we have seen that the first graphenic layer that grows on the C-face of SiC maintains a purely metallic character and an important presence of π electrons along with a non-negligible coupling with the substrates. The particularity of its geometrical configuration consists in a corrugated surface where small sp^2-bonded graphene quantum dots are terminated by carbon atoms that covalently bond with the surface. Below these quantum dots also the surface carbon atoms sp^2-hybridize, while their π bands a half-filled and present a ferromagnetic ordering due to an increased DOS concentration. Typical graphene-like characteristics are recovered with the addition of a second graphene layer. According to this picture C-face epitaxial graphene should maintain some important advantages with respect to Si-face one, like the absence of a Fermi-level pinning effect that could allow plausible device operation starting from an off state. However more research should focus on the interface transport properties in order to clear if typical free-standing graphene characteristics can be recovered (or not) in an epitaxially grown monolayer.

As a general conclusion, the present study implies that a thorough understanding of surface reconstruction is necessary for the conductive properties, and hence, for determining the device application of graphene on SiC substrates.

Chapter 6

General conclusions and outlook

As a vastly expanding field, carbon-based electronics present a series of advantages with respect to the current semiconductor technology: intrinsic low-dimensionality, mechanical stability and elasticity, exceptional electrical, optical and thermal properties to name but a few. Within this picture, one of the most promising materials for both active and passive device integration is two or quasi-one-dimensional graphene, a flat sheet of carbon atoms arranged in a honeycomb lattice. As a suspended material, graphene should be metallic with a relativistic fermion gas that almost nullifies its electron mass. A direct consequence is that electron mobilities in this system are the highest measured to date. If we consider a gap opening by means of lateral confinement, graphene nanoribbons should be ideal candidates for nanoelectronic device integration. However in ambient conditions a graphene-based device cannot be neither ideal nor suspended. This PhD thesis has dealt from a modeling and simulation point of view with the transport properties of confined graphene structures that are not ideal, i.e. that suffer defects, interact with the metallic contacts and with the substrate. Indeed, results have shown that these external factors can nontrivially influence the electronic transport properties of this material.

Defects as a source of electronic perturbation and their repercussions on the conduction mechanism was the first subject that has been studied here. For this purpose we implemented a bottom-up multiscale approach for the modeling of defect localization in $C_{6n^2}H_{6n}$ islands, i.e. graphene quantum dots with a hexagonal symmetry, by means of density functional and semiempirical approaches. Using the *ab initio* calculations as a reference, we recognized the theoretical framework under which semiempirical methods describe adequately the electronic structure of the studied systems and thereon proceeded to the calculation of quantum transport within the non-equilibrium Green's function formalism. The computational data revealed an impurity-like behavior of vacancies in these clusters and evidenced the role of parameterization even within the same semiempirical context.

In terms of conduction, failure to capture the proper chemical aspects in the presence of generic local alterations of the ideal atomic structure resulted in an improper description of the transport features. We thereon presented a systematic study of electron backscattering phenomena during conduction for graphene nanoribbons with single and multiple vacancy scatterers, for ribbon dimensions within the capabilities of modern lithographic techniques. Our analysis built upon *ab initio* parameterized semiempirical models and nonequilibrium Green's function techniques. The underlying mechanism was based on wavefunction localizations and perturbations that in the case of the first $\pi - \pi^*$ plateau gave rise to impurity-like pseudogaps with both donor and acceptor characteristics. Confinement and geometry were crucial for the manifestation of such effects. Moving towards the statistical limit of finite defect concentration we saw that significant conductance degradation and loss of typical graphene-like characteristics can take place. Finally, self-consistent quantum transport calculations showed that vacancies act as local charging centers that can induce electrostatic inhomogeneities on the ribbon topology.

The second argument treated in this thesis was the conduction implications of the interaction between graphene nanoribbons and metallic probes. We started by calculating quantum transport for metal-graphene nanoribbon heterojunctions within the atomistic self-consistent Schrödinger/Poisson scheme, paying attention on both the chemical aspects of the interface bonding as well as the one-dimensional electrostatics along the ribbon length. We saw that bandbending and doping effects can strongly influence the transport properties, giving rise to conductance asymmetries and a selective suppression of the subband formation. Within a complementary context, we saw that junction electrostatics and p-type characteristics drove the conduction mechanism in the case of high work function Au, Pd and Pt electrodes, whereas contact resistance became dominant in the case of Al. We thereon proceeded with the calculation of purely nonequilibrium charging effects in the high-bias regime for finite-size armchair graphene nanoribbons biased within source and drain metallic electrodes. The analysis evidenced dynamic electron-electron interactions that affected the conduction mechanism by provoking electronic structure alterations. The origin of such process was traced in a tracking relationship between the device's local density of states and the electrochemical potentials of the contacts. We finally discussed why such effects have no equivalent in the semiclassical limit.

The third argument treated in this thesis was the interaction between graphene and SiC substrates. We started by evaluating latteral confinement in Si-face grown films within electronic structure calculations of few-layer epitaxial graphene nanoribbons. Using an atomistic description for both the graphene layers and the substrate and real/momentum space projections we argued that the role of the heterostructure's interface can become crucial for the conducting capacity of the studied systems. The key issue that arose from this interaction was a Fermi level pinning effect introduced by dangling interface bonds. Such phenomenon was independent from the width of the considered nanostructures, compromising the importance of confinement in these systems. We thereon performed first-principles calculations based on the density functional theory for the determination of the structural and electronic properties of epitaxial graphene on 4H-SiC(000$\bar{1}$). Our approach was based on the principle of lattice commensuration using appropriate supercells that minimize non-physical stresses. Results showed that contrary to Si-face epitaxial graphene, the first graphitic layer of the C-face has a purely metallic character while π bands are partially preserved. However Dirac cones appeared only with the second graphitic layer denoting a non-null interaction with the substrate. Moreover we showed localized surface magnetic properties at the interface and an absence of the Fermi-level pinning effects seen in the case of SiC(0001).

A further theoretical investigation on the sources of non ideality in graphene-based devices should take place in the future, since experimental evidence indicates that disorder and environmental interactions are the most important factors that hinder the ideal transmission of electrons in this material. From a methodological point of view an important improvement toward this goal could be the introduction of purely *ab initio* Hamiltonians in the transport formalism for a more precise determination of the structural and energetic properties of defects, impurities, metallic contacts etc. On the other hand a multidisciplinary approach could evidence important aspects of device operation for graphene-based systems. As an example, answers to simple questions like, “how stable is a graphene nanoribbon device?”, could be affronted within combined high-temperature molecular dynamics and quantum transport calculations for the verification of defect metastability and conductance fluctuations. Finally it should be noted that a further effort in order to implement scaling and optimization techniques in quantum transport codes is necessary for a more efficient application of theoretical models over experimental data.

Appendix A

The computational code

The main technical product of this PhD period is a fully optimized and versatile quantum transport code based on the self-consistent Schrödinger/Poisson scheme. This code combines the capabilities of the open-source NanoTCAD ViDES software[37] and the in-house CNR-IMM transport code in order to deliver a three-dimensional quantum transport simulator with the following characteristics: versatile geometry, metallic and ideal contacts, Schottky and ohmic contacts, multiple gates, different dielectrics, optimized one-dimensional scaling within order-N techniques, optimized convergence within a Newton-Rhapson predictor corrector algorithm, a wide range of channel materials, electron-electron interactions, multi-scale semi-empirical Hamiltonians, and the possibility of expansion in order to incorporate fully *ab initio* Hamiltonians.

The main enhancements with respect to the open source version consist in the inclusion of the NEGF formalism based on an extended Hückel Hamiltonian[56] and all the optimizations therein: iterative techniques for a fast calculation of the surface green functions[95], block tridiagonal decomposition of the Green matrix even for non-equivalent block dimensions[89, 90], real to k-space expansions for the calculation of the surface green function of semi-infinite metallic leads[117], optimized matrix algebra operations with the use of LAPACK/BLAS libraries, real-space user-defined single and double-ζ Slater-type non-orthogonal basis sets, atomically-resolved calculation of the quantities of interest for conduction (DOS, transmission probability, etc) and the possibility to directly introduce *ab initio* Hamiltonians. The extended Hückel method, although computationally heavier with respect to the next-neighbor tight-binding one, allows for a series of new features: simulation of numerous channel materials (practically all the materials for which a parametrization exists), introduction of realistic metallic contacts and direct evaluation of local chemical/structural disorder. In other words it allows for a first-approximation chemical and spatial resolution to the description of the electronic problem.

Moreover, a series of auxiliary programs have been developed for the calculation of the bandstructure in one-dimensional periodic systems, the visualization of the wavefunctions as well as of the energy bands in real space.

Bibliography

[1] M. P. Anantram, M. S. Lundstrom, and D. E. Nikonov. Modeling of Nanoscale Devices. *arXiv:cond-mat/0610247*, Oct. 2006. 27

[2] A. Aviram and M. A. Ratner. Molecular rectifiers. *Chemical Physics Letters*, 29:277–283, Nov. 1974. doi: 10.1016/0009-2614(74)85031-1. 1

[3] S. Barraza-Lopez, M. Vanević, M. Kindermann, and M. Y. Chou. Effects of Metallic Contacts on Electron Transport through Graphene. *Phys. Rev. Lett.*, 104(7):076807–+, 2010. doi: 10.1103/PhysRevLett.104.076807. 58

[4] A. D. Becke. Density-functional thermochemistry. iii. the role of exact exchange. *The Journal of Chemical Physics*, 98(7):5648–5652, 1993. doi: 10.1063/1.464913. 31

[5] B. Biel, X. Blase, F. Triozon, and S. Roche. Anomalous Doping Effects on Charge Transport in Graphene Nanoribbons. *Physical Review Letters*, 102 (9):096803, Mar. 2009. doi: 10.1103/PhysRevLett.102.096803. 29, 46, 49, 52

[6] B. Biel, F. Triozon, X. Blase, and S. Roche. Chemically Induced Mobility Gaps in Graphene Nanoribbons: A Route for Upscaling Device Performances. *Nano Letters*, 9:2725–2729, July 2009. doi: 10.1021/nl901226s. 6, 56

[7] J. S. Binkley, J. A. Pople, and W. J. Hehre. Self-consistent molecular orbital methods. 21. small split-valence basis sets for first-row elements. *Journal of the American Chemical Society*, 1980. 31

[8] P. Blake, R. Yang, S. V. Morozov, F. Schedin, L. A. Ponomarenko, A. A. Zhukov, R. R. Nair, I. V. Grigorieva, K. S. Novoselov, and A. K. Geim. Influence of metal contacts and charge inhomogeneity on transport properties of graphene near the neutrality point. *Solid State Communications*, 149:1068–1071, 2009. 58

[9] D. W. Boukhvalov and M. I. Katsnelson. Tuning the gap in bilayer graphene using chemical functionalization: Density functional calculations. *Physical Review B*, 78(8):085413, 2008. doi: 10.1103/PhysRevB.78.085413. 6, 29

[10] S. Bouzzine, S. Bouzakraoui, M. Bouachrine, and M. Hamidi. Density functional theory (b3lyp/6-31g*) study of oligothiophenes in their aromatic and polaronic states. *Journal of Molecular Structure-THEOCHEM*, 726(1-3):271–276, AUG 1 2005. doi: 10.1016/j.theochem.2005.04.023. 31

[11] M. Brandbyge, J. Mozos, P. Ordejón, J. Taylor, and K. Stokbro. Density-functional method for nonequilibrium electron transport. *Physical Review B*, 65(16):165401–+, Apr. 2002. doi: 10.1103/PhysRevB.65.165401. 27

[12] N. Camara, B. Jouault, A. Caboni, B. Jabakhanji, W. Desrat, E. Pausas, C. Consejo, N. Mestres, P. Godignon, and J. Camassel. Growth of monolayer graphene on 8[degree] off-axis 4h–sic (000–1) substrates with application to quantum transport devices. *Applied Physics Letters*, 97(9):093107, 2010. doi: 10.1063/1.3480610. URL `http://link.aip.org/link/?APL/97/093107/1`. 74, 75, 86

[13] J. M. Carlsson and M. Scheffler. Structural, Electronic, and Chemical Properties of Nanoporous Carbon. *Physical Review Letters*, 96(4):046806, Feb. 2006. doi: 10.1103/PhysRevLett.96.046806. 29, 30

[14] A. H. Castro Neto, F. Guinea, N. M. R. Peres, K. S. Novoselov, and A. K. Geim. The electronic properties of graphene. *Reviews of Modern Physics*, 81:109–162, Jan. 2009. doi: 10.1103/RevModPhys.81.109. 2

[15] J. Cerdá and F. Soria. Accurate and transferable extended Hückel-type tight-binding parameters. *Physical Review B*, 61:7965–7971, Mar. 2000. doi: 10.1103/PhysRevB.61.7965. 60, 76

[16] J. Cerdá and F. Soria. Accurate and transferable extended hückel-type tight-binding parameters. *Phys. Rev. B*, 61(12):7965–7971, Mar 2000. doi: 10.1103/PhysRevB.61.7965. 32

[17] J. I. Cerda. http://www.icmm.csic.es/jcerda/. 32

[18] J. Chen, C. Jang, S. Adam, M. S. Fuhrer, E. D. Williams, and M. Ishigami. Charged-impurity scattering in graphene. *Nature Physics*, 4:377–381, May 2008. doi: 10.1038/nphys935. 53

[19] J. Chen, W. G. Cullen, C. Jang, M. S. Fuhrer, and E. D. Williams. Defect Scattering in Graphene. *Physical Review Letters*, 102(23):236805, June 2009. doi: 10.1103/PhysRevLett.102.236805. 29, 57

[20] K. A. Cho, T. Shimada, M. Sakurai, and A. Koma. Effect of growth temperature and substrate materials on epitaxial growth of coronene. *Journal of Applied Physics*, 84:268–274, July 1998. doi: 10.1063/1.368092. 34

[21] J. B. Collins, P. von R. Schleyer, J. S. Binkley, and J. A. Pople. Self-consistent molecular orbital methods. xvii. geometries and binding energies of second-row molecules. a comparison of three basis sets. *The Journal of Chemical Physics*, 64(12):5142–5151, 1976. doi: 10.1063/1.432189. 31

[22] G. Compagnini, F. Giannazzo, S. Sonde, V. Raineri, and E. Rimini. Ion irradiation and defect formation in single layer graphene. *Carbon*, 47(14): 3201 – 3207, 2009. ISSN 0008-6223. doi: DOI:10.1016/j.carbon.2009.07.033. 56

[23] A. Cresti and S. Roche. Edge-disorder-dependent transport length scales in graphene nanoribbons: From Klein defects to the superlattice limit. *Physical Review B*, 79(23):233404–+, June 2009. doi: 10.1103/PhysRevB.79.233404. 55

[24] S. Datta. *Electronic transport in mesoscopic systems*. Cambridge University Press, 1995. 10, 14, 16, 18, 20, 28, 47, 60

[25] S. Datta. Nanoscale device modeling: the Green's function method. *Superlattices and Microstructures*, 28:253–278, Oct. 2000. doi: 10.1006/spmi.2000.0920. 19, 20, 33

[26] S. Datta. *Quantum transport: atom to transistor*. Cambridge University Press, 2005. 15, 18, 19, 20, 26, 28, 77, 80

[27] S. Datta. *Nanoelectronic devices: A unified view*. Oxford Handbook on Nanoscience and Nanotechnology: Frontiers and Advances, 2008. 20, 28

[28] I. Deretzis and A. La Magna. Role of contact bonding on electronic transport in metal-carbon nanotube-metal systems. *Nanotechnology*, 17(20): 5063–5072, 2006. 32, 33, 42, 66

[29] I. Deretzis and A. La Magna. Bias-driven local density of states alterations and transport in ballistic molecular devices. *The Journal of Chemical Physics*, 128(16):164706, 2008. doi: 10.1063/1.2905216. 63, 66, 68, 70, 71

[30] I. Deretzis and A. La Magna. Electronic structure of epitaxial graphene nanoribbons on SiC(0001). *Applied Physics Letters*, 95(6):063111, Aug. 2009. doi: 10.1063/1.3202397. 29, 49, 83

[31] S. Dubois, Z. Zanolli, X. Declerck, and J. Charlier. Electronic properties and quantum transport in Graphene-based nanostructures. *European Physical Journal B*, 72:1–24, Nov. 2009. doi: 10.1140/epjb/e2009-00327-8. 2, 7, 8

[32] K. V. Emtsev, A. Bostwick, K. Horn, J. Jobst, G. L. Kellogg, L. Ley, J. L. McChesney, T. Ohta, S. A. Reshanov, J. Röhrl, E. Rotenberg, A. K. Schmid, D. Waldmann, H. B. Weber, and T. Seyller. Towards wafer-size graphene layers by atmospheric pressure graphitization of silicon carbide. *Nature Materials*, 8:203–207, Mar. 2009. doi: 10.1038/nmat2382. 9, 29, 74, 75

[33] M. J. F. et al. Gaussian 03, Revision C.02. Gaussian, Inc., Wallingford, CT, 2004. 31

[34] J. K. Fawcett and J. Trotter. The Crystal and Molecular Structure of Coronene. *Royal Society of London Proceedings Series A*, 289:366–376, jan 1966. 30

[35] J. Fernández-Rossier and J. J. Palacios. Magnetism in Graphene Nanoislands. *Physical Review Letters*, 99(17):177204–+, Oct. 2007. doi: 10.1103/PhysRevLett.99.177204. 38

[36] G. Fiori and G. Iannaccone. Simulation of Graphene Nanoribbon Field-Effect Transistors. *IEEE Electron Device Letters*, 28:760–762, Aug. 2007. doi: 10.1109/LED.2007.901680. 53

[37] G. Fiori and G. Iannaccone. Nanotcad vides, Oct 2008. URL `http://nanohub.org/resources/5116`. 92

[38] G. Fiori and G. Iannaccone. On the Possibility of Tunable-Gap Bilayer Graphene FET. *IEEE Electron Device Letters*, 30:261–264, Mar. 2009. doi: 10.1109/LED.2008.2010629. 6

[39] G. Fiori, G. Iannaccone, and G. Klimeck. A Three-Dimensional Simulation Study of the Performance of Carbon Nanotube Field-Effect Transistors With Doped Reservoirs and Realistic Geometry. *IEEE Transactions on Electron Devices*, 53:1782–1788, Aug. 2006. doi: 10.1109/TED.2006.878018. 53, 59, 60

[40] G. Fiori, G. Iannaccone, and G. Klimeck. Coupled Mode Space Approach for the Simulation of Realistic Carbon Nanotube Field-Effect Transistors. *IEEE Transactions on Nanotechnology*, 6:475–480, July 2007. doi: 10.1109/TNANO.2007.896842. 26

[41] G. Forte, A. Grassi, G. M. Lombardo, A. La Magna, G. G. N. Angilella, R. Pucci, and R. Vilardi. Modeling vacancies and hydrogen impurities in graphene: A molecular point of view. *Physics Letters A*, 372:6168–6174, Sept. 2008. doi: 10.1016/j.physleta.2008.08.014. 30, 40

[42] M. Fujita, K. Wakabayashi, K. Nakada, and K. Kusakabe. Peculiar Localized State at Zigzag Graphite Edge. *Journal of the Physical Society of Japan*, 65:1920–+, July 1996. doi: 10.1143/JPSJ.65.1920. 38

[43] P. Gava, M. Lazzeri, A. M. Saitta, and F. Mauri. Ab initio study of gap opening and screening effects in gated bilayer graphene. *Physical Review B*, 79(16):165431, Apr. 2009. doi: 10.1103/PhysRevB.79.165431. 6, 29

[44] A. K. Geim and K. S. Novoselov. The rise of graphene. *Nature Materials*, 6:183–191, Mar. 2007. doi: 10.1038/nmat1849. 2, 5, 58

[45] M. S. Gordon, J. S. Binkley, J. A. Pople, W. J. Pietro, and W. J. Hehre. Self-consistent molecular-orbital methods. 22. small split-valence basis sets for second-row elements. *Journal of the American Chemical Society*, 1982. 31

[46] N. Gorjizadeh, A. A. Farajian, and Y. Kawazoe. The effects of defects on the conductance of graphene nanoribbons. *Nanotechnology*, 20(1):015201, Jan. 2009. doi: 10.1088/0957-4484/20/1/015201. 52

[47] J. Guo, S. Datta, M. Lundstrom, and M. P. Anantam. Towards Multi-Scale Modeling of Carbon Nanotube Transistors. *International J. on Multiscale Computational Engineering*, 2:257–276, 2004. 62

[48] J. Guo, Y. Yoon, and Y. Ouyang. Gate Electrostatics and Quantum Capacitance of Graphene Nanoribbons. *Nano Letters*, 7:1935–1940, July 2007. doi: 10.1021/nl0706190. 67

[49] J. Hass, R. Feng, J. E. Millán-Otoya, X. Li, M. Sprinkle, P. N. First, W. A. de Heer, E. H. Conrad, and C. Berger. Structural properties of the multilayer graphene/ 4H-SiC(000$\bar{1}$) system as determined by surface x-ray diffraction. *Physical Review B*, 75(21):214109–+, June 2007. doi: 10.1103/PhysRevB.75.214109. 74, 86

[50] J. Hass, F. Varchon, J. E. Millán-Otoya, M. Sprinkle, N. Sharma, W. A. de Heer, C. Berger, P. N. First, L. Magaud, and E. H. Conrad. Why Multilayer Graphene on 4H-SiC(000$\bar{1}$) Behaves Like a Single Sheet of Graphene. *Physical Review Letters*, 100(12):125504–+, Mar. 2008. doi: 10.1103/PhysRevLett.100.125504. 75

[51] W. J. Hehre, R. F. Stewart, and J. A. Pople. Self-consistent molecular-orbital methods. i. use of gaussian expansions of slater-type atomic orbitals. *The Journal of Chemical Physics*, 51(6):2657–2664, 1969. doi: 10.1063/1.1672392. 31

[52] S. Heinze, J. Tersoff, R. Martel, V. Derycke, J. Appenzeller, and P. Avouris. Carbon Nanotubes as Schottky Barrier Transistors. *Phys. Rev. Lett.*, 89 (10):106801–+, 2002. doi: 10.1103/PhysRevLett.89.106801. 64

[53] F. Hiebel, P. Mallet, L. Magaud, and J. Veuillen. Atomic and electronic structure of monolayer graphene on 6H-SiC$(000\bar{1})(3\times3)$: A scanning tunneling microscopy study. *Physical Review B*, 80(23):235429–+, Dec. 2009. doi: 10.1103/PhysRevB.80.235429. 74, 83

[54] I. G. Hill, A. Kahn, Z. G. Soos, R. A. Pascal, and Jr. Charge-separation energy in films of [pi]-conjugated organic molecules. *Chemical Physics Letters*, 327(3-4):181 – 188, 2000. ISSN 0009-2614. doi: DOI:10.1016/S0009-2614(00)00882-4. 36

[55] M. Hjort and S. Stafström. Modeling vacancies in graphite via the Hückel method. *Physical Review B*, 61:14089–14094, May 2000. doi: 10.1103/PhysRevB.61.14089. 29

[56] R. Hoffmann. An extended h[u-umlaut]ckel theory. i. hydrocarbons. *The Journal of Chemical Physics*, 39(6):1397–1412, 1963. doi: 10.1063/1.1734456. 31, 32, 92

[57] B. Huang, F. Liu, J. Wu, B.-L. Gu, and W. Duan. Suppression of spin polarization in graphene nanoribbons by edge defects and impurities. *Phys. Rev. B*, 77(15):153411–+, Apr. 2008. doi: 10.1103/PhysRevB.77.153411. 8, 38

[58] B. Huard, N. Stander, J. A. Sulpizio, and D. Goldhaber-Gordon. Evidence of the role of contacts on the observed electron-hole asymmetry in graphene. *Physical Review B*, 78(12):121402–+, Sept. 2008. doi: 10.1103/PhysRevB.78.121402. 67

[59] S. Iijima. Helical microtubules of graphitic carbon. *Nature*, 354:56–58, Nov. 1991. doi: 10.1038/354056a0. 1

[60] Y. Imry and R. Landauer. Conductance viewed as transmission. *Reviews of Modern Physics Supplement*, 71:306–+, Mar. 1999. doi: 10.1103/RevModPhys.71.S306. 20

[61] G. G. Jernigan, B. L. Vanmil, J. L. Tedesco, J. G. Tischler, E. R. Glaser, A. Davidson, III, P. M. Campbell, and D. K. Gaskill. Comparison of Epitaxial Graphene on Si-face and C-face 4H SiC Formed by Ultrahigh Vacuum and RF Furnace Production. *Nano Letters*, 9:2605–2609, July 2009. doi: 10.1021/nl900803z. 74

[62] J. Jobst, D. Waldmann, F. Speck, R. Hirner, D. K. Maude, T. Seyller, and H. B. Weber. Quantum oscillations and quantum Hall effect in epitaxial graphene. *Physical Review B*, 81(19):195434–+, May 2010. doi: 10.1103/PhysRevB.81.195434. 74

[63] P. A. Khomyakov, G. Giovannetti, P. C. Rusu, G. Brocks, J. van den Brink, and P. J. Kelly. First-principles study of the interaction and charge transfer between graphene and metals. *Phys. Rev. B*, 79(19):195425–+, 2009. doi: 10.1103/PhysRevB.79.195425. 58

[64] D. Kienle, J. I. Cerda, and A. W. Ghosh. Extended Hückel theory for band structure, chemistry, and transport. I. Carbon nanotubes. *Journal of Applied Physics*, 100(4):043714–+, Aug. 2006. doi: 10.1063/1.2259818. 25, 32, 36, 47, 60, 76, 77

[65] S. Kim, J. Ihm, H. J. Choi, and Y. Son. Origin of Anomalous Electronic Structures of Epitaxial Graphene on Silicon Carbide. *Physical Review Letters*, 100(17):176802–+, May 2008. doi: 10.1103/PhysRevLett.100.176802. 83

[66] A. La Magna, I. Deretzis, G. Forte, and R. Pucci. Violation of the single-parameter scaling hypothesis in disordered graphene nanoribbons. *Physical Review B*, 78(15):153405–+, Oct. 2008. doi: 10.1103/PhysRevB.78.153405. 10, 55

[67] A. La Magna, I. Deretzis, G. Forte, and R. Pucci. Conductance distribution in doped and defected graphene nanoribbons. *Physical Review B*, 80(19): 195413–+, Nov. 2009. doi: 10.1103/PhysRevB.80.195413. 56, 57

[68] C. Lee, W. Yang, and R. G. Parr. Development of the colle-salvetti correlation-energy formula into a functional of the electron density. *Phys. Rev. B*, 37(2):785–789, Jan 1988. doi: 10.1103/PhysRevB.37.785. 31

[69] E. J. H. Lee, K. Balasubramanian, R. T. Weitz, M. Burghard, and K. Kern. Contact and edge effects in graphene devices. *Nat. Nano.*, 3:486–490, 2008. doi: 10.1038/nnano.2008.172. 58

[70] F. Léonard and J. Tersoff. Novel Length Scales in Nanotube Devices. *Phys. Rev. Lett.*, 83:5174–5177, 1999. doi: 10.1103/PhysRevLett.83.5174. 58, 63

[71] I. N. Levine. *Quantum Chemistry.* Pearson Education International, 2009. 22, 23

[72] Y. Lin, V. Perebeinos, Z. Chen, and P. Avouris. Electrical observation of subband formation in graphene nanoribbons. *Phys. Rev. B*, 78(16):161409–+, 2008. doi: 10.1103/PhysRevB.78.161409. 58

[73] Y. Lin, K. A. Jenkins, A. Valdes-Garcia, J. P. Small, D. B. Farmer, and P. Avouris. Operation of Graphene Transistors at Gigahertz Frequencies. *Nano Letters*, 9:422–426, Jan. 2009. doi: 10.1021/nl803316h. 10, 58

[74] Y. Lin, C. Dimitrakopoulos, K. A. Jenkins, D. B. Farmer, H. Chiu, A. Grill, and P. Avouris. 100-GHz Transistors from Wafer-Scale Epitaxial Graphene. *Science*, 327:662–, Feb. 2010. doi: 10.1126/science.1184289. 74

[75] A. Mattausch and O. Pankratov. AbInitio Study of Graphene on SiC. *Physical Review Letters*, 99(7):076802–+, Aug. 2007. doi: 10.1103/PhysRevLett.99.076802. 74, 75, 76, 79, 83

[76] J. C. Meyer, C. Kisielowski, R. Erni, M. D. Rossell, M. F. Crommie, and A. Zettl. Direct Imaging of Lattice Atoms and Topological Defects in Graphene Membranes. *Nano Letters*, 8:3582–3586, Nov. 2008. doi: 10.1021/nl801386m. 9, 29

[77] H. B. Michaelson. The work function of the elements and its periodicity. *J. Appl. Phys.*, 48:4729–4733, 1977. doi: 10.1063/1.323539. 60

[78] A. Modelli, L. Mussoni, and D. Fabbri. Electron affinities of polycyclic aromatic hydrocarbons by means of b3lyp/6-31+g* calculations. *The Journal of Physical Chemistry A*, 110(20):6482–6486, 2006. doi: 10.1021/jp0605911. 31

[79] T. Mueller, F. Xia, M. Freitag, J. Tsang, and P. Avouris. Role of contacts in graphene transistors: A scanning photocurrent study. *Phys. Rev. B*, 79 (24):245430–+, 2009. doi: 10.1103/PhysRevB.79.245430. 58

[80] A. H. C. Neto, F. Guinea, N. M. R. Peres, K. S. Novoselov, and A. K. Geim. The electronic properties of graphene. *Reviews of Modern Physics*, 81(1):109, 2009. doi: 10.1103/RevModPhys.81.109. 29

[81] K. S. Novoselov, A. K. Geim, S. V. Morozov, D. Jiang, Y. Zhang, S. V. Dubonos, I. V. Grigorieva, and A. A. Firsov. Electric Field Effect in Atomically Thin Carbon Films. *Science*, 306:666–669, Oct. 2004. doi: 10.1126/science.1102896. 1

[82] R. Y. Oeiras, F. M. Araújo-Moreira, and E. Z. da Silva. Defect-mediated half-metal behavior in zigzag graphene nanoribbons. *Physical Review B*, 80 (7):073405, 2009. doi: 10.1103/PhysRevB.80.073405. 52

[83] S. Oida, F. R. McFeely, J. B. Hannon, R. M. Tromp, M. Copel, Z. Chen, Y. Sun, D. B. Farmer, and J. Yurkas. Decoupling graphene from SiC(0001) via oxidation. *Physical Review B*, 82(4):041411–+, July 2010. doi: 10.1103/PhysRevB.82.041411. 74

[84] C. Oshima and A. Nagashima. REVIEW ARTICLE: Ultra-thin epitaxial films of graphite and hexagonal boron nitride on solid surfaces. *Journal of Physics Condensed Matter*, 9:1–20, 1997. doi: 10.1088/0953-8984/9/1/004. 60

[85] J. J. Palacios, J. Fernández-Rossier, and L. Brey. Vacancy-induced magnetism in graphene and graphene ribbons. *Physical Review B*, 77(19): 195428, May 2008. doi: 10.1103/PhysRevB.77.195428. 29, 30, 50

[86] M. Paulsson. Non Equilibrium Green's Functions for Dummies: Introduction to the One Particle NEGF equations. *arXiv:cond-mat/0210519*, Oct. 2002. 14, 15, 18

[87] X. Peng and R. Ahuja. Symmetry Breaking Induced Bandgap in Epitaxial Graphene Layers on SiC. *Nano Letters*, 8:4464–4468, Dec. 2008. doi: 10.1021/nl802409q. 74

[88] V. M. Pereira, J. M. B. Lopes Dos Santos, and A. H. Castro Neto. Modeling disorder in graphene. *Physical Review B*, 77(11):115109, Mar. 2008. doi: 10.1103/PhysRevB.77.115109. 3, 29, 30, 37, 40, 46, 47

[89] D. Petersen, H. Sørensen, P. Hansen, S. Skelboe, and K. Stokbro. Block tridiagonal matrix inversion and fast transmission calculations. *Journal of Computational Physics*, 227(6):3174–3190, 2008. 27, 92

[90] D. Petersen, S. Li, K. Stokbro, H. Sørensen, P. Hansen, S. Skelboe, and E. Darve. A hybrid method for the parallel computation of green's functions. *Journal of Computational Physics*, 228(14):5020–5039, 2009. 27, 53, 60, 92

[91] W. J. Pietro, M. M. Francl, W. J. Hehre, D. J. DeFrees, J. A. Pople, and J. S. Binkley. Self-consistent molecular orbital methods. 24. supplemented small split-valence basis sets for second-row elements. *Journal of the American Chemical Society*, 1982. 31

[92] H. Raza and E. C. Kan. Armchair graphene nanoribbons: Electronic structure and electric-field modulation. *Physical Review B*, 77(24):245434–+, June 2008. doi: 10.1103/PhysRevB.77.245434. 76

[93] C. Riedl, U. Starke, J. Bernhardt, M. Franke, and K. Heinz. Structural properties of the graphene-SiC(0001) interface as a key for the preparation of homogeneous large-terrace graphene surfaces. *Physical Review B*, 76(24): 245406–+, Dec. 2007. doi: 10.1103/PhysRevB.76.245406. 75

[94] C. Riedl, C. Coletti, T. Iwasaki, A. A. Zakharov, and U. Starke. Quasi-Free-Standing Epitaxial Graphene on SiC Obtained by Hydrogen Intercalation. *Physical Review Letters*, 103(24):246804–+, Dec. 2009. doi: 10.1103/PhysRevLett.103.246804. 74

[95] M. P. L. Sancho, J. M. L. Sancho, J. M. L. Sancho, and J. Rubio. Highly convergent schemes for the calculation of bulk and surface green functions. *Journal of Physics F: Metal Physics*, 15(4):851–858, 1985. 27, 80, 92

[96] P. G. Schroeder, C. B. France, B. A. Parkinson, and R. Schlaf. Orbital alignment at p-sexiphenyl and coronene/layered materials interfaces measured with photoemission spectroscopy. *Journal of Applied Physics*, 91: 9095–9107, June 2002. doi: 10.1063/1.1473217. 34, 35

[97] P. Shemella, Y. Zhang, M. Mailman, P. M. Ajayan, and S. K. Nayak. Energy gaps in zero-dimensional graphene nanoribbons. *Applied Physics Letters*, 91(4):042101–+, July 2007. doi: 10.1063/1.2761531. 69

[98] J. M. Soler, E. Artacho, J. D. Gale, A. García, J. Junquera, P. Ordejón, and D. Sánchez-Portal. The SIESTA method for ab initio order-N materials simulation. *Journal of Physics Condensed Matter*, 14:2745–2779, Mar. 2002. doi: 10.1088/0953-8984/14/11/302. 82

[99] Y. Son, M. L. Cohen, and S. G. Louie. Energy Gaps in Graphene Nanoribbons. *Physical Review Letters*, 97(21):216803, Nov. 2006. doi: 10.1103/PhysRevLett.97.216803. 6, 7, 8, 34, 38, 47, 50, 59, 63, 65, 67, 69, 77

[100] S. Sonde, F. Giannazzo, V. Raineri, R. Yakimova, J. Huntzinger, A. Tiberj, and J. Camassel. Electrical properties of the graphene/ 4H-SiC (0001)

interface probed by scanning current spectroscopy. *Physical Review B*, 80 (24):241406–+, Dec. 2009. doi: 10.1103/PhysRevB.80.241406. 81, 86

[101] M. Sprinkle, D. Siegel, Y. Hu, J. Hicks, A. Tejeda, A. Taleb-Ibrahimi, P. Le Fèvre, F. Bertran, S. Vizzini, H. Enriquez, S. Chiang, P. Soukiassian, C. Berger, W. A. de Heer, A. Lanzara, and E. H. Conrad. First Direct Observation of a Nearly Ideal Graphene Band Structure. *Physical Review Letters*, 103(22):226803–+, Nov. 2009. doi: 10.1103/PhysRevLett.103.226803. 75

[102] M. Sprinkle, J. Hicks, A. Tejeda, A. Taleb-Ibrahimi, P. Le Fèvre, F. Bertran, H. Tinkey, M. C. Clark, P. Soukiassian, D. Martinotti, J. Hass, W. A. de Heer, C. Berger, and E. H. Conrad. Structure and electronic properties of epitaxial graphene grown on SiC. *ArXiv e-prints, 1001.3869*, Jan. 2010. 74, 75, 82

[103] U. Starke and C. Riedl. Epitaxial graphene on SiC(0001) and \mathrm {SiC}(000\bar {1}) : from surface reconstructions to carbon electronics. *Journal of Physics Condensed Matter*, 21(13):134016–+, Apr. 2009. doi: 10.1088/0953-8984/21/13/134016. 74, 83

[104] P. J. Stephens, F. J. Devlin, C. F. Chabalowski, and M. J. Frisch. Ab initio calculation of vibrational absorption and circular dichroism spectra using density functional force fields. *The Journal of Physical Chemistry*, 98(45): 11623–11627, 1994. doi: 10.1021/j100096a001. 31

[105] D. Sun, C. Divin, C. Berger, W. A. de Heer, P. N. First, and T. B. Norris. Spectroscopic Measurement of Interlayer Screening in Multilayer Epitaxial Graphene. *Physical Review Letters*, 104(13):136802–+, Apr. 2010. doi: 10.1103/PhysRevLett.104.136802. 75

[106] P. W. Sutter, J. Flege, and E. A. Sutter. Epitaxial graphene on ruthenium. *Nature Materials*, 7:406–411, May 2008. doi: 10.1038/nmat2166. 9

[107] A. Trellakis, A. T. Galick, A. Pacelli, and U. Ravaioli. Iteration scheme for the solution of the two-dimensional Schrödinger-Poisson equations in quantum structures. *J. Appl. Phys.*, 81:7880–7884, 1997. doi: 10.1063/1.365396. 60

[108] N. Troullier and J. L. Martins. Efficient pseudopotentials for plane-wave calculations. *Physical Review B*, 43:1993–2006, Jan. 1991. doi: 10.1103/PhysRevB.43.1993. 82

[109] F. Varchon, R. Feng, J. Hass, X. Li, B. N. Nguyen, C. Naud, P. Mallet, J.-Y. Veuillen, C. Berger, E. H. Conrad, and L. Magaud. Electronic Structure of Epitaxial Graphene Layers on SiC: Effect of the Substrate. *Physical Review Letters*, 99(12):126805–+, Sept. 2007. doi: 10.1103/PhysRevLett.99.126805. 74, 83

[110] G. Vignale and M. di Ventra. Incompleteness of the Landauer formula for electronic transport. *Physical Review B*, 79(1):014201–+, Jan. 2009. doi: 10.1103/PhysRevB.79.014201. 28

[111] C. Virojanadara, M. Syväjarvi, R. Yakimova, L. I. Johansson, A. A. Zakharov, and T. Balasubramanian. Homogeneous large-area graphene layer growth on 6H -SiC(0001). *Physical Review B*, 78(24):245403–+, Dec. 2008. doi: 10.1103/PhysRevB.78.245403. 74

[112] S. H. Vosko, L. Wilk, and M. Nusair. Accurate spin-dependent electron liquid correlation energies for local spin density calculations: a critical analysis. *Canadian Journal of Physics*, 58:1200–+, 1980. 31

[113] T. Wassmann, A. P. Seitsonen, A. M. Saitta, M. Lazzeri, and F. Mauri. Structure, stability, edge states, and aromaticity of graphene ribbons. *Phys. Rev. Lett.*, 101(9):096402, Aug 2008. doi: 10.1103/PhysRevLett.101.096402. 9, 50

[114] X. Wu, Y. Hu, M. Ruan, N. K. Madiomanana, J. Hankinson, M. Sprinkle, C. Berger, and W. A. de Heer. Half integer quantum Hall effect in high mobility single layer epitaxial graphene. *Applied Physics Letters*, 95(22):223108–+, Nov. 2009. doi: 10.1063/1.3266524. 75, 84, 86

[115] F. Xia, T. Mueller, Y.-m. Lin, A. Valdes-Garcia, and P. Avouris. Ultrafast graphene photodetector. *Nat Nano*, 4(12):839–843, Dec. 2009. 29

[116] O. V. Yazyev and L. Helm. Defect-induced magnetism in graphene. *Physical Review B*, 75(12):125408, 2007. doi: 10.1103/PhysRevB.75.125408. 29

[117] F. Zahid, M. Paulsson, and S. Datta. Electrical conduction in molecules," chapter in advanced semiconductors and organic nano-techniques. ed. H. Morkoc, Academic Press, 2003, ISBN: 0-12-507060-8, 2003. 16, 32, 60, 92

[118] F. Zahid, M. Paulsson, E. Polizzi, A. W. Ghosh, L. Siddiqui, and S. Datta. A self-consistent transport model for molecular conduction based on extended Hückel theory with full three-dimensional electrostatics. *The Journal of Chemical Physics*, 123(6):064707–+, Aug. 2005. doi: 10.1063/1.1961289. 66, 67

[119] Y. Zhang, T. Tang, C. Girit, Z. Hao, M. C. Martin, A. Zettl, M. F. Crommie, Y. R. Shen, and F. Wang. Direct observation of a widely tunable bandgap in bilayer graphene. *Nature*, 459:820–823, June 2009. doi: 10.1038/nature08105. 6

[120] H. Zheng, Z. F. Wang, T. Luo, Q. W. Shi, and J. Chen. Analytical study of electronic structure in armchair graphene nanoribbons. *Physical Review B*, 75(16):165414, Apr. 2007. doi: 10.1103/PhysRevB.75.165414. 7, 49

[121] S. Y. Zhou, G. Gweon, A. V. Fedorov, P. N. First, W. A. de Heer, D. Lee, F. Guinea, A. H. Castro Neto, and A. Lanzara. Substrate-induced bandgap opening in epitaxial graphene. *Nature Materials*, 6:916–+, Nov. 2007. doi: 10.1038/nmat2056. 6

[122] U. Zimmermann and N. Karl. Epitaxial growth of coronene and hexa-peri-benzocoronene on mos2(0001) and graphite (0001): a leed study of molecular size effects. *Surface Science*, 268(1-3):296 – 306, 1992. ISSN 0039-6028. doi: DOI:10.1016/0039-6028(92)90969-D. 34

List of Publications

List of publications during the PhD period:

1. A. La Magna, I. Deretzis, "Phonon Driven Nonlinear Electrical Behavior in Molecular Devices", *Physical Review Letters* **99**, 136404 (2007)
2. I. Deretzis, A. La Magna, "Bias-driven local density of states alterations and transport in ballistic molecular devices", *Journal of Chemical Physics* **128**, 164706 (2008)
3. I. Deretzis, A. La Magna, "Nonequilibrium aspects of armchair graphene nanoribbon conduction", *Materials Science in Semiconductor Processing* **11**, 190 (2008)
4. A. La Magna, I. Deretzis, G. Forte, R. Pucci, "Violation of the single-parameter scaling hypothesis in disordered graphene nanoribbons", *Physical Review B* **78**, 153405 (2008)
5. A. La Magna, I. Deretzis, V. Privitera, "Insulator-metal transition in biased finite polyyne systems", *European Physical Journal B* **70**, 311-316 (2009)
6. I. Deretzis, A. La Magna, "Electronic structure of epitaxial graphene nanoribbons on SiC (0001)", *Applied Physics Letters* 95, 063111 (2009)
7. A. La Magna, I. Deretzis, G. Forte, R. Pucci, "Conductance distribution in doped and defected graphene nanoribbons", *Physical Review B* **80**, 195413 (2009)
8. G. Forte, A. La Magna, I. Deretzis, R. Pucci, "Ab initio prediction of boron compounds arising from borozene: Structural and electronic properties", *Nanoscale Research Letters* **5**, 158 (2010)
9. I. Deretzis, G. Forte, A. Grassi, A. La Magna, G. Piccitto, R. Pucci, "A multiscale study of electronic structure and quantum transport in $C_{6n^2}H_{6n}$-based graphene quantum dots", *Journal of Physics: Condensed Matter* **22**, 095504 (2010)

10. I. Deretzis, G. Fiori, G. Iannaccone, A. La Magna, "Effects due to backscattering and pseudogap features in graphene nanoribbons with single vacancies", *Physical Review B* **81**, 085427 (2010)
11. A. La Magna, I. Deretzis, G. Forte, R. Pucci, "Lack of universal conductance features in disordered graphene nanoribbons", *Physica Status Solidi C* **7**, 1246 (2010)
12. I. Deretzis, G. Fiori, G. Iannaccone, G. Piccitto, A. La Magna, "Quantum transport modeling of defected graphene nanoribbons", *Physica E*, doi:`10.1016/j.physe.2010.06.024`
13. I. Deretzis, G. Fiori, G. Iannaccone, A. La Magna, "Atomistic quantum transport modeling of metal-graphene nanoribbon heterojunctions", *Physical Review B* **82**, 161413(R) (2010)
14. I. Deretzis, A. La Magna, "Sinlge-layer metallicity and interface magnetism of epitaxial graphene on SiC(000$\bar{1}$)", submitted